INVESTIGATION OF PRESSURE-TUBE AND CALANDRIA-TUBE DEFORMATION FOLLOWING A SINGLE-CHANNEL BLOCKAGE EVENT IN ACR-700

Craig Gerardi

Professor Jacopo Buongiorno

Nuclear Science and Engineering Department

MIT

August 2005

ABSTRACT

The ACR-700 is an advanced pressure-tube (PT) reactor being developed by Atomic Energy of Canada Limited (AECL). As in conventional CANDU reactors, the PTs are horizontal. Each PT is surrounded by a calandria tube (CT), and the gap in between is filled with carbon dioxide gas. The space between the CTs is filled with the heavy-water moderator.

One postulated accident scenario for ACR-700 is the complete coolant flow blockage of a single PT. The flow is not monitored within each individual PT, thus during the early stages of this accident the reactor remains at full power and full pressure, resulting in rapid coolant boil-off and fuel overheating. Melting of the Zircaloy (Zry) components of the fuel bundle (cladding, end plates and end caps) can occur, with relocation of some molten material to the bottom of the PT. The hot spot caused by the molten Zry/PT interaction may cause PT/CT failure due to localized plastic strains. Failure of the PT/CT results in depressurization of the primary system, which triggers a reactor scram, after which the decay heat is removed via reflooding, thus PT/CT rupture effectively terminates the accident. Clearly, prediction of the time scale and conditions under which PT/CT failure occurs is of great importance for this accident.

We analyzed the following key phenomena occurring after the blockage:

(a) Coolant boil-off
(b) Cladding heat-up and melting
(c) Dripping of molten Zircaloy (Zry) from the fuel pin
(d) Thermal interaction between the molten Zry and the PT
(e) Localized bulging of the PT
(f) Interaction of the bulged PT with the CT

Simple one-dimensional models were adequate to describe (a), (b) and (c), while the three-dimensional nature of (d), (e) and (f) required the use of more sophisticated models including a finite-element description of the thermal transients within the PT and the CT, implemented with the code COSMOSM.

The main findings of the study are as follows:

(1) Most coolant boils off within 3 s of accident initiation.

(2) Depending on the magnitude of radiation heat transfer between adjacent fuel pins, the cladding of the hot fuel pin in the blocked PT reaches the melting point of Zry in 7 to 10 s after accident initiation.

(3) Inception of melting of the UO_2 fuel pellets is not expected for at least another 7 s after Zry melting.

(4) Several effects could theoretically prevent molten Zry dripping from the fuel pins, including Zry/UO_2 interaction and Zry oxidation. However, it was concluded that because of the very high heat-up rate typical of the flow blockage accident sequence, holdup of molten Zry would not occur. Experimental verification of this conclusion is recommended.

(5) Once the molten Zry relocates to the bottom of the PT, a hot spot is created that causes the PT to bulge out radially under the effect of the reactor pressure. The PT may come in contact with the CT, which heats up, bulges and eventually fails. The inception and speed of the PT/CT bulging and ultimately the likelihood of failure depend strongly on the postulated mass of molten Zry in contact with the PT, and on the value of the thermal resistance at the Zry/PT interface. It was found that a Zry mass ≤10 g will not cause PT/CT failure regardless of the contact resistance effect. On the other hand, a mass of 100 g would be sufficient to cause PT/CT failure even in the presence of a thick 0.2 mm oxide layer at the interface. The characteristic time scales for this 100-g case are as follows:

- PT bulging starts within 3 s of Zry/PT contact
- PT makes contact with the CT in another 2 s
- CT bulging starts in less than 1 s
- CT failure occurs within another 5 s.

Thus, the duration of the PT/CT deformation transient is 11 s, which gives a total duration of the accident (from PT blockage to PT/CT failure) of 18 to 21 s.

ACKNOWLEDGEMENTS

This work was supported by the U.S. Nuclear Regulatory Commission (NRC) through Collaborative Agreement NRC-04-02-079.

CONTENTS

LIST OF FIGURES

LIST OF TABLES

1. INTRODUCTION

The ACR-700 is an advanced pressure-tube (PT) reactor being developed by Atomic Energy of Canada Limited (AECL). As in conventional CANDU reactors, the PTs are horizontal and each accommodates 12 circular fuel assemblies (FAs) 495 mm in length. Each PT is surrounded by a calandria tube (CT). The space between the CTs is filled with the heavy-water moderator. Unlike traditional CANDUs, however, the ACR-700 utilizes slightly enriched uranium fuel and light-water coolant in lieu of natural uranium fuel and heavy-water coolant. Also, the operating temperatures and pressure have been increased to enhance the thermal efficiency. A diagram depicting the layout of the ACR-700 reactor coolant system is included in Figure 1, and a diagram describing the arrangement of the fuel channel is included in Figure 2.

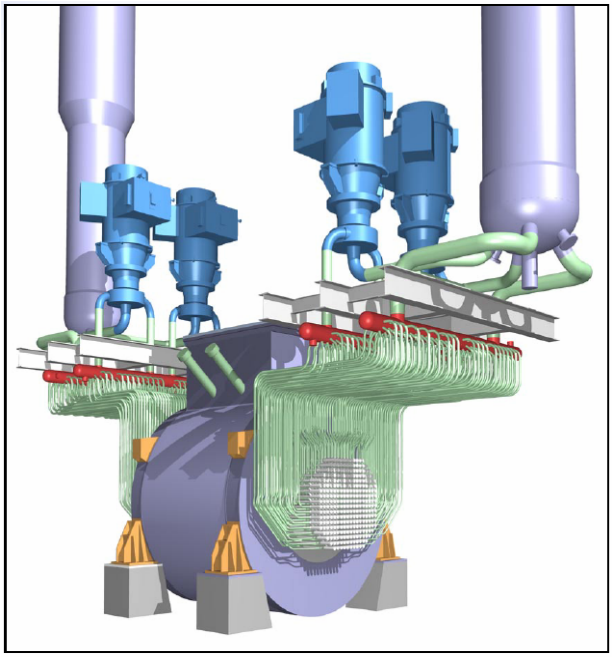

Figure 1: ACR-700 Reactor Coolant System [1]

One postulated accident scenario for ACR-700 is the complete coolant flow blockage of a single PT. The flow is not monitored within each individual PT, thus during the early stages of this accident the reactor remains at full power, resulting in rapid coolant boil-off

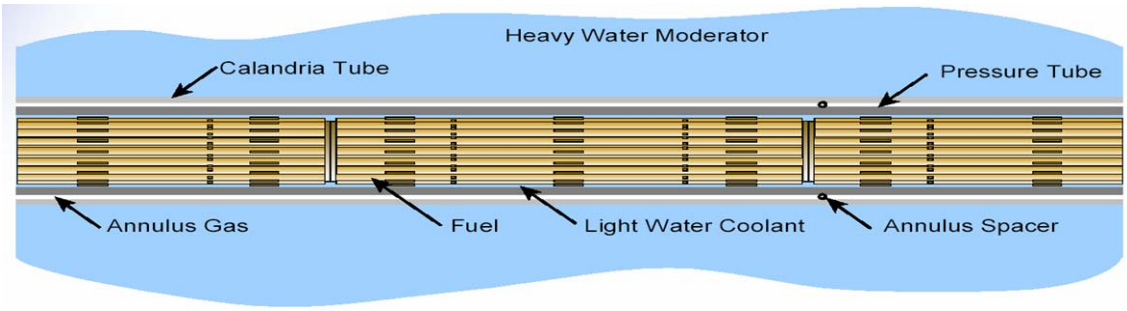

Figure 2: ACR-700 Fuel Channel [1]

and fuel overheating. Melting of the Zircaloy (Zry) components of the fuel bundle (cladding, end plates and end caps) can occur, with relocation of some molten material to the bottom of the PT. The hot spot caused by the molten Zry/PT interaction may cause the PT to bulge radially due to localized plastic strains. Under certain conditions, the PT may come into contact with the CT, which will heat up, and eventually fail. PT/CT failure results in depressurization of the primary system, which triggers a reactor scram, after which decay heat is removed via reflooding, thus PT/CT rupture effectively terminates the accident. Clearly, prediction of the PT/CT time-to-failure is of great importance for this accident. A diagram depicting the beginning stages (prior to CT failure) of this fuel channel degradation is included in Figure 3. A brief overview of the sequence of steps considered and their associated key phenomena is provided in Table I.

Figure 3: Degradation of ACR-700 fuel channel and PT rupture [1]

This report first describes the energy transport phenomena involved during coolant boiloff, cladding melt, and PT rupture. These phenomena include conduction, convection and radiation heat transfer in the fuel-cladding-steam system and between the molten material and the PT. The Zry/steam reaction at the Zircaloy surface and the dissolution of UO_2 at the Zry/fuel interface have also been analyzed. The geometry of the molten material in contact with the PT wall have been evaluated. The heat conduction between the molten drop and PT wall along with the resulting creep-induced local strains in the PT have been determined as the dominant mechanisms for PT failure in this scenario.

Table I: Key steps considered and associated phenomena

Sequence	***Phenomena***
Coolant Boiloff	• Energy of Evaporation
Fuel Pin Heatup / Cladding Melt	• Energy Redistribution • Fission Heat • Radiative Heat Transfer • Convective Heat Transfer • Zry/Steam Chemical Reaction • Holdup Effects Preventing Molten Zry Relocation
Molten Zry/PT Interaction	• Zry Solidification • Radiative Heat Transfer • Convective Heat Transfer • Zry/Steam Chemical Reaction • Conduction Between Zry/PT • ZrO_2 Contact Resistance
PT Failure	• Creep Strain • PT Bulging/Failure • PT/CT Contact
CT Failure	• Conduction between PT/CT • Nucleate and film boiling on CT surface • Creep Strain • CT Bulging/Failure

A three dimensional COSMOSM finite-element model was developed to model the thermal portion of the molten Zry interaction with the PT and CT. The thermal models include all the important phenomena such as molten droplet solidification, convection and radiation within the gas annulus and on the outer surface of the CT, and the molten Zry/steam reaction. A parametric study was completed on the effect of the presence of a contact resistance between the Zry and PT due to an oxidized layer on the PT surface.

A three dimensional analytical model describing the bulging of both the PT and CT was implemented in MATLAB. This bulging was assumed to occur with spherical symmetry

and the thickness in this region was assumed to be uniform, though varying with time. This analysis enabled the prediction of PT/CT contact and CT failure, which, for this study, was assumed to be the final step of the transient.

It is important to note that most analysis in the area of molten material/PT interaction [2, 3] has involved the assumption of large amounts of molten Zry (~10-25 kg) contacting the PT and then focused on the magnitude of failure propagation to neighboring fuel channels. The present best estimate analysis focuses on understanding the impact of small droplets falling from the fuel rods, which would accumulate much sooner than large inventories. Failure propagation is not investigated in our study; however, the PT/CT time-to-failure results of this study can serve as input information for best-estimate failure propagation analyses requiring the initial molten Zry inventory.

The report is structured as follows. A summary of the results for cladding melt and molten Zry/PT interaction is reported in Sections 2 and 3, respectively. A detailed description of all models and analyses is provided in Appendices A and B.

2. INVESTIGATION OF THE PHENOMENA LEADING TO CLADDING MELT AND RELOCATION TO THE BOTTOM OF THE PT

2.1. COOLANT BOIL-OFF

The postulated initiator for this event is a complete (e.g. 100%) blockage of flow at the inlet of a single pressure tube (PT). The reactor remains at full power and pressure (12.6 MPa) since flow is not monitored in individual PTs. The flow of water into the PT is assumed to cease upon accident initiation causing coolant vaporization to occur almost immediately.

Using a heat of evaporation of 1321 kJ/kg and a peak channel power of 7.293 MW, it was calculated that the coolant inventory completely evaporates in about 2.8s. A detailed description of the calculations used in this analysis is included in Section A.1.

2.2. ENERGY REDISTRIBUTION WITHIN THE FUEL PIN

Once a fuel pin is uncovered, the convection coefficient becomes very low, and radiative heat transfer to the surrounding pins and the PT wall is also negligible in the first few seconds of the ensuing heat-up. Thus, the radial temperature profile within the fuel flattens rapidly. This energy redistribution occurs with a time constant of 1.4 s (see Section A.4), which was calculated by solving the transient heat conduction equation for the fuel pin with the assumptions of negligible cladding thermal capacity and thermal resistance (thin cladding – Section A.4 & A.5), and negligible gap resistance ('collapsed' cladding). This means that roughly 1.4 s after a pin is uncovered, its cladding reaches a temperature equal to the radial average of the UO_2 temperature prior to the accident initiation. This temperature is about 680°C, and was calculated with the Babcock and Wilcox UO_2 thermal conductivity correlation [4] for a fuel pin operating at 37.9 kW/m linear power, which is

estimated to be the peak linear power for ACR-700 (see Section A.2). Therefore, 680°C is the initial condition for the fuel pin heat-up calculations that follow.

2.3. CLADDING AND FUEL MELT

The fuel pin of maximum linear power is considered to begin heating up upon uncovery. The governing equation includes three terms: fission energy production, radiation heat loss and an energy storage term:

$$\rho C_p \frac{\pi}{4} D^2 \frac{dT}{dt} = q'_f - \pi D \varepsilon \sigma (T^4 - T_\infty^4) \tag{2.1}$$

where ϱ,C_p, D, q'_f, ε, σ, and T_∞ are the density, heat capacity, diameter of the pin, maximum linear heat generation rate, emissivity of the cladding, Stefan-Boltzmann constant, and the surroundings temperature respectively.

The values of the parameters used in the calculations are listed in Table II. The upper PT wall temperature is assumed to be a suitable representative surroundings temperature for the purpose of calculating radiation heat transfer. During the severe flow blockage event this temperature is of the order of 500 °C, as found in the ACR-700 Severe Flow Blockage PIRT [5]. A sensitivity analysis has shown that our results are not very sensitive to this temperature, so a very accurate value is not necessary.

Solving Equation (2.1), it was found (Section A.7) that the Zircaloy cladding reaches its melting temperature in approximately 10 seconds when radiation cooling is considered and approximately 6.7 seconds not including radiation cooling (Figure 1). It is expected that the actual melting time of the cladding will lie between these two values since the topmost pins will be uncovered first but also will be cooled by radiation better, compared to inner pins. UO_2 melt would occur much later, due to its higher melting point (Section A.8).

Detailed calculations concerning the time to cladding and fuel melt are included in Appendix A.

Table II: Reference ACR-700 Parameters

Parameter	Value
Thermal Power (MWth)	1980
Gross Electric Power (nominal) (MWe)	731
Reactor Pressure (MPa)	12.6
Nominal Coolant Inlet Temperature (ºC)	279
Nominal Coolant Outlet Temperature (ºC)	325
Length of Fuel Bundle (mm)	495.3
Core length (mm)	5940
Number of Bundles per Fuel Channel	12
Number of Fuel Channels (PTs)	284
Pressure Tube Inner Radius (mm)	51.689
Pressure Tube Outer Radius (mm)	58.169
Number of Fuel Elements per Channel	43
Lattice Pitch (mm)	220
Fuel Pin Outer Diameter (mm)	11.5
Peak Power of a Single Pin (kW)	219
Maximum Linear Heat Generation Rate (kW/m)	37.9
Peak Channel Power (MW)	7.293
Melting Temperature of Zr (ºC)	1760
Melting Temperature of UO_2 (ºC)	2850
Initial Average Fuel Pin Temperature (ºC)	680
Upper PT Wall Temperature (ºC)	500
Fuel Density (95% Theoretical) (kg/m^3)	9186
Average Fuel Thermal Conductivity (W/mK)	3.64
Fuel Heat Capacity (J/kgK)	247
Emissivity of Cladding	0.80

2.4. HOLDUP EFFECTS PREVENTING MOLTEN CLADDING RELOCATION TO THE BOTTOM OF THE PRESSURE TUBE

The amount of oxygen present at the interface of the Zircaloy cladding and UO_2 at the time of Zircaloy melting greatly influences the progression of the accident, because molten Zircaloy wets UO_2 in the presence of oxygen [6]. This can prevent molten Zry relocation

from the cladding to the bottom of the PT. If this happened, the fuel assembly end caps and end plates, which are also made of Zry, would eventually melt and relocate on the PT, but this would prolong the accident and likely generate more molten material. The holdup phenomena investigated in this report are summarized in Table III, and discussed in further detail below. Figure 5 provides a sketch of where these holdup mechanisms are taking place with respect to the fuel channel geometry.

Table III: Holdup effects investigated in this report

Phenomenon	**Dissolution of UO_2 fuel by molten Zry**	**Zry/Steam Reaction**	
Effect	Raise oxygen content in Zry	Raise oxygen content in Zry	Solid ZrO_2 sheath created surrounding Zry
Holdup mechanism	Zry will 'wet' UO_2, clinging to the pellets preventing drip	Zry will 'wet' UO_2, clinging to the pellets preventing drip	Sheath encapsulates molten Zry preventing drip
Prevent Zry drip in single channel flow blockage event?	No. Heatup rate sufficiently fast to limit oxygen diffusion [8]	No. Oxygen penetration into cladding small compared to overall clad thickness	Not likely. Heatup rate sufficiently fast to cause quick inter-element contact allowing Zry drip from these contact points [3, 10]

The first phenomenon that could prevent molten Zry drip is the diffusion of oxygen to the cladding/fuel interface from the oxide layer on the outer surface of the cladding (due to the Zirconium/Steam reaction) or from the UO_2 pellet.

The Zirconium/Steam reaction is exothermic and releases hydrogen[1]:

$$Zr + 2H_2O \rightarrow ZrO_2 + 2H_2 + 587\,{}^{kJ}/_{mol\,Zr} \tag{2.2}$$

The oxidation rate for Zircaloy-4 in steam is given by Urbanic [7]:

$$\frac{d\xi}{dt} = \frac{\delta^2}{2\xi} \tag{2.3}$$

[1] Incidentally, we shall notice that the contribution of this reaction to the fuel pin heatup is completely negligible with respect to the fission heat.

where ξ is the thickness of the region through which oxygen has penetrated and $\delta_{\xi T}$ is a temperature-dependent factor:

$$\delta_{\xi_T} = 0.363e^{\left(\frac{-8968}{T}\right)} \tag{2.4}$$

in the temperature range 1050-1580 ºC, and

$$\delta_{\xi_T} = 0.251e^{\left(\frac{-7764}{T}\right)} \tag{2.5}$$

in the temperature range 1580-1850 ºC.

Using the temperature curve that includes radiative cooling in Figure 4, Equations (2.3), (2.4), and (2.5), the growth of the oxide layer can be calculated (Section A.9) and is shown in Figure 4. The overall thickness of the oxide layer expected by the time of melt is approximately 97μm, or 16 percent of the overall thickness of the cladding. This demonstrates that oxygen penetration into the cladding due to Zirconium/steam oxidation has negligible impact on molten Zircaloy-4 reolaction to the PT bottom. In this calculation, we made the assumption that at the time of the accident the cladding thickness is already 10% oxidized. Likely this is a significant overestimate of the actual initial oxidation, because CANDU FAs are not kept in reactor long enough to develop such high oxidation. However, a sensitivity analysis, included in Section A.15, has shown that the final value of the oxide layer thickness is fairly independent from the initial value, because of the form of Equation (2.3).

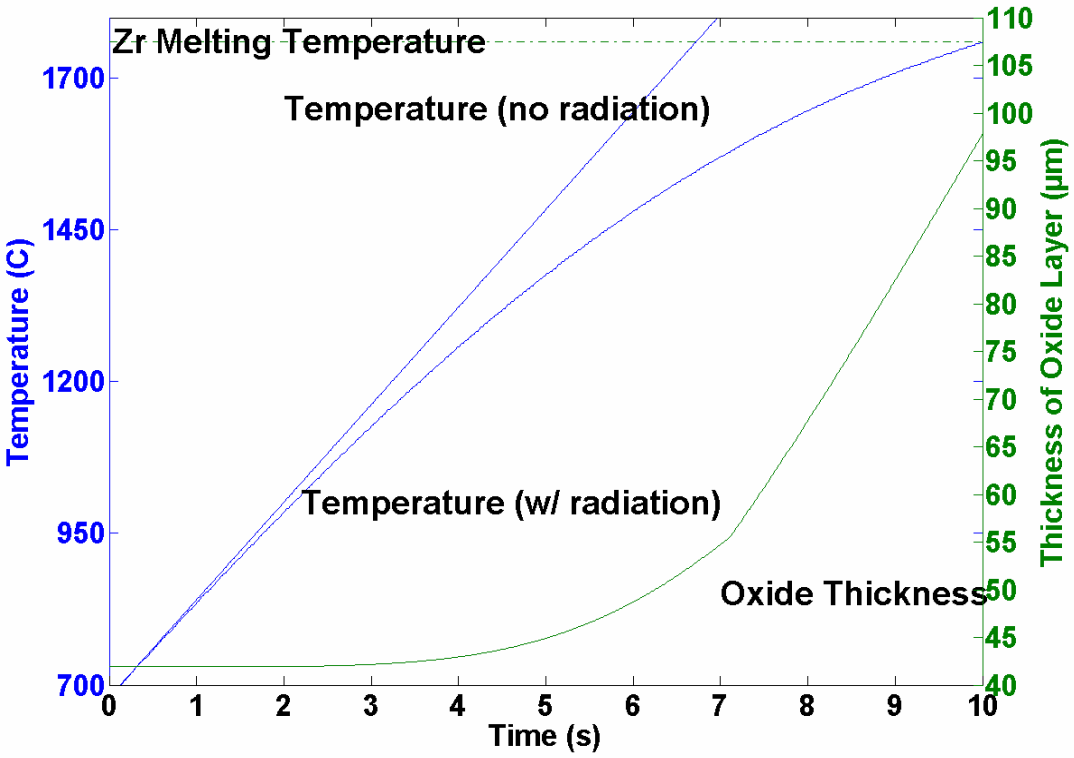

Figure 4: Oxide Layer Thickness and Cladding Temperature Profile during Fuel Heat-up

The second phenomenon resulting in increased oxygen content within the fuel cladding is the dissolution of solid UO_2 by molten Zircaloy-4 cladding. The driving force for this reaction is the diffusion of oxygen from the UO_2 into the cladding. This reaction predominantly occurs above the melting point of Zircaloy-4 (1760 ºC). Rosinger et al. [8] observed that molten Zircaloy does not wet UO_2 if the heating rate is sufficiently high, i.e., there is very little time for UO_2 to dissolve in the Zircaloy. The critical heating rate in their experiments was around 35 °C/s. Further, Dienst et al. [9] showed that the interaction of molten Zircaloy-4 with UO_2 at 1800°C in an inert atmosphere is insignificant for the first 80 s. Because the heating rate during the complete flow blockage is very high (about 140 °C/s, as seen in Figure 4) and the duration of the cladding heat-up is very short (<10 s, as seen in Figure 4), it can be concluded that, upon reaching its melting temperature, the majority of unoxidized Zircaloy-4 melts and does not wet the UO_2.

An additional effect that could prevent dripping of the molten Zry from the fuel pins is the presence of the oxide layer on the outer surface of the cladding, which could act as a solid sheath to prevent dripping. This sheath has been shown [3, 10] to form and act as a barrier

to fuel relocation. Nevertheless, for sufficiently high heating rates, cladding relocation is known to occur [10]. The experimental critical heating rate was 10 °C/s. The suggested mechanism for relocation is through localized steam starvation along inter-element contact points, which creates sites of thin or nonexistent oxide shell thereby acting as a path for molten material flow [3]. Fuel element geometry has been shown to disassemble and cause inter-element contact (as shown in Figure 5) at temperatures ranging from 1200-1400 °C, which is considerably earlier in the transient than cladding melt [10]. Since this transient has an extremely high heating rate and fuel element contact is expected to occur, it is reasonable to predict cladding relocation[2]. Experimental verification of this phenomenon and its time scale under the conditions expected during the single-channel flow blockage event are warranted, however, to provide satisfactory confidence in our conclusion.

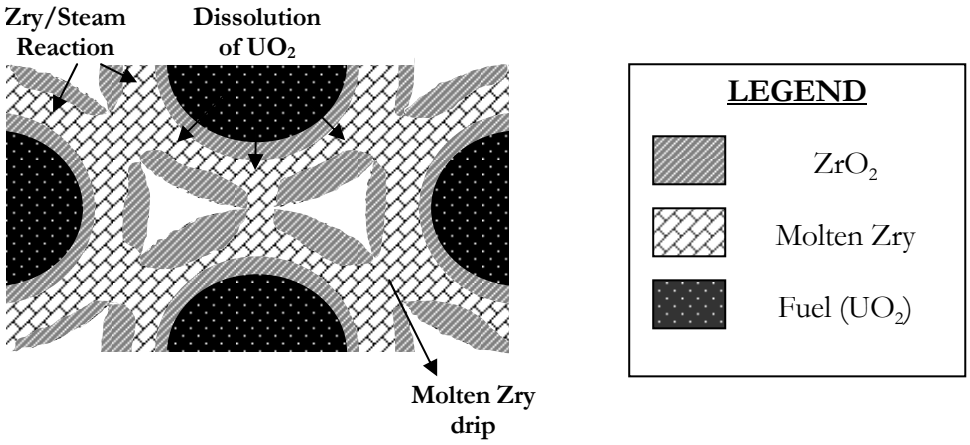

Figure 5: Axial cutaway of four fuel pins in disassembled fuel channel depicting possible holdup mechanisms

2.5. DISCUSSION

A summary of the important representative time scales leading up to molten Zry/PT contact are given in Table IV.

The time range of 7-10 seconds until the beginning of some channel deformation is consistent with the range given by the ACR-700 PIRT [5] of 8 seconds. Overall, these simplified one-dimensional results are in good agreement with the findings of the much

[2] In contrast, for longer transients with comparatively low heating rates such as a large-break loss of coolant accident (LB-LOCA) with failed emergency core cooling system (ECCS), there is sufficient time for the molten cladding to wet UO2, and not drip as discussed in Rosinger et al [8].

more sophisticated calculations used by AECL. These results should give confidence in verification of AECL's tools for analyzing this accident scenario and give better understanding to the individual segments of this accident. The analysis discussed in Chapter 3 will complete the study of the sequence with a look at the molten Zry/PT and PT/CT interactions.

Table IV: Important Time Scales in the Early Stages of the Single-Channel Flow Blockage Event

Process	Time (s)
Coolant inventory boil-off	2.8
Fuel cladding melt	6.7-10
Total: accident initiation to Molten Zry/PT contact	7-12

3. INVESTIGATION OF MOLTEN ZRY/PT INTERACTION, AND PT/CT BULGING

A first attempt to analyze the molten Zry/PT interaction with simple one-dimensional models was presented in [11]. However, this interaction is a complex process involving multiple energy transfer mechanisms and three-dimensional effects. Therefore, a more complete analysis was performed and is presented here.

Full three dimensional models must be used to properly model the heat transfer within the PT as axial and circumferential conduction acts as a significant heat sink. Molten Zry solidification and convection and radiation heat transfer are also best modeled via three dimensional modeling. Bulging of the PT also requires three-dimensional modeling due to the localized nature of the straining.

Once the molten cladding has relocated to the bottom of the PT, the situation can be represented as small droplets of liquid Zircaloy in contact with the Zr-2.5wt% Nb PT. The PT surface has a ~0.1mm thick zirconium oxide layer deposited as part of the manufacturing process [8]. To determine the geometry (height, surface area, and contact diameter) for various Zry droplet masses, a model based on the Young-Laplace equation [13] was used. The contact angle, θ, between zirconium oxide and molten Zircaloy-4 was assumed to be approximately 120 degrees (see Figure 6), as estimated from the contact angle data for molten zirconium droplets on various oxides in reference [12]. This drop geometry model is discussed in detail in Section A.11 and validated using oil and water on several surfaces in Section A.12.

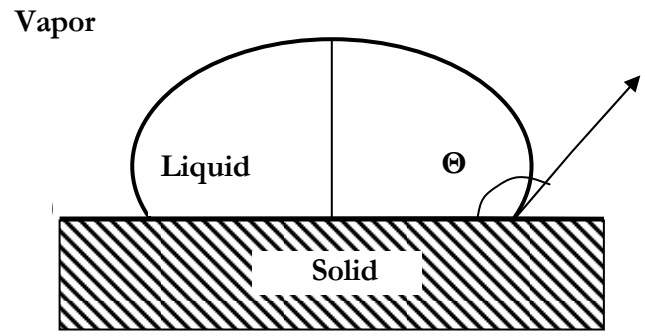

Figure 6: Contact angle for equilibrium solid-liquid-vapor system

3.1. THERMAL MODEL

Thermal analysis of Zry/PT contact was completed using a three dimensional COSMOSM finite element model. The mesh, material properties, boundary conditions and loading used in the COSMOSM model are discussed next.

Model Geometry

The three dimensional solid model of the PT and molten mass were created using version 2004 SP5.0 of the computerized aided design (CAD) program, SolidWorks [14]. This CAD model was then imported into version 2.85 of the COSMOSM finite element code [15]. Only a quarter section of the system was modeled as shown in Figure 7 and Figure 8. This standard model used 9209 elements and 16118 nodes. A 10-node three dimensional tetrahedral solid element (TETRA10) was used for the thermal analysis. Only one degree of freedom per node, representing the temperature, is used. The model was automatically meshed using the high quality 4-point Jacobian method. The mesh density was higher near the melt to improve solution accuracy in this area of high thermal gradients. Several mesh densities were tested from coarse to very fine, with the final result shown in Figure 7 and Figure 8 being sufficiently accurate without requiring excessive computation time.

The axial length of the model is 100 mm, which is sufficiently longer than the typical size of the molten Zry drop, so that the temperature distribution is not affected by the boundary conditions at the ends, over the time scale involved (i.e., < 20 s).

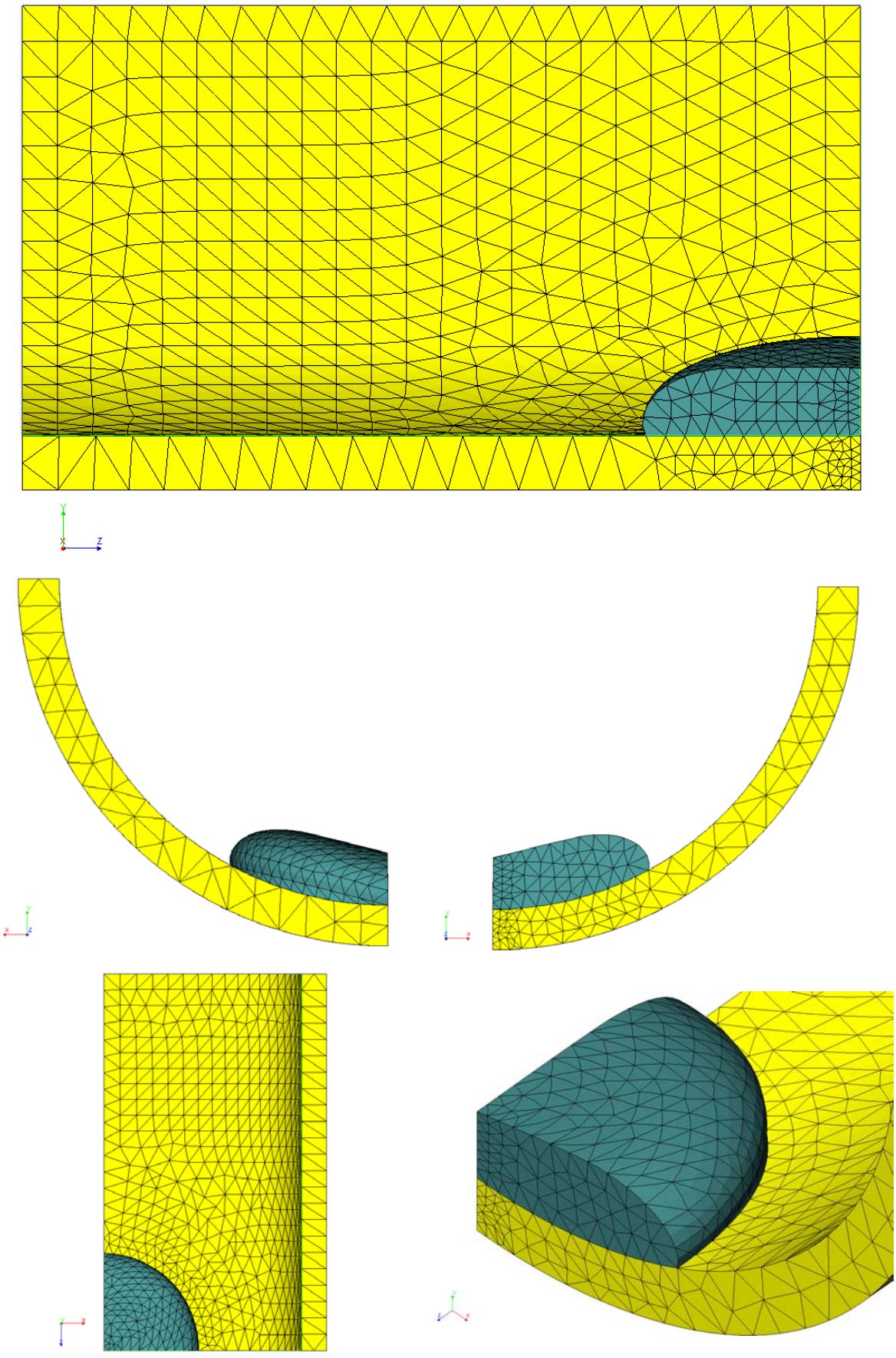

Figure 7: Several Views of COSMOSM Thermal Mesh – 100g Zry & PT

The molten Zry was assumed to be in place on the inside of the PT throughout the simulation.

Melt geometry was determined using the cross section calculated using the Young-Laplace model as discussed in Section A.11 and imported as a two-dimensional sketch within SolidWorks. This cross section was then used to form a quarter portion of the droplet. Steps were taken to ensure that values for volume and surface area were maintained when placing this droplet in contact with the curved PT surface.

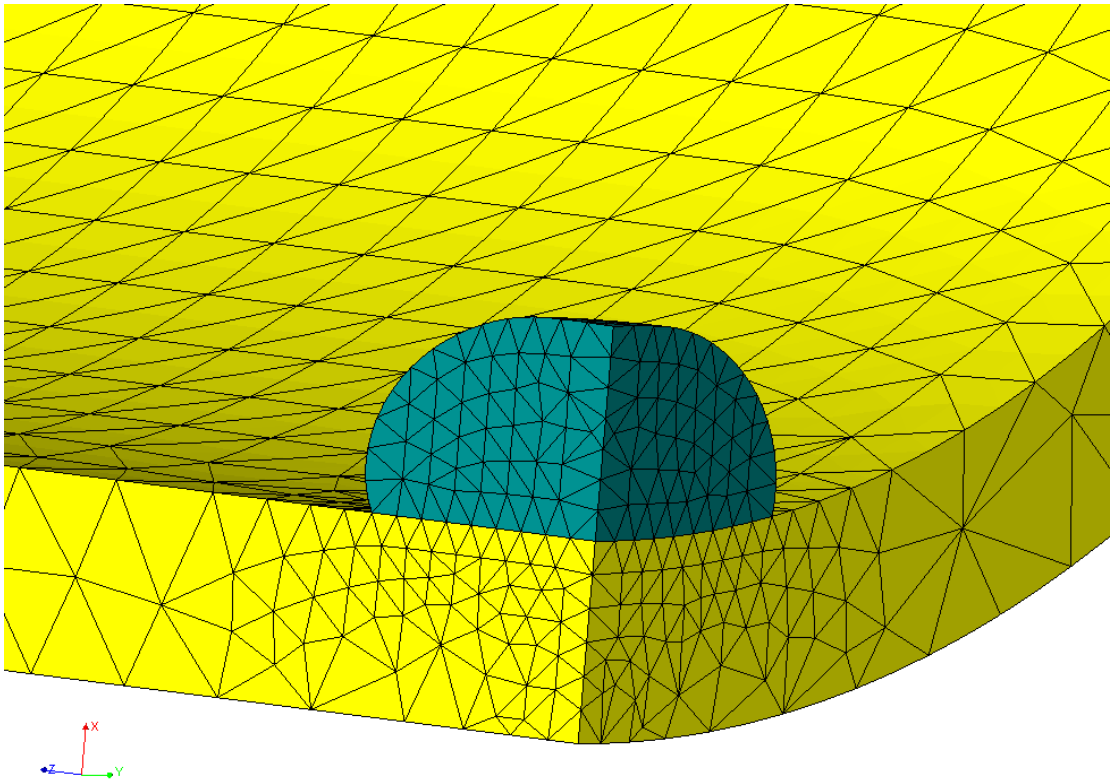

Figure 8: Thermal Mesh – 10g Zry & PT

For some runs (discussed in Section B.5), a thin contact resistance at the interface of the PT surface and the molten Zry was included. As discussed in the previous chapter, the inside of the PT is oxidized during the manufacturing process so that an approximately 0.1mm thick layer of ZrO_2 is in place. This oxide layer inhibits heat transfer and is an important parameter. A parametric study was completed (Section B.5) studying the affect of various oxide thickness on heat transfer. An oxide thickness of 0.2mm was used as the best-estimate thickness in this report.

Thermal analysis modeling the PT bulge coming into contact with the CT was also completed for several runs. A detailed discussion is included in Section B.9.

Material Properties

Material properties were required for the PT, CT and molten Zry. These properties include density, thermal conductivity, specific heat, enthalpy and emissivity. Values used are shown in Table V. Zry freezing was modeled as a specific heat spike at the melting temperature of 1760 °C, as discussed in Section B.2.

Table V: Physical Properties of Model Entities

Parameter	Molten Zry	Pressure Tube	Calandria Tube
Density (kg/m^3)	6500	6570	6440
Thermal Conductivity (W/m^2K)	50	16	16
Specific Heat (kJ/kg)	356 [3]	307	307
Emissivity	0.80	0.70	0.70

Boundary and Initial Conditions

Time zero for all cases is the time when molten Zry/PT contact is made.

The PT was assigned an initial temperature of 328 °C which was taken as the PT bottom nominal temperature from [5]. The molten Zry was assigned an initial temperature of 1762°C. This value is two degrees higher than the melting temperature of Zry, which is necessary to allow for proper modeling of the heat of fusion as discussed in Section B.2.

Radiation and convection heat transfer were considered from the PT outer surface to properly simulate the effect of the gas annulus that separates the PT and CT. The convection coefficient was assumed to be 10 W/m^2K and the emissivity 0.70 as discussed in Section B.4. The temperature of the moderator on the outer surface of the CT was

[3] Nominal value – heat of fusion is incorporated into this value at the melt temperature of Zry (see Section B.2)

assigned a constant value of 74 °C which was taken as the nominal moderator temperature from [2]. The CT was assigned this same value of 74 °C as an initial temperature.

Investigation of the effect the Zry/steam reaction occurring on the outer surface of the molten Zry may have on time to failure is discussed in Section B.11, while a description of the formulation of this boundary condition is included in Section B.3.

Convection and radiation are also considered from the outer surface of the CT when localized PT/CT contact has been made due to PT bulging as discussed in B.10. Both nucleate pool boiling and film boiling heat transfer are considered. For nucleate boiling, a heat transfer coefficient ranging from 10,000 to 40,000 W/m^{2}K was chosen, based on estimates using the correlations from Zuber and Rosenhow [4]. Since these high convection coefficients keep the wall surface temperature relatively low, radiation was not considered for nucleate boiling. The film boiling convection coefficient of 350 W/m^{2}K was estimated using the horizontal cylinder film boiling correlations from [16] which includes Bromley's transcendental equation incorporating radiation heat transfer. An emissivity of 0.70 was used for the CT outer surface.

3.2. STRUCTURAL MODEL

The structural model used to study the PT and CT bulging due to localized creep strains assumed spherical symmetry of the bulging region. The time dependent membrane stresses were calculated accordingly.

Shewfelt [17] provides the high-temperature creep equation for Zr-2.5 wt% Nb. In the temperature range from 450ºC to 850ºC the creep rate is:

$$\dot{\varepsilon} = 1.3x10^{-5}\sigma^{9}e^{(-36600/T)} + \frac{5.7x10^{7}\sigma^{1.6}e^{(-29200/T)}}{\left[1+2x10^{10}\int_{t_1}^{t} e^{(-29200/T)}dt\right]^{.42}} \tag{3.1}$$

and in the temperature range of 850-1200 ºC it is:

$$\dot{\varepsilon} = 10.4\sigma^{3.3} e^{(-19600/T)} + \frac{3.5x10^4 \sigma^{1.4} e^{(-19600/T)}}{\left[1 + 274\int_{t_2}^{t} e^{(-19600/T)} \cdot (T - 1105)^{3.72} dt\right]} \quad (3.2)$$

where $\dot{\varepsilon}$, σ, t_1, and t_2 are the logarithmic creep strain rate, applied stress (MPa), time where the temperature is above 450°C, and time where the temperature is above 850°C respectively.

The tangential and radial creep strain rates in the bulging region were calculated using the deviatoric stress tensor and the one dimensional creep strain rates of Equation (3.1) and (3.2), time-integrated with an implicit method. It is then possible to use the geometry describing the straining of the spherical bulge for each time step to calculate a new radius of curvature for the bulge. Finally, the new thickness in the bulging region is calculated from the conservation of volume typical of creep strains. This allows for the growth history of the bulging area to be predicted until theoretical failure (37% reduction in wall thickness [18]) is achieved. An example of the bulging results obtained with this model is shown in Figure 12, which depicts the reduction in wall thickness vs. time for the best-estimate 100g Zry droplet case. A more detailed discussion of the procedure, theory and validation of the bulging model is included in Sections B.6 through B.9.

Since the gap between the PT and CT is small (17.3 mm), PT bulging models predict that contact will be made prior to PT failure. Since the bulging area is extremely compliant, once contact is made, the pressure load is transferred locally from the PT to the CT. As the CT is heated, it too begins to bulge until it fails. CT failure is assumed to be the end of the transient, since the resulting release of steam from the fuel channel is quickly detected and the reactor will scram.

3.3. ANALYSIS & RESULTS

The complete algorithm for the three dimensional simulation is detailed in the flowchart of Figure 9. The molten Zry/PT thermal analysis is calculated using COSMOSM. The result of this thermal analysis is then input into the PT bulging model. If PT/CT contact is not made then failure of the PT only is considered. If the PT wall thickness is not reduced by

37%, then failure is not expected to occur, and the transient dissipates. If the wall thickness is reduced by 37% then the PT is predicted to fail, pressurizing the annulus gap. At this point, the CT must bulge and fail the accident to terminate since merely failing the PT is not sufficient for immediate CT failure or accident detection, according to B. Sanderson [personal communication, April 4, 2005].

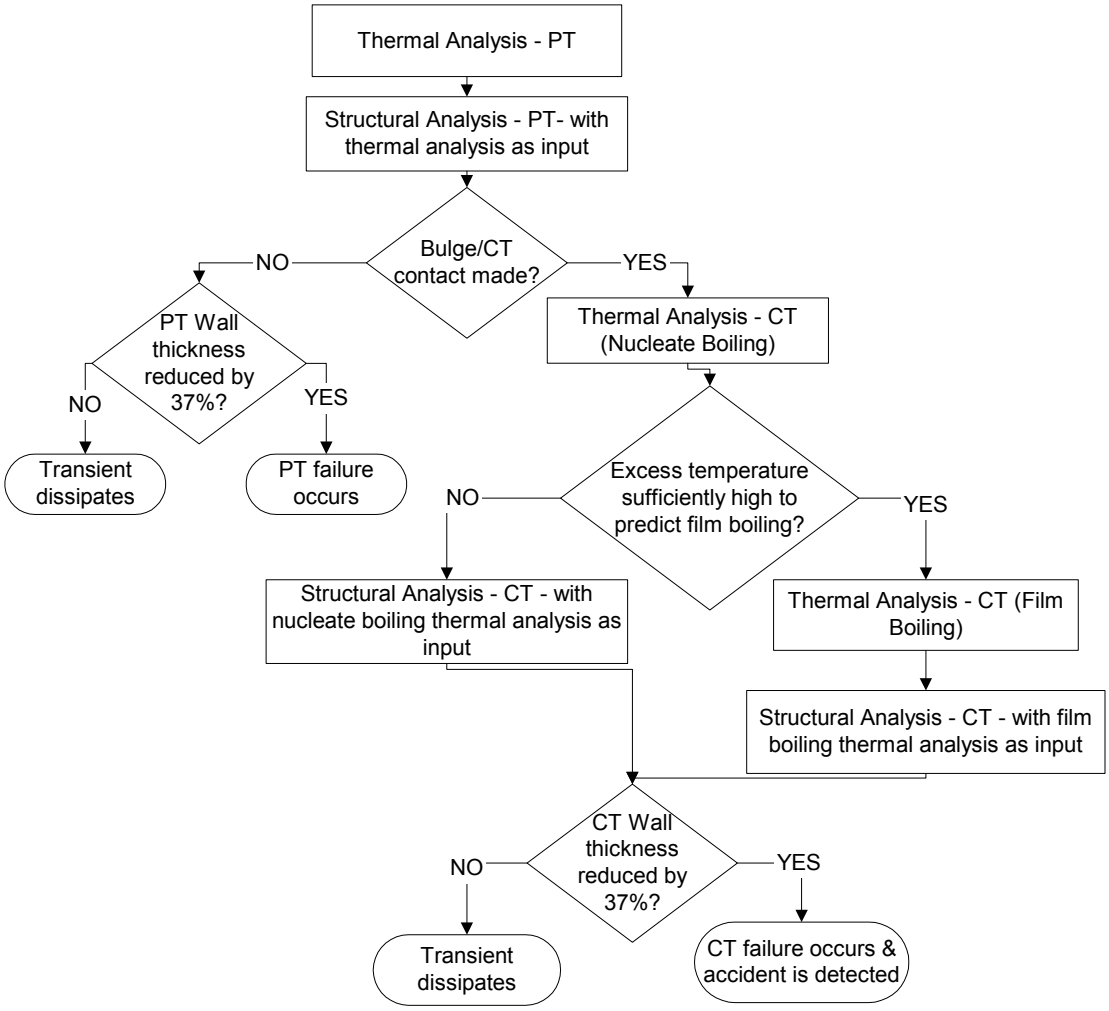

Figure 9: Flowchart of complete analysis process

If PT/CT contact is made, then a thermal simulation in COSMOSM which will include the CT along with molten Zry and PT is run that assumes nucleate boiling from the outer CT surface. If the wall superheat at the CT wall and bulk temperature is not high enough to predict film boiling, then this thermal result is plugged into the MATLAB bulging model. If the wall superheat is sufficiently high, another thermal analysis is completed using COSMOSM, this time assuming film boiling on the outer surface of the CT. This thermal result is then plugged into the MATLAB bulging model where the thickness of the CT wall

is then analyzed. If the thickness is not reduced by 37%, then failure of the CT is not expected to occur. If wall thickness is reduced by 37%, then CT failure occurs, and accident detection and scram will take place.

Thermal Results

An important objective in this study was to better understand what effects different size masses of molten Zry will have on PT/CT failure. To this end, a thermal analysis was completed comparing the temperature history at a point in the middle of the PT wall when a 1, 10 and 100g mass of molten Zry is placed on the PT wall. This analysis was three dimensional, included solidification of the droplets, and assumed that there was no Zry/steam reaction, an adiabatic boundary condition on the exterior of the PT and no contact resistance between the molten Zry and PT. The results are shown in Figure 10.

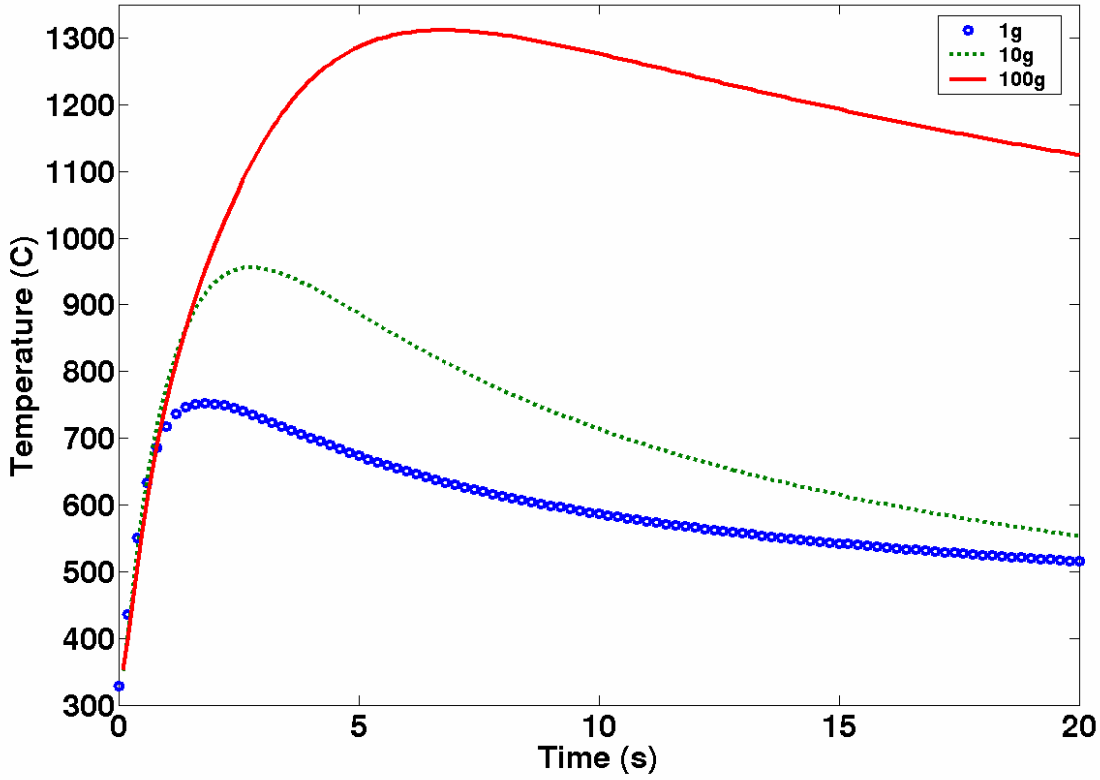

Figure 10: Comparison of temperature histories in middle of PT wall for 1, 10 and 100g molten Zry drops.

It is interesting to note that there is little difference in the temperature histories for approximately the first second of heatup, after which the 1g and 10g curves quickly level out compared to the 100g curve.

The effect of a contact resistance between the molten Zry and PT inner surface is pronounced. For the ZrO_2 thicknesses investigated: 0.02, 0.2, and 2.0 mm, temperature differences on the outer surface of the PT of several 100 degrees can be expected, as shown in Figure 11, which clearly has a large impact on time to failure. This effect is discussed in more detail in Section B.5. This study shows that for oxide thicknesses less than 20μm, the temperature history is unaltered, as would time to failure. For oxide thickness greater than 200μm, however, the temperature history is reduced and softened, which is expected to alter time to failure. Since the expected oxide thickness on the inner surface of the PT is 0.1mm, but the exact thickness between the PT and molten Zry is not known with certainty, this sensitivity study is extremely important and is included in the structural analysis in Section B.11.

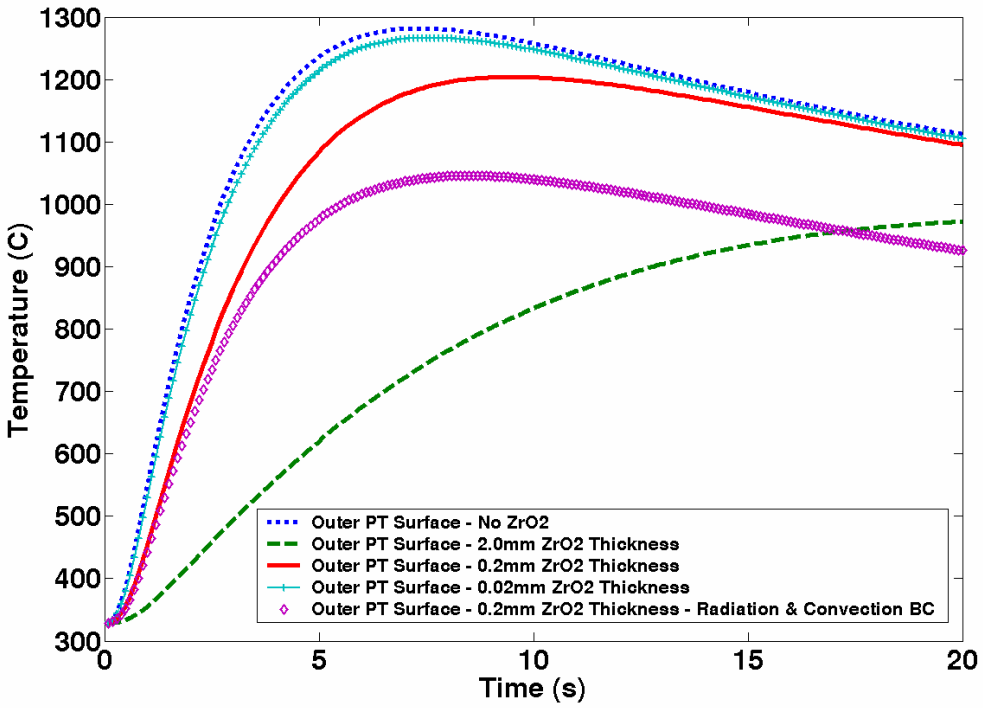

Figure 11: Thermal Contact Resistance Analysis: Outer PT Surface Comparison

Bulging Results

The first important result obtained from the structural analysis is that there is a minimum mass of molten Zry necessary to result in PT, and ultimately CT, failure as shown in Section B.11. A sample of the results obtained through this analysis is shown in Figure 12. This figure depicts the displacement, wall thickness reduction, Von Mises stresses, and radius of curvature history for the PT in the best-estimate case. The PT is expected to make local contact with the CT in approximately 5.3 seconds.

No case under 100g is predicted to fail the PT. All 100g cases result in failure of the PT and CT except in the case with 2.0mm of ZrO_2 on the PT surface. Thus, this analysis shows that in order for failure of the PT/CT to occur, the molten droplet's mass must be greater than 10g. The time required for failure is dependent on the boundary conditions assumed. For 100 g droplets, failure of the PT and CT is expected to occur somewhere between 7.5 and 11 seconds after molten Zry contact with the PT depending on the boundary conditions and ZrO_2 thickness assumed.

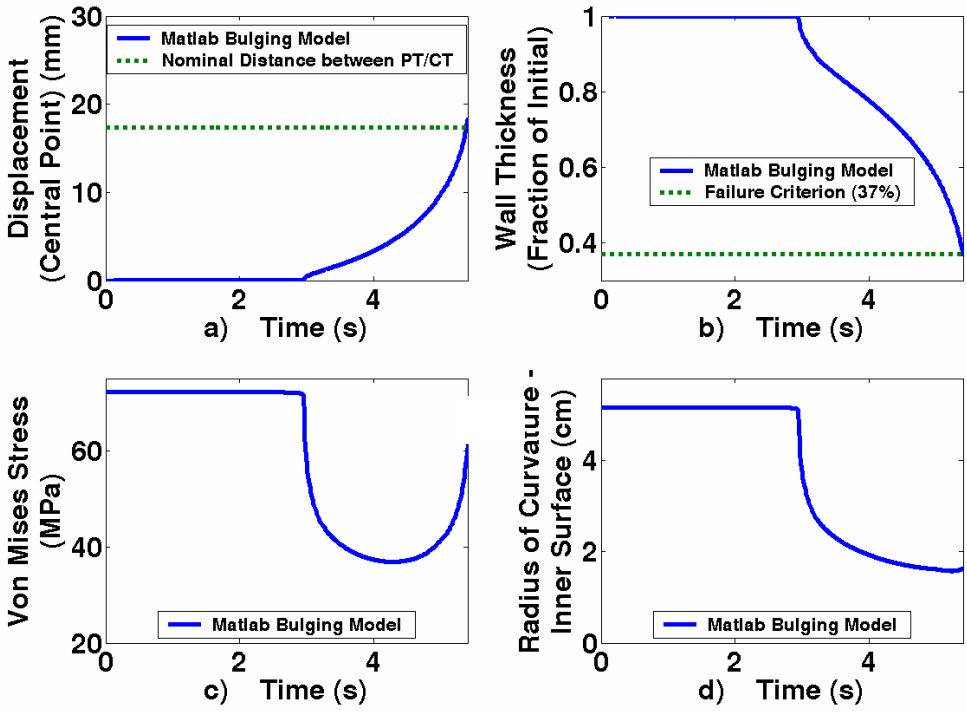

Figure 12: Best-estimate 100g Zry droplet case results. a) Displacement of PT central point, b) Reduction in PT wall thickness, c) Von Mises membrane stress in PT bulge, d) Radius of curvature (inner PT)

4. CONCLUSIONS AND FUTURE WORK

The single-channel complete flow blockage event in ACR-700 results in rapid overheating of the fuel pin, melt of the cladding and can fail the pressure tube and/or calandria tube within several seconds of accident initiation. Perhaps counterintuitive – quick failure of the PT & CT is desirable. This creates a path for a steam to enter the moderator resulting in a depressurization of the primary heat transport system ensuing in accident detection and scram. Thus, a quicker PT/CT breach will limit the amount of molten material available to interact with the moderator and further failure propagation from the blocked PT to surrounding PTs.

The calculated time scales for the initial portion of this transient (i.e. coolant boiloff and cladding melt) range from 7 to 12 seconds after flow blockage. This range is consistent with that provided in AECL's ACR-700 PIRT [5].

Our analysis shows that molten Zry relocation from structural components to the PT wall is a critical process, but is not well understood. In order to gain a clearer understanding of this process, experimental data must be gathered. It is recommended that at least two separate experiments be completed. The first experiment should verify that molten cladding will in fact flow from horizontal fuel pins under the conditions expected for the blockage event. Cladding flow has been studied previously, but never at the high heat-up rate expected for the blockage event. The second experiment should then study the movement of the molten cladding through the fuel channel to the PT surface. The objective of these experiments would be to see how long it takes after cladding melt before significant amounts of molten Zry contact the PT.

Our thermo-mechanical analyses of the molten Zry/PT and PT/CT interaction established that a minimum molten Zry mass of about 100 g is required for failure of the PT/CT system. This differs considerably from typical analyses and experiments on molten material/PT interaction and PT propagation that assume a large amount (10-25 kg) of molten Zry is available. The analysis completed in this report can assist in future failure

propagation studies by providing time scales than can be used to better estimate the initial molten material inventories.

APPENDIX A: DETAILED DISCUSION OF PHENOMENA LEADING TO CLADDING MELT AND RELOCATION TO THE BOTTOM OF THE PT

A.1. COOLANT BOILOFF

Several assumptions were made in completing this analysis. The reactor remains at full power since flow is not monitored in individual PTs. First, it assumed that the PT is completely blocked at its inlet which forces the incoming coolant flow to immediately cease at time of accident initiation. Secondly, it is assumed that the pressure within the channel remains at the average reactor pressure (12.6 MPa) during boiloff since the PT outlet is open. Lastly, the average coolant temperature is assumed to be 302°C.

The rate of coolant inventory evaporation is easily found using the heat of evaporation, h_{evap}, of water (1321 kJ/kg) and peak channel power, P, of 7.293 MW:

$$\text{Rate of Evaporation} = \frac{P}{h_{evap}} = \frac{7293}{1321} = 5.52 \, {}^{kg}\!/\!_{s} \qquad \text{(A.1)}$$

The total mass of coolant, m_{PT}, (15.33 kg) is calculated by finding the internal volume of the channel (0.02146 m^3) and the density of water (644.7 kg/m^3).

Table VI: Calculated Values for Coolant Boil-Off Analysis

Parameter	Value
Coolant Volume in Single PT (m^3)	0.02146
Coolant Mass in Single PT (kg)	15.33

The evaporation time is then approximately 2.8s as shown in Equation (A.2):

$$t_{evap} = \frac{m_{PT}}{\text{Rate of Evaporation}} = 2.77s \tag{A.2}$$

A.2. PEAK LINEAR HEAT GENERATION RATE

The maximum linear heat generation rate for ACR-700 is proprietary information, thus was approximated through comparison with the CANDU 6 reactor. The known peak heat generation rate in a CANDU 6 reactor is 44.1 kW/m found in Todreas & Kazimi Table 2-3 [4], and the number of pins per channel in CANDU is 37 while the number of pins in ACR-700 is 43. Using this ratio, we can find an approximate peak heat generation rate, q'_{max}, in ACR-700 of 37.9 kW/m:

$$q'_{\max_{ACR-700}} = q'_{\max_{CANDU\,6}} \cdot \frac{\#\,pins_{CANDU}}{\#\,pins_{ACR-700}} = 37.9\,kW/m \tag{A.3}$$

A.3. INITIAL AVERAGE FUEL PIN TEMPERATURE (PRE-ACCIDENT)

The steady-state data before accident initiation are the initial conditions of the transient. In particular, the average fuel pin temperature, fuel centerline temperature and the fuel thermal conductivity are needed to determine the time to cladding melt.

The well-known relationship between the linear heat generation and the temperature profile within the pin is:

$$\int_{T_{fo}}^{T_{\max}} k\,dT = \frac{q'}{4\pi} \tag{A.4}$$

where T_{max}, T_{fo}, and k are the maximum fuel centerline temperature, fuel cladding outer temperature, and thermal conductivity of the fuel, respectively. The fuel cladding outer temperature was estimated to be 372°C by assuming a bulk coolant temperature, T_b, of 328°C and using a series of thermal resistances posed by the cladding and coolant:

$$T_{fo} = T_b + q' \left(\frac{\ln\left(\frac{R_{co}}{R_{ci}}\right)}{2\pi k_c} + \frac{1}{2\pi R_{co} h} \right) \tag{A.5}$$

where R_{co}, R_{ci}, k_c and h are the cladding outer radius, cladding inner radius, conductivity of the cladding, and convection coefficient of the coolant, respectively. The convection coefficient of the coolant was found by using Churchill and Chu's correlation for free convection from a long horizontal cylinder [16].

Inputting into Equation (A.4) into the expression for the variation of the thermal conductivity of the fuel as a function of temperature used by Babcock and Wilcox (Eq. 8-16b[4] in [4]), we find that the average fuel pin temperature and the centerline temperature are 680°C and 1086°C respectively. The linear heat generation rate used for this calculation is the peak heat flux found in Equation (A.3).

Using this same formula, Eq 8-16b, one can then find the average thermal conductivity of UO_2 under these conditions to be 3.64 W/mK.

A.4. FUEL PIN ENERGY REDISTRIBUTION

Upon accident initiation, the coolant surrounding the hottest pin is assumed to immediately vaporize, causing the convection coefficient to become very low and radiative heat transfer to be negligible in the first few seconds of the ensuing heat-up. Therefore, the radial temperature profile flattens quickly. The purpose of the following calculations is to determine how fast the temperature profile (and thus the energy distribution) flattens. If this time is fast compared with the time to cladding melt, then it is acceptable to assume a flat temperature distribution when calculating the time to cladding melt.

The major assumptions used in the energy redistribution calculation are that 1) the thickness of the cladding is small enough that the thermal resistance of the cladding is

[4]Eq. 8-16b from Todreas and Kazimi is reproduced as follows:

$k = \frac{1}{11.8 + 0.0238T} + 8.775 x 10^{-13} T^3$,

where k and T are the UO_2 thermal conductivity, and local UO_2 temperature respectively

extremely low (verified in Section A.5), and 2) the thermal capacity of the cladding is low so as not to effect the redistribution. Also, a physical characteristic of CANDU cladding is that it 'collapses' when the reactor is pressurized, thus the gap resistance is low and is neglected for simplicity. This characteristic coupled with the previous two assumptions support the additional assumption that the temperature of the cladding is approximately equal to the temperature of the fuel (verified in Section A.6).

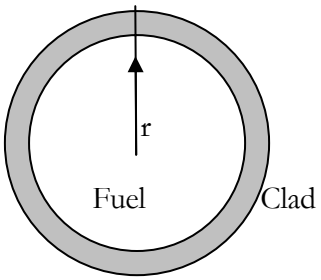

Figure 13: Cladding and Fuel Geometry

The heat diffusion equation describing the fuel pin geometry shown in Figure 13 is defined as:

$$\alpha \frac{1}{r}\frac{\partial}{\partial r}\left(r\frac{\partial T}{\partial r}\right)=\frac{\partial T}{\partial t} \tag{A.6}$$

where α, r, T are the fuel thermal diffusivity, the radial coordinate, and the pin average temperature respectively. The following boundary conditions are applied to this equation:

$$T(r,0)=T_0(r) \tag{A.7}$$

$$-k\frac{\partial T}{\partial r}\Big|_{r=R}=0 \qquad \{\text{for } t \geq 0\} \tag{A.8}$$

where T_o, k, and R are the initial fuel temperature distribution, thermal conductivity of the fuel, and outer radius of the fuel cladding respectively.

Equation (A.6) is solved with the separation of variables method, to obtain the time constant for energy redistribution within the pin:

$$\tau' = \frac{R^2}{\alpha\lambda^2} \tag{A.9}$$

where λ=3.8317 is the dominate eigenvalue of Equation (A.6) for the boundary condition expressed by Equation (A.8).

Using the properties of UO_2 it is possible to obtain a value of this time constant which will give a measure of how quickly the temperature profile will flatten. The thermal diffusivity of UO_2 is given by Todreas & Kazimi [4]:

$$\alpha = \frac{k}{\rho C_p} = 1.39x10^{-6}\ {}^{m^2}\!/_{s} \tag{A.10}$$

where ρ, and C_p are the density of the fuel (95% theoretical), and the heat capacity of the fuel respectively.

Therefore the time constant is approximately 1.4s:

$$\tau = \frac{R^2}{\alpha \cdot \lambda^2} = 1.39s \tag{A.11}$$

This time constant describing the time to energy redistribution, is significantly shorter than the time it takes to melt the pin, thus a single temperature adiabatic heating model is appropriate to describe the pin heat-up.

A.5. VERIFICATION OF LOW THERMAL RESISTANCE OF PIN CLADDING

The thermal resistance of the fuel, R_f, and cladding, R_c, can be calculated as follows:

$$R_f = \frac{1}{8\pi k_f} = 0.011\ {}^{m \cdot K}\!/_{W} \tag{A.12}$$

$$R_c = \frac{\ln\left(\frac{D_{co}}{D_{ci}}\right)}{2\pi k_c} = 3.353x10^{-4}\ {}^{m \cdot K}\!/_{W} \tag{A.13}$$

where D_{co}, D_{ci}, k_c, k_f are the outer diameter of the cladding, inner diameter of the cladding, conductivity of the fuel and conductivity of the cladding respectively. Equations (A.12) and (A.13) indicate that the thermal resistance of the cladding is negligible.

A.6. VERIFICATION THAT PIN CLADDING TEMPERATURE APPROXIMATELY EQUALS FUEL OUTER TEMPERATURE

Using a thermal resistance model and assuming a negligible gap resistance, the temperature difference between the fuel outer temperature and cladding outer temperature can be expressed in terms of the linear power of the pin:

$$T_{fo} - T_{co} = q'\left[\frac{1}{2\pi k_c}\ln\left(\frac{R_{co}}{R_{ci}}\right)\right] = 37.9x10^3\left[\frac{1}{2\pi \cdot 45.7}\ln\left(\frac{.575}{.533}\right)\right] = 10.0^o C \quad \text{(A.14)}$$

where T_{fo}, T_{co}, R_{ci}, and R_{co} are the outer temperature of the fuel, outer temperature of the cladding, inner radius of the cladding and outer radius of the cladding respectively.

Since the temperature difference computed between the outer diameter of the fuel and outer diameter of the cladding is small, the assumption that these values are approximately equal holds.

A.7. CLADDING MELT

The time to cladding melt is calculated using the average fuel temperature (680°C) calculated in Section A.3 as an initial condition. Radiative heat transfer is assumed to have a significant effect on time to melt due to the high temperature differential between the fuel and its surroundings (PT wall, support structure), therefore the governing equation describing the clad heat-up is as follows:

$$\rho C_p \frac{\pi}{4} D^2 \frac{dT}{dt} = q'_f - \pi D \varepsilon \sigma (T^4 - T_\infty^4) \quad \text{(A.15)}$$

The three terms in this equation are energy storage, fission energy production, and radiation heat loss. The values for several of these parameters are given in Table VII..

Table VII: Parameters used in calculating fuel cladding melt

Parameter	Value
Melting temperature of Zr-4 (°C)	1760
Initial average fuel temperature (°C)	680
Heat capacity of UO_2 (J/kgK)	247
Density of UO_2 (95% TD) (kg/m^3)	9186
Emissivity of PT wall	.80
Diameter of fuel pin (mm)	5.75

Non-dimensionalizing this equation results in:

$$\frac{d\theta}{d\tau} = 1 - \theta^4 \tag{A.16}$$

with

$$\theta = \frac{T/T_\infty}{\left[1 + \frac{q'_f}{\pi D T_\infty^4 \varepsilon \sigma}\right]^{1/4}} \tag{A.17}$$

and

$$\tau = \frac{4\varepsilon\sigma T_\infty^3 \left[1 + \frac{q'_f}{\pi D T_\infty^4 \varepsilon \sigma}\right]^{3/4}}{\rho C_p D} t \tag{A.18}$$

Solving Equation (A.16) with the ODE solver MATLAB and substituting the numerical values from Table VIII, one gets the cladding time-to-melt:

$$t_{ZrMelt} = 7.9s \tag{A.19}$$

This model is most likely to represent outer pins that have a high view factor of the PT wall, thus allowing radiation heat transfer to occur. However, inner pins would not lose heat energy via radiation as rapidly since they would mostly 'see' nearby hot pins. Thus, to bound the time to cladding melt, the same analysis has been done without including

radiation heat transfer. The time to cladding melt without including radiation heat transfer is found by setting the radiation term equal to zero in Equation (A.15), integrating and solving for t:

$$t\dot{q} = (C_P m_{UO_2})(T_{melt} - T_0) \tag{A.20}$$

where q, C_p, M_{UO2}, T_{melt}, and T_0 are the power of the fuel, conductivity of the fuel, melting temperature of the fuel, and intitial fuel temperature respectively.

Solving for t:

$$t_{ZrMelt(\text{w/o Rad})} = 4.6s \tag{A.21}$$

Radiative heat transfer is clearly important in this transient since the time to melt including radiation is almost twice as long as the time to melt not including radiation. The actual time to melt is expected to be somewhere in between the two bounding values.

A.8. FUEL MELT

The same process used to find the time to cladding melt can be applied to understand fuel melting, since the heat up is assumed to be even across the fuel and cladding. The melt temperature of the fuel is 2850 °C. Two analysis were completed, one that did not include radiation cooling, and one that included radiation cooling assuming an emissivity of 0.8, typical of oxides. The results are shown in Figure 14. If radiation is not considered, the cladding would be expected to melt within 13.5 s from accident initiation, which then represents the lower bound. If an emissivity of 0.8 is assumed, then no melting is expected to occur as pin heating would come to equilibrium with radiative cooling. This is true as long as the surroundings are not heated significantly. Given enough time, the PT walls would be heated significantly, and radiation cooling would play a lesser role, with melting eventually occurring. It is interesting to note that with these assumptions, even assuming an emissivity of 0.2 would result in long term equilibrium without melt as long as the

surroundings were not heated. It is then reasonable to state that UO_2 melting will occur at the earliest some 14 seconds after accident initiation or at least 7 seconds after clad melt.

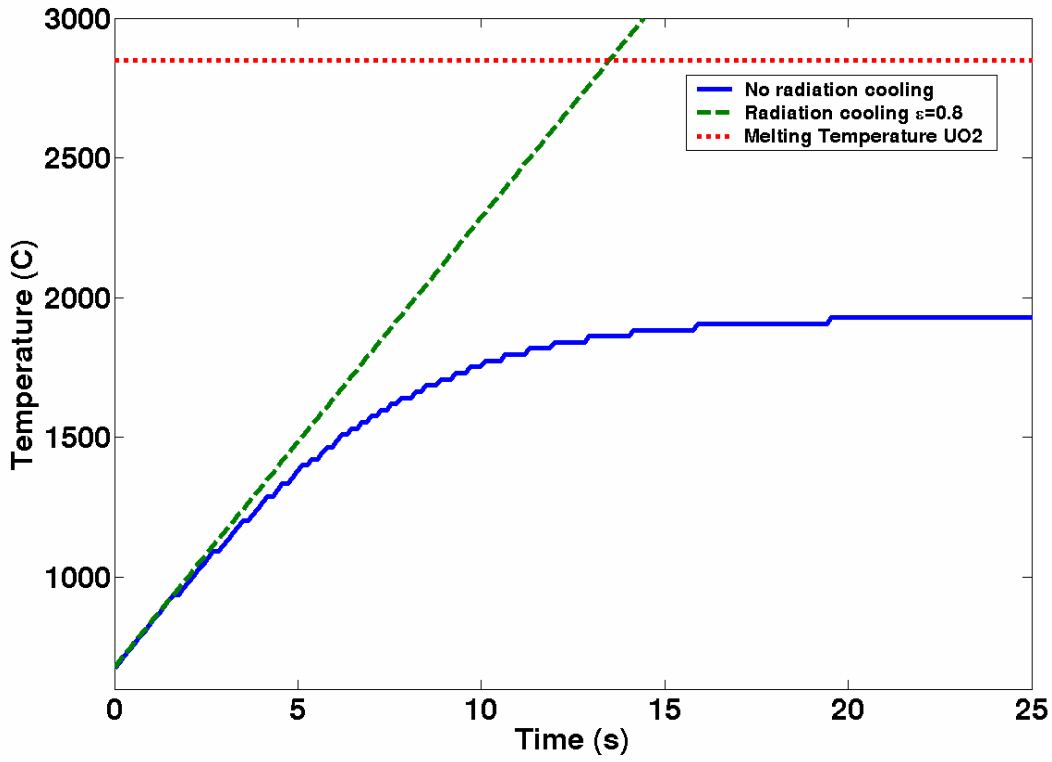

Figure 14: Temperature Histories of Fuel Pin – Melting of UO_2 with and without radiation cooling

A.9. FUEL CLADDING OXIDE LAYER GROWTH DUE TO ZR/STEAM REACTION

The exothermic Zry/steam reaction is shown to increase the oxygen content of the cladding, creating an outer shell of solid UO_2 when interior Zry melts. The equations governing this interaction are given in Section 2.4 as Equations (2.3), (2.4), and (2.5). The heatup time used is the maximum time to clad melt found in Section A.7, which is approximately 8s.

For this calculation, we make the assumption that at the time of transient initiation the cladding has been in the reactor for long enough that a layer of oxide has formed within 10% of the overall thickness of the cladding. If the thickness of the cladding is 0.042cm then the initial thickness of the $ZrO_2 + \alpha$ layer is 0.0042cm.

By separating variables and solving for Equation (2.3) the ZrO_2 + α layer growth we get:

$$\xi_{T_{final},\%O_{init}=10} = \sqrt{2\left(\frac{\delta^2 \cdot \Delta t}{2} + \frac{\xi_{initial}^2}{2}\right)} \tag{A.22}$$

where ξ_{Tfinal}, $\xi_{initial}$, and δ are the finally cladding thickness, initial cladding thickness, and the growth constant (Equations (2.4) and (2.5)) respectively.

Assuming an initial 10% oxygen thickness, then the total oxygen content in the cladding prior to this transient is approximately 6.67%. Using equation (A.22) we find that after 10s the oxide layer thickness has reached 97μm, or 16% of the overall cladding thickness. A time history of the predicted oxide layer growth is shown in Figure 4.

If we assume that there is no initial ZrO_2 formed on the surface of the cladding, or that the cladding was just placed in the reactor, then we can solve for the ZrO_2 + α layer growth:

$$\xi_{T_{final},\%O_{init}=0} = \sqrt{2\left(\frac{\delta^2 \cdot \Delta t}{2}\right)} \tag{A.23}$$

Using Equation (A.23), we find that after 10s the oxide layer thickness has reached 85 μm, or 14% of the cladding thickness. Thus, the initial oxide layer thickness does not contribute heavily to the resulting oxide thickness; however, for the rest of this paper, an initial oxide layer thickness of 10% is assumed to exist on the outer surface of the cladding as a conservative assumption.

In order to place this oxide layer thickness in perspective, it is useful to compare the oxide layer thickness for the single channel flow blockage event to a longer transient such as the large break loss of coolant accident (LB-LOCA) with a failed emergency core coolant system (ECCS). This transient takes place over a longer time-frame (30-100s) since the reactor is assumed to scram at the time of transient initiation, thus the reactor is outputting a comparatively low amount of thermal power. Running the same analysis as above with a 30-100s time period, the cladding is expected to be approximately 45-85% oxidized. Thus,

Zircaloy melt and relocation is expected to be more difficult in the LB-LOCA with ECCS failure than in the complete flow blockage event.

A.10. CONTACT ANGLE BETWEEN ZIRCALOY-4 AND ZIRCONIUM OXIDE

The angle of contact (see Figure 6) is an important parameter governing the interaction between the molten cladding droplet, and the PT wall which are composed of Zircaloy-4 and ZrO_2 [5] respectively.

At present, no direct measurements of the contact angle or wettability of molten Zircaloy-4 cladding with ZrO_2 have been taken. However, some conclusions may be drawn from studies of ZrO_2 interacting with other metals.

The most significant factor governing the geometry of interaction between a liquid metal and a solid ceramic is the surface tension between the liquid metal and vapor surroundings. From the literature [2], the surface tension for pure liquid zirconium is approximately 1500 dynes/cm which lands somewhere between that of Ni and Cu. The literature [6] places the contact angle between ZrO_2-Cu at about 119 degrees for a temperature range of 1473-1773K, and between ZrO_2-Ni at 119 degress for a temperature range of 1740-1953K. For the temperature range discussed, the liquid metals do not wet the ceramic, which is expected of the liquid Zircaloy-4 as well [6,19]. Logically it would make sense that liquid Zr would wet solid Zr well, but the presence of the oxidized ceramic significantly decreases a liquid metal's wettability [2]. The contact angle for the liquid metals does show a small temperature dependence – contact angle decreases with increasing temperature. The temperature range of interest to the molten fuel cladding problem is approximately 2033K, so it is reasonable to approximate the contact angle between ZrO_2/Zry to be approximately 120 degrees.

A.11. MOLTEN DROPLET GEOMETRY

The shape of the molten Zircaloy cladding droplet is governed by the competing effects of surface tension, gravity and hydrostatic pressure as shown in Equation (A.24).

[5] The inner PT wall has a ~1mm thick zirconium oxide layer deposited as a part of the manufacturing process

$$-\rho g\pi r^2 dz + \pi r^2 P_i(z) - \pi\left(r(z+dz)\right)^2 \cdot P_l(z+dz) + P_v$$
$$-2\pi r\sqrt{1+\left(\frac{dr}{dz}\right)^2}\,dz\sin\theta - \gamma 2\pi r\cos\theta \qquad \text{(A.24)}$$
$$+\gamma 2\pi \mathrm{r}(\mathrm{z}+\mathrm{dz})\cdot\cos\left[\theta(\mathrm{z}+\mathrm{dz})\right] = 0$$

where θ, z, z_o, r, ϱ_l, P_l, P_v, represent the contact angle, local droplet height, maximum height, local droplet radius, liquid density, pressure on the inner surface of droplet, pressure on outer surface of droplet respectively. A diagram of this geometry is shown in Figure 15.

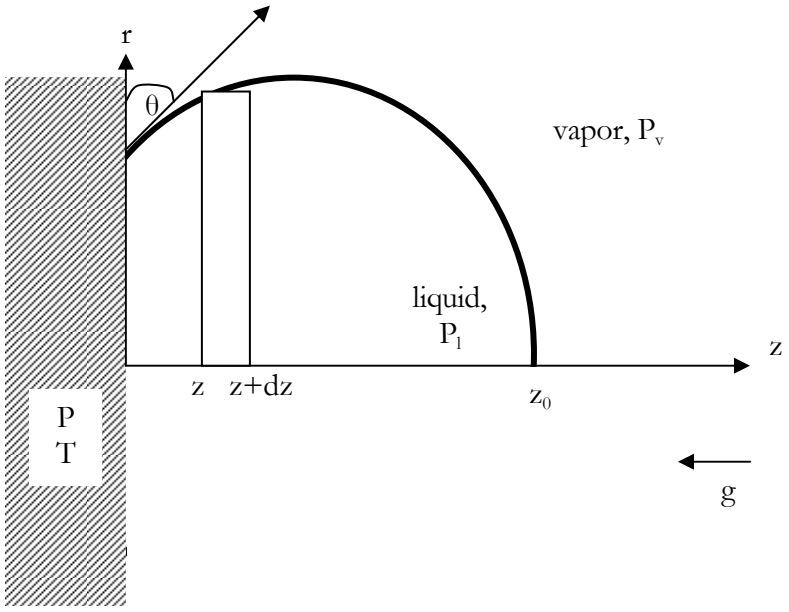

Figure 15: Geometry of Molten Droplet in Contact with PT Wall

The force balance expressed in Equation (A.24) can then be simplified and converted to non-dimensional form as:

$$y\frac{dy}{dx}\left[D^* + \beta(1-x)\right] - \frac{d}{dx}\left[\frac{y}{\sqrt{1+\left(\frac{dy}{dx}\right)^2}}\right] = 0 \qquad \text{(A.25)}$$

with the bounding conditions being:

$$
\begin{aligned}
& y(1) = 0 \\
& \left.\frac{dy}{dx}\right|_{x=0} = \frac{1}{\tan\theta} \\
& \int_0^1 y^2 dx = \frac{M}{\pi\rho_l z_o^{\ 3}}
\end{aligned}
\tag{A.26}
$$

where $\beta=\Delta\rho g z_o^{\ 2}/\Upsilon$, $D^*=\Delta P_o z_o/\Upsilon$, $x=z/z_o$, $y=r/z_o$, $\Delta P_o=P_l-P_v-\Delta\rho g(z_o-z)$ and M represents the mass of droplet. This formulation was implemented using Matlab's ODE solver by rearranging to obtain the following input equations:

$$
\begin{aligned}
\frac{dy_1}{dx} &= y_2 \\
\frac{dy_2}{dx} &= \frac{1+y_2^{\ 2}}{y_1} - (1+y_2^{\ 2})^{3/2}(D^* + \beta(1-x)) \\
y_2(0) &= \cot\theta \\
y_1(0) &= \frac{\dfrac{1}{\sqrt{1+\cot^2\theta}} + \sqrt{\dfrac{1}{1+\cot^2\theta} + \dfrac{M}{\pi\rho_l z_0^{\ 3}}\beta(D^*+\beta)}}{(D^*+\beta)}
\end{aligned}
\tag{A.27}
$$

where $y_1 \equiv y$, and $y_2 \equiv dy/dx$. Upon solving these differential equations, one can obtain the droplet profile, and thus several important parameters relevant to this study: surface area, area of contact between droplet & PT, and droplet height.

Table VIII: Relevant Droplet Parameters from Young-Laplace Model for Molten Zry / PT Contact

Droplet mass (g)	Thickness (mm)	Contact area (mm^2)	Free area (mm^2)
0.1	2.3	7	24
1	4.3	36	110
10	6.8	250	509
100	7.9	2053	2844

A.12. YOUNG-LAPLACE MODEL VERIFICATION

This model was validated experimentally by placing droplets of known volume on various surfaces and measuring the resulting contact angle, droplet height, and contact diameter. The liquids used were water and oil (Shell Omala 2200). The surface tensions used for water and oil were 0.07 and 0.03 N/m respectively [4, 20]. Two types of surfaces were used: stainless steel and a PVC plastic. High resolution pictures of each fluid-surface pair were taken in order to enable measurement of contact angle, droplet height, and contact diameter. Several of these pictures are reproduced below in Figure 16, Figure 17, and Figure 18 . Results of this study are shown in Table IX. These results show relatively good agreement between the model and this coarse experiment with the average deviation between the model and experiment diameters and heights being ±5% and ±20% respectively. This gives us favorable confidence in the validity of the model.

Table IX: Verification of Young-Laplace through comparison of contact parameters of various liquid-surface pairs

								Percentage Difference	
Fluid	Surface	Weight (mg)	Measured Contact Angle	Measured Height (mm)	Measured Contact Diameter (mm)	Calculated height (mm)	Calculated diameter (mm)	Height	Diameter
Water	Plastic	35.0	85.0	2.39	4.64	2.20	5.10	8.14%	9.81%
Water	Plastic	298.0	83.5	3.89	12.36	3.30	12.00	15.27%	2.92%
Water	Plastic	510.0	83.0	4.53	15.90	3.60	15.00	20.49%	5.68%
Water	Metal	36.0	138.0	1.85	8.31	1.20	7.70	35.04%	7.37%
Water	Metal	183.0	134.0	2.79	13.72	1.70	14.20	39.16%	3.53%
Oil	Metal	40.0	124.0	1.47	7.69	1.60	7.50	9.14%	2.50%
Oil	Plastic	71.0	126.0	1.60	9.87	1.40	9.90	12.31%	0.31%
					Average Percent Difference:			**19.94%**	**4.59%**
					Standard Deviation:			**12.47%**	**3.23%**

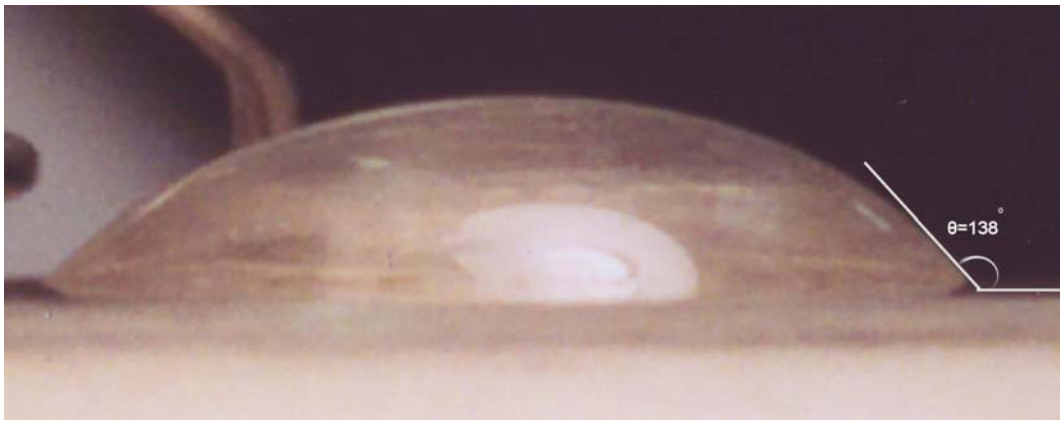

Figure 16: Water/Steel Contact – (36 mg)

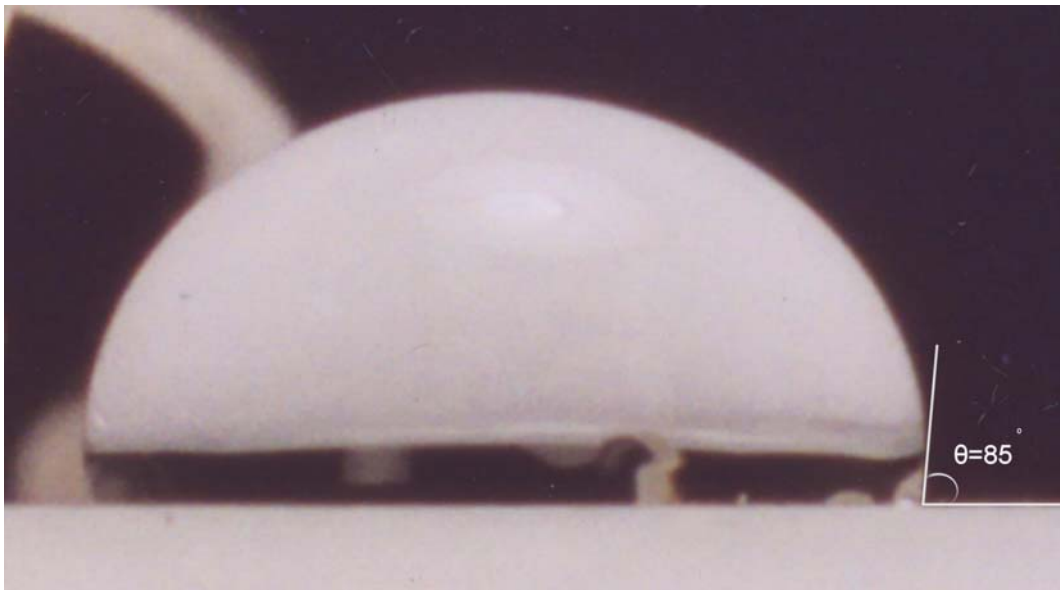

Figure 17: Water/Plastic (PVC) Interaction – (35mg)

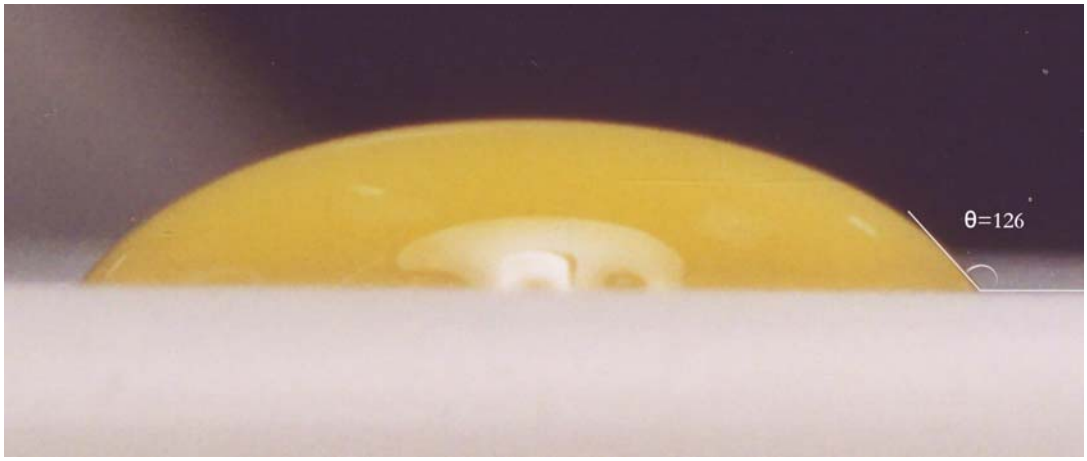

Figure 18: Oil/Plastic (PVC) Interaction – (71mg)

A.13. PT HEATUP DUE TO MOLTEN ZRY CONTACT

The heat-up of the PT wall due to conductive heat transfer via the hot molten Zry was modeled as simple one-dimensional transient heat conduction as shown in Figure 22. The PT wall is assumed to be at 328 °C, which will be approximately the temperature of the stratified coolant that is in contact with the PT prior to molten Zry contact. Once contact is made, the corresponding heat-up of the PT wall is given by:

$$\frac{\partial^2 T}{\partial x^2} = \frac{1}{\alpha}\frac{\partial T}{\partial t} \tag{A.28}$$

with the following boundary conditions:

$$T(x, t=0) = T_o \approx 328^o C \tag{A.29}$$

$$-k\left.\frac{\partial T}{\partial x}\right|_{x=0} = 0 \tag{A.30}$$

$$T_{\text{Zr/PT interface}}(x = y_{PT}, t > 0) = T_w \tag{A.31}$$

where x, and yPT are the distance from the outer PT surface, and the PT thickness (0.648 cm) respectively.

This system of equations can then be solved non-dimensionally and a temperature history for various locations within the PT wall may be obtained (Figure 19).

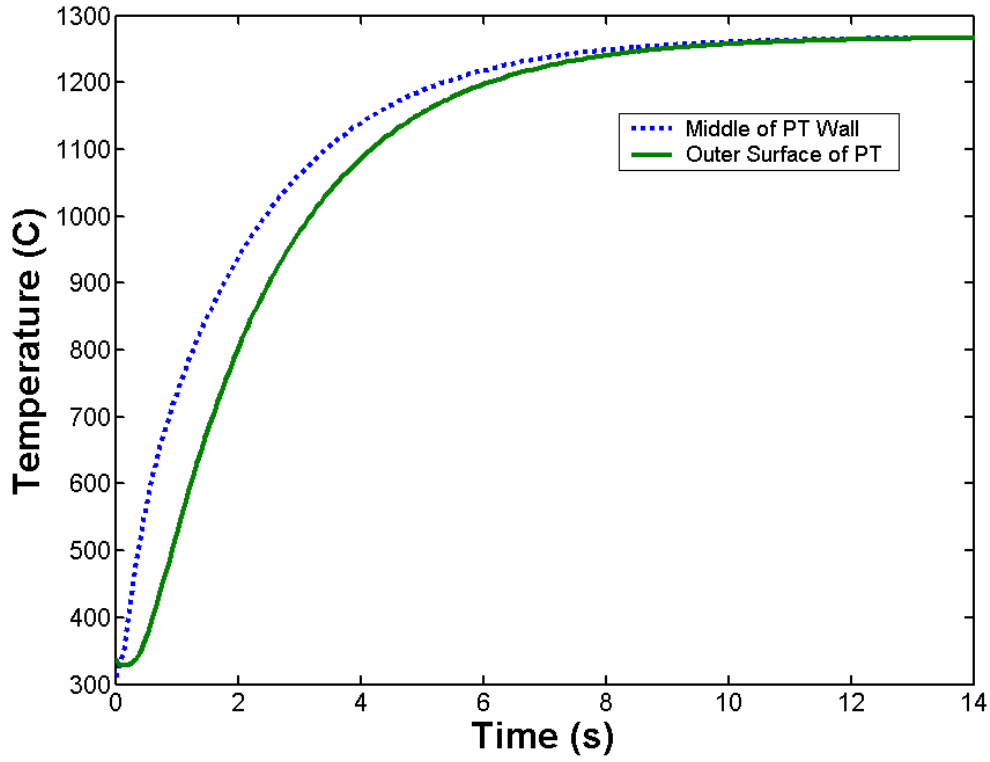

Figure 19: PT Wall 1D Conduction Temperature History

A.14. VERIFICATION OF MATLAB IMPLEMENTATION OF CREEP MODEL

The explicit integration scheme discussed in Equation (A.32) for finding the PT logarithmic strain at any time was implemented via MATLAB 6.5 [21], which is a standard explicit integration scheme:

$$\varepsilon_{i+1} = \varepsilon_i + \dot{\varepsilon}_i \cdot \Delta t \tag{A.32}$$

The output of this model was compared with two cases from Shewfelt et al [17], Figures 8 and 9. These cases from Shewfelt involve extremely fast transient heat-up similar to what is shown to occur when molten Zry is in contact with the PT. Part of the objective of this study was understanding the effect of removing the second terms of both Equations (3.1) and (3.2) which represent hardening terms due to grain-boundary sliding and rapid phase transformation respectively [17]. It is desirable to remove these terms in our study for calculation simplicity and reduced computational load. These terms are shown to be negligible for fast heat-up rates, but to have significant impact for longer transients as can be seen in Figure 20 and Figure 21.

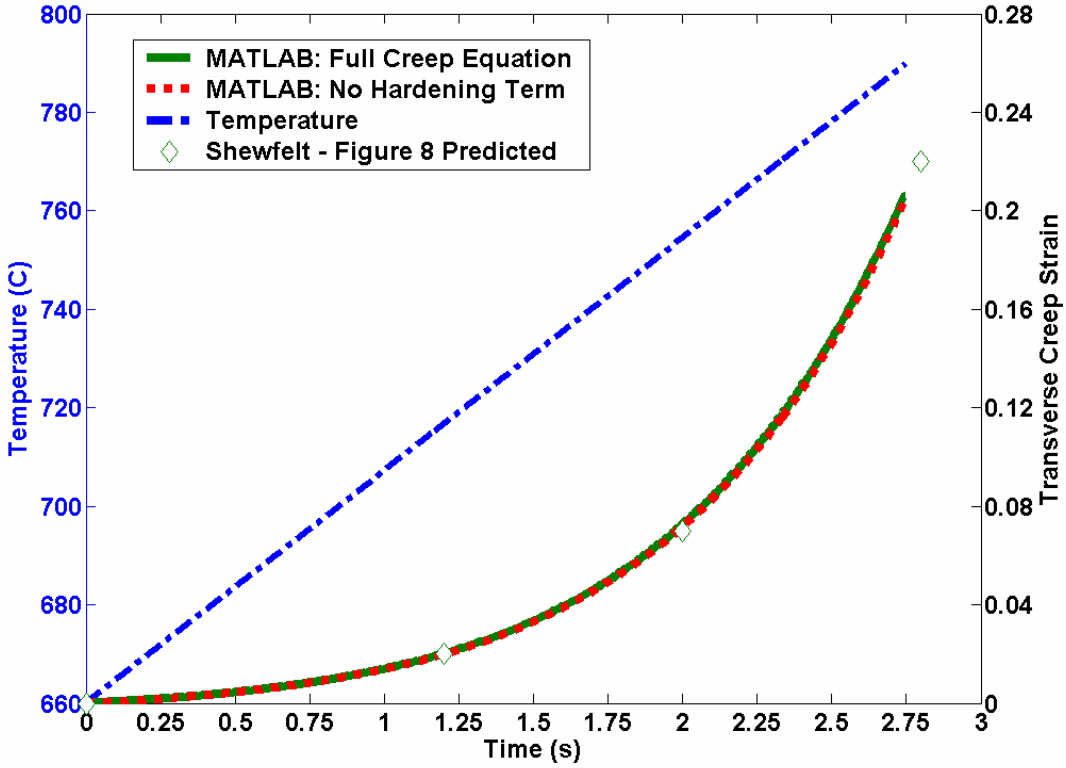

Figure 20: Comparison of MATLAB model with Shewfelt results – Fig. 8

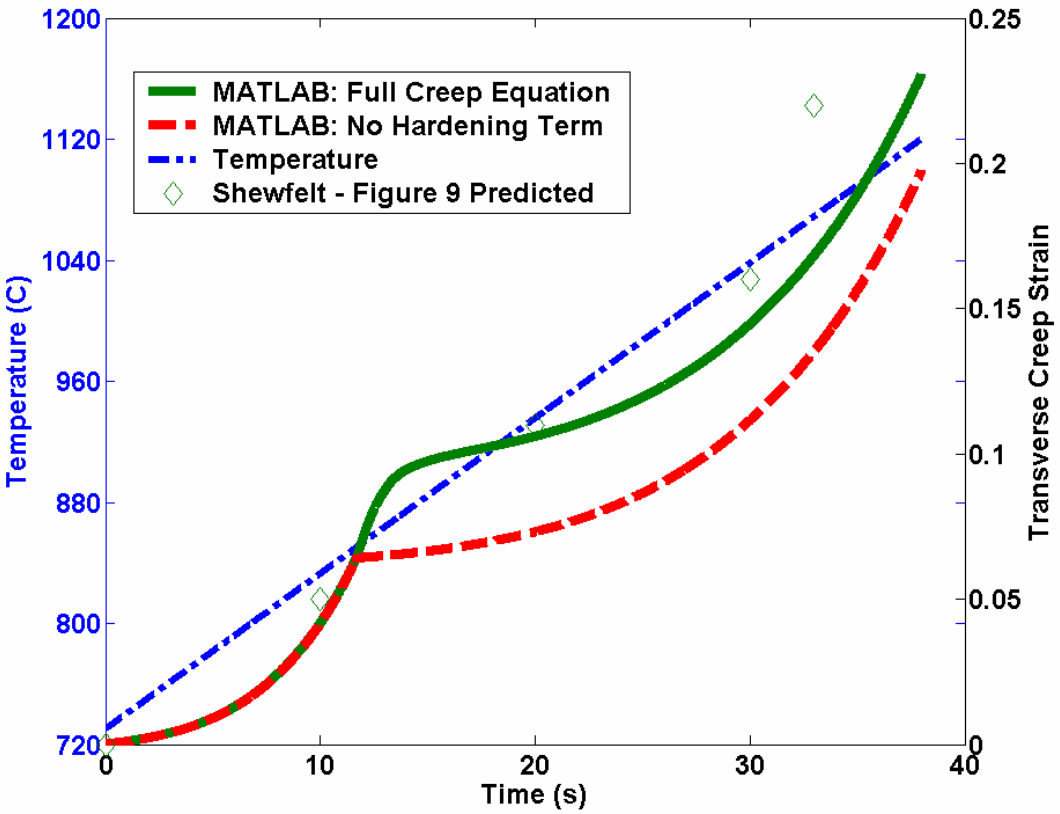

Figure 21: Comparison of MATLAB model with Shewfelt results – Fig. 9

A.15. SENSITIVITY STUDIES FOR SEVERAL PARAMETERS

Sensitivity studies were completed in order to gauge the relative importance of values chosen for several parameters in this study.

Dependence of Time to Cladding Melt on Emissivity of Zircaloy

The duration of heating from time of PT flow blockage to clad melt assuming loss of heat only through radiation is dependent on the emissivity of the ZrO_2 expected to be on the outside of the cladding. A study of this dependence was completed by varying the value of emissivity from 0.0 to 1.0 and using the methods discussed in the preceding discussion to find time to cladding melt.

Table X: Results of Sensitivity of Time to Cladding Melt on Cladding Emissivity

Emissivity of Zircaloy	Difference from nominal emissivity	Time to clad melt (s)	Difference from nominal time to melt
0.00	-100%	4.08	-46.2%
0.20	-75.0%	4.89	-35.5%
0.60	-25.0%	6.55	-23.9%
0.80	--	7.58	--
1.00	+25.0%	10.9	+43.8%

Therefore, a change in emissivity (from .80 the expected value) by a factor of +1.25 results in a change in time to clad melt by a factor of 1.43. A decrease in emissivity by a factor of 1.33 (to 0.60) results in a decrease in time to clad melt by a factor of 1.16, while a decrease in emissivity of 4 to 0.20 results in a decrease in time to clad melt by a factor of 1.4.

Thus, in the immediate vicinity of the expected emissivity of 0.80 there seems to be some relatively large change in time to melt, but as emissivity decreases there is less change in time to melt. However, the certainty in the emissivity value is quite high since it is highly expected that the outer surface of the cladding will remain completely covered in an oxide layer, where the emissivity is known to be approximately 0.80.

Dependence of Time to Cladding Melt on Linear Heat Rate

The duration of heating from time of PT flow blockage to clad melt assuming loss of heat only through radiation is dependent on the linear heat generation rate, q', of the fuel. For this report, as discussed in Section A.2, a linear heat generation rate of 37.9 kW/m has been considered via comparison of the ACR-700 and CANDU-6 designs. Since this value is not certain, a sensitivity study was completed. This model starts by using the various linear heat generation rates to find a fuel outer temperature, and average fuel conductivity coefficient. Then the time constant is found using the methods of Section A.7. The results of this study are reported in Table XI.

Table XI: Results of Sensitivity Study of q' on Time to Clad Melt

Linear heat generation rate (kW/m)	Difference from nominal linear heat rate	Initial fuel outer temperature (C)	Conductivity of fuel (W/mK)	Time to melt (s)	Difference from nominal time to melt
34.1	-10%	367	3.81	10.0	+2.67%
37.9	--	372	3.64	9.74	--
41.7	+10%	376	3.48	9.34	-4.11%
56.9	+50%	393	2.98	7.31	-25.0%

So increasing the linear heat rate from 37.9 to 41.7 kW/m, or by a factor of 1.1 the time to melt decreased by 1.04 seconds, and increasing the heat rate by a factor of 1.5 resulted in a decrease in the time to melt by a factor of 1.33. Therefore, the time to cladding melt is not heavily dependent on the linear heat generation rate, but is still effected, especially at high heat rate.

This analysis also shows how time to cladding melt is dependent on the thermal conductivity of the fuel, whose value is heavily coupled with the initial fuel outer temperature. From the above analysis a decrease in the conductivity of the fuel by a factor of 1.2 led to a decrease in time to clad melt of 1.33. However, the value of the conductivity of the fuel is accurately known by using the semi-empirical formulas used by fuel manufacturers [4, pp 301].

APPENDIX B: DETAILED DISCUSSION OF ZRY/PT AND CT MODELS

B.1. VERIFICATION OF COSMOSM HEAT TRANSFER MODEL

A simple one dimensional model was created in COSMOSM in order to benchmark the program's modeling capabilities with an analytical model for the 1D heat-up of the PT wall underneath the droplet as shown in Figure 22, where the inner surface of the PT wall is being heated via contact with the molten Zircaloy, while heat transfer at the outer surface of the PT is assumed negligible. The latter assumption is accurate if the PT has not yet ballooned into contact with the calandria tube. The PT/CT contact situation is discussed in detail in the 3-D analysis of Section 3.1.

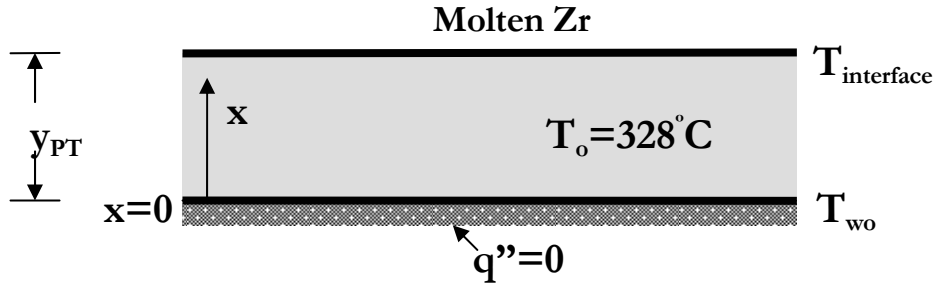

Figure 22: Diagram of 1-D Transient Conduction in PT Wall

The transient conduction problem can be solved and the temperature profile over time for various locations along the thickness of the PT may be obtained. The temperature history for the middle of the PT is shown in Figure 23.

As in the theoretical model, the contact temperature is assumed to remain at 1268 °C, the outer wall is considered adiabatic, and physical data is included in Table XII.

Table XII: Physical Properties for Molten Cladding and PT

Parameter	Value	Source
Molten Cladding Density (kg/m^3)	6550	[4]
PT Wall Density (kg/m^3)	6500	[4]
Molten Cladding Conductivity (W/mK)	50	[25]
PT Wall Conductivity (W/mK)	16	[22]
Molten Cladding Heat Capacity (kJ/kgK)	356	[25]
PT Wall Heat Capacity (kJ/kgK)	307	[22]

The GeoStar model was created using a simple PLANE2D element configuration with a 100 x 100 meshing and a time increment of 0.04 seconds.

The temperature of the middle node of the model is shown in Figure 23 and compares extremely well with the theoretical temperature vs. time.

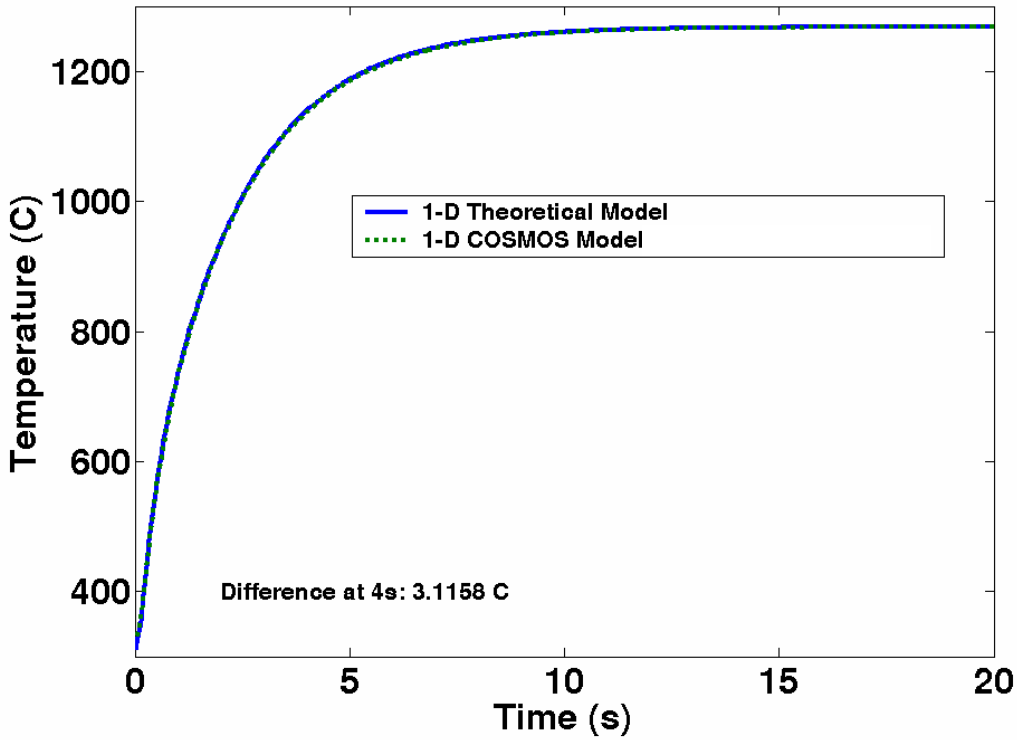

Figure 23: Comparison of 1-D Theoretical and COSMOSM Mid-Plane PT Temperature Histories

B.2. COSMOSM HEAT OF FUSION MODEL FOR ZRY SOLIDIFICATION

The phase change during the solidification of the molten Zircaloy is simulated in COSMOSM by incorporating the latent heat of fusion (224 kJ/kg) into the model for the specific heat of Zircaloy. The method chosen for this model is introducing a spike at the melting point of Zircaloy in a C_p vs. Temperature curve within COSMOSM. As shown in Figure 24, there is a spike in the C_p in narrow range between 2032.8 K and 2033 K of 2.24×10^6 J/kg. The area under this spike equals 224 kJ/kg, thus properly accounting for the heat of fusion around the melting temperature of Zry (2033K). For all other temperatures, the specific heat is kept at a constant 356 J/kg.

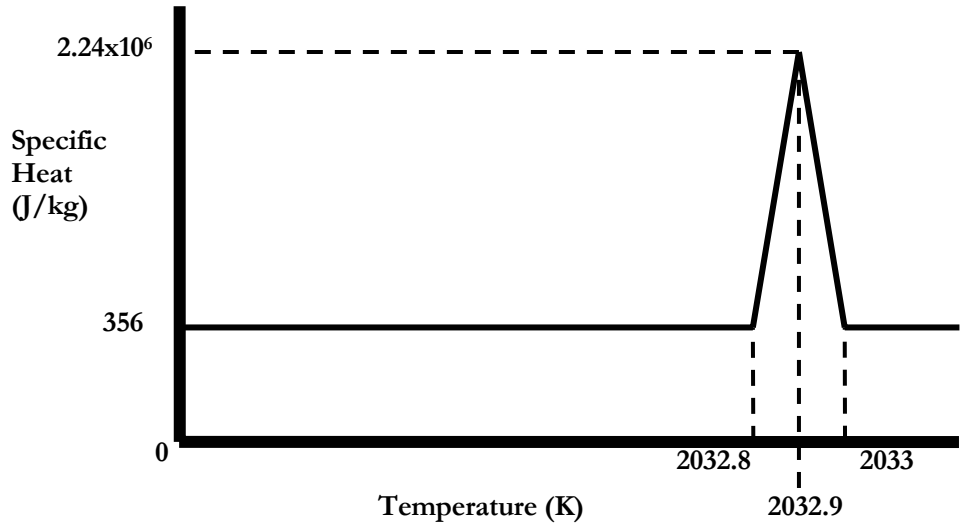

Figure 24: Specific Heat with 0.2-degree width Spike Representing Heat of Fusion Model

Theoretical Model for Droplet Solidification

To ensure that the COSMOSM model is appropriate, it was compared with the theoretical model for droplet solidification as described below, with the solidification time modeled as Equation (B.3).

To determine the time needed for full solidification of the droplet, a simple one dimensional model characterizing the energy balance at the freezing front was developed as shown in shown in Figure 3.

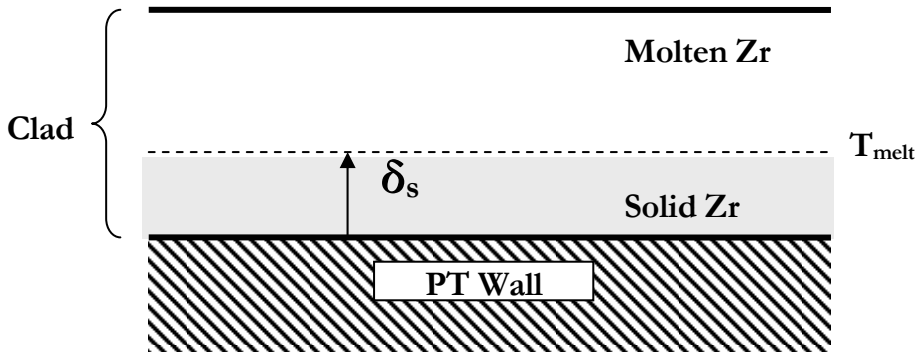

Figure 25: One Dimensional Freezing Front Model

The heat flux through the solid front is given by:

$$q'' = \frac{k_s}{\delta_s}(T_{melt} - T_w) \tag{B.1}$$

where q", k_s, δ_s, T_{melt}, and T_w are the heat flux at the freezing front, thermal conductivity of the solid Zircaloy, thickness of the solid front, melting temperature of Zircaloy, and the PT wall temperature respectively.

Thus, the energy balance at the solidification front is:

$$\rho_s h_{ls} d\delta_s = \frac{k_s}{\delta_s}(T_{melt} - T_w)dt \tag{B.2}$$

The heat of fusion of Zircaloy, h_{ls}, is 224 kJ/kg [8], its thermal conductivity, k_s, is 50 W/mK, and its density, ϱ_s, is 6500 kg/m^3. Equation (B.2) can be integrated to solve for the time required to solidify the entire thickness of the droplet:

$$t_{solidify} = \frac{\delta_s^{\,2}\rho_s h_{ls}}{2k_s(T_{melt} - T_w)} \tag{B.3}$$

This model is considered a reasonable approximation as long as:

$$C_{ps}(T_{melt} - T_w) << h_{ls} \quad \text{(B.4)}$$

where C_{ps} is the heat capacity of the solid Zry, given as 356 J/kgK [4]. The value of the left hand side of Equation (B.4) is 178 kJ/kg which is somewhat less than the value of h_{ls}, so we can say the model is at least reasonable.

Several representative times for complete solidification predicted by this 1-D analytical model are given in Table XIII. Note that even relatively large droplets release most of their energy within less than 2 s.

Table XIII: Time to Complete Solidification for Representative Droplets

Droplet weight (g)	Thickness of droplet (mm)	Time to solidify (s)
0.1	2.3	0.157
1	4.3	0.547
10	6.8	1.369
100	7.9	1.847

COSMOSM Solidification Model

The COSMOSM model used for this simulation is a one dimensional and meshed similar to the model discussed in Section B.1.

For the comparison, a contact temperature much higher than will actually be encountered was chosen (2000K) simply because the theoretical model is only acceptable for small differences between the saturation temperature and the PT wall contact temperature. This temperature is also sufficiently far from the specific heat spike so that the arbitrary selection of the spike width will not affect the solution. As long as the COSMOSM model accurately mirrors this theoretical model for these artificial boundary conditions, we can then assume the COSMOSM model will work under the actual boundary conditions – since the COSMOSM model is not reliant on the simplifications made in the theoretical model. In this model, and for all thermal models discussed in this paper, the molten Zry initial temperature is set to 1762°C to allow sufficient margin for this heat of fusion model to work correctly.

As can be seen in Figure 26, the COSMOSM model does closely follow the theoretical model. However, it does seem to overestimate the time to solidification especially for larger thicknesses. This is likely due to the assumptions used in the theoretical model. The COSMOSM model will account for subcooling in the region nearest the PT wall, unlike the theoretical model.

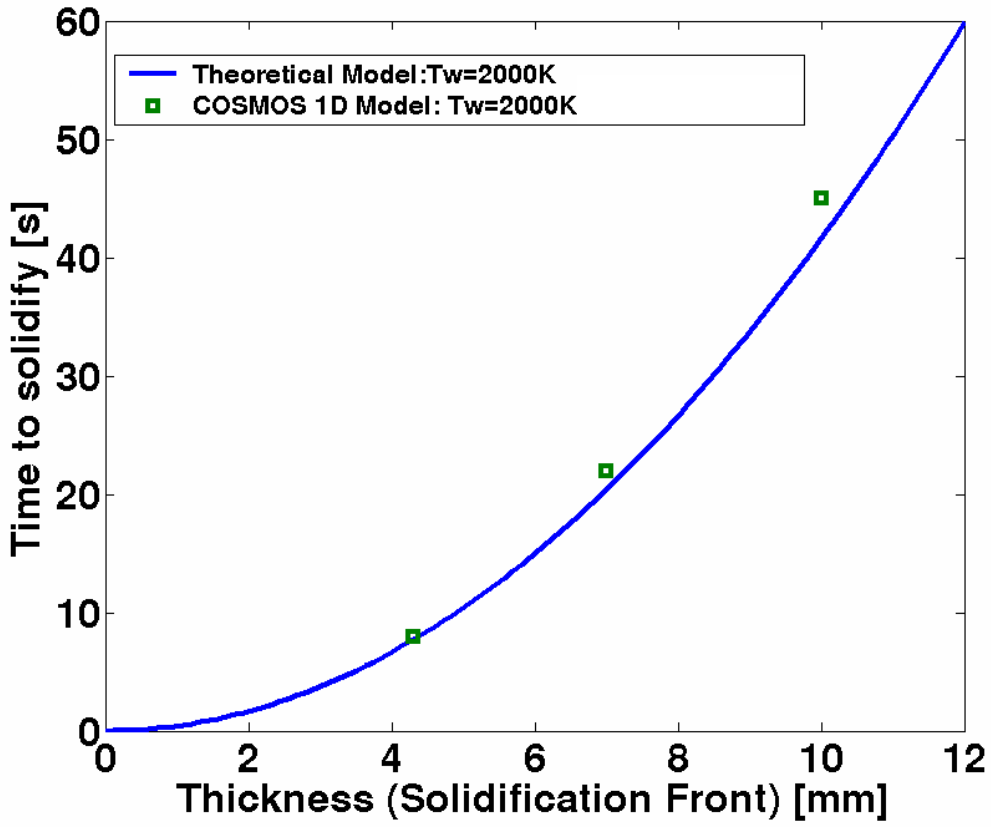

Figure 26: Comparison of Theory and COSMOSM Prediction of Time to Molten Zry Solidification of Various Droplet Thicknesses

B.3. INCLUSION OF ZRY/STEAM REACTION

The approximate heat flux through the surface of the molten mass produced by the Zircaloy steam oxidation reaction is given by:

$$q'' = \frac{E_{chemical}}{t_{solidify} \cdot A_s} \tag{B.5}$$

where q", $E_{chemical}$, $t_{solidify}$, and A_s are heat flux through the free surface of the drop, the energy released via this reaction, the solidification time and the free surface area reported in Table VIII respectively. The value used for solidification time (~2.0s for a 10g droplet) was estimated using a characteristic COSMOS thermal model. The energy released via the chemical reaction (~50 J for a 10g droplet) was found as follows:

The description of this reaction is given as Equation (2.2). The parabolic reaction rate constant for the Zry/Steam reaction is given by the following temperature relation [2]:

$$K_p = 8.79x10^5 e^{-16610/T_{Zr}} \quad {mg^2}/{cm^4 s} \tag{B.6}$$

Using the definition of the 'extent' of the reaction, ω, given as [2]:

$$\omega^2 = K_p t \tag{B.7}$$

we can approximate the total energy output during the time it takes for the Zry to solidify as:

$$E_{in} = \left(\Delta H_{RX}\right) \cdot \left(\sqrt{K_p \cdot \Delta t}\right) \cdot \left(\frac{mol_{Zr}}{\mathrm{A}_{Zr}}\right) \cdot A_s \tag{B.8}$$

with ΔH_{RX} equaling 587 kJ/mol_{Zr}, and A_{Zr} being the atomic weight of Zircaloy, 91.2g/mol.

For the 10g droplet, a flux of 476 kW/m^2 was obtained.

B.4. INCLUSION OF RADIATION & CONVECTION WITHIN GAS ANNULUS

Radiation and convection heat transfer within the gas annulus that separates the PT & CT may be a significant source of cooling. To determine the magnitude of this cooling, two three dimensional models were created: 1) one including radiation and convection and 2) one assuming an adiabatic boundary condition on the PT outer surface. The typical 100g molten Zry model geometry discussed in Section B.1 was used, with applied convection and radiation boundary conditions as discussed below.

Convection Heat Transfer Coefficient

The convection heat transfer coefficient for the outer surface of the PT was found using the correlation produced by Rohsenow and Hartnett [16] for concentric tube annuluses. The flow rate within the gas annulus for a CANDU type reactor is 3.0 L/s [24]. Thermodynamic data for CO_2 was found in [16] for a temperature of 201 °C which is chosen as the average of the initial PT wall surface temperature (328 °C) and the approximate CT surface temperature (74°C). Physical data for this problem is given in Table XIV.

Table XIV: Physical Data Used in Calculating Convection Coefficient of Gas Annulus

Parameter	Value
PT Outer Radius (cm)	5.8169
CT Inner Radius (cm)	7.55
Flow Area (m^2)	7.28×10^{-3}
Velocity of Gas (m/s)	0.412
Density of CO_2 (m^3/kg)	1.12
Viscosity of CO_2 (Ns/m^2)	221×10^{-7}
Conductivity of CO_2 (W/mK)	30.4×10^{-3}

The hydraulic diameter, D_h, of the annulus is found as:

$$D_h = D_o - D_i = 3.466cm \tag{B.9}$$

with D_o and D_i being the diameters of the inner surface of the CT and the outer surface of the PT respectively. The Reynolds number of the gas is then:

$$\mathrm{Re} = \frac{\rho v D_h}{\mu} = 723 \tag{B.10}$$

with ρ, v, and μ being the density of CO_2, gas velocity and viscosity of CO_2 respectively. The Nusselt number is then estimated by using Equation 8.73 and Table 8.3 from [16]. A

value of 9.6 was found. This corresponds to a convective heat transfer coefficient of approximately 10.0 W/m^2.

Radiation Heat Transfer

The surrounding temperature for the radiation heat transfer portion of the annulus boundary condition was set to 177 °C as discussed above. The emissivity of the outer surface of the PT was set as 0.7 in order to model an oxidized surface.

A comparison of the COSMOSM temperature history output between the base case with an adiabatic PT outer surface boundary condition and a radiation & convection heat transfer boundary condition as discussed above is shown in Figure 27. These results show that there is a difference between the two boundary conditions, thus a radiation and convection boundary condition is used for all the studies in this paper unless otherwise stated.

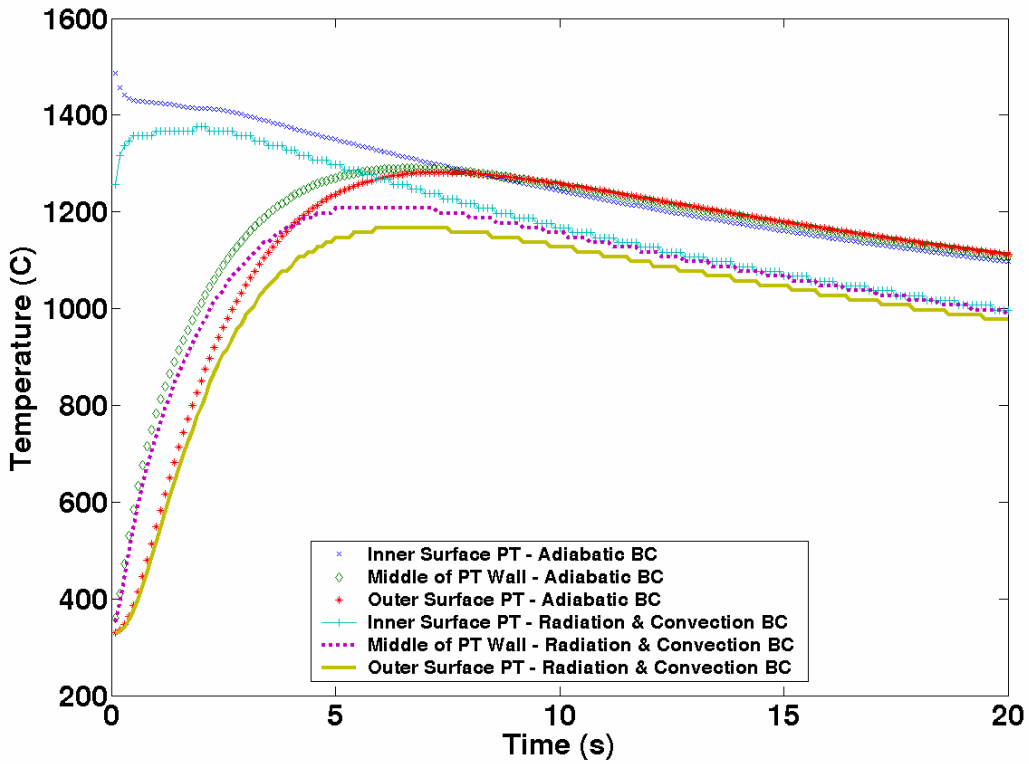

Figure 27: Comparison of PT Temperature Histories with an Adiabatic BC or a Radiation/Convection BC on Outer PT Surface

B.5. CONTACT RESISTANCE BETWEEN MOLTEN ZRY & PT DUE TO ZrO_2 LAYER

The thermal conductivity of ZrO_2 is much lower than that of pure Zr, and thus effectively acts as an insulator. It is expected that a thin layer of ZrO_2 will exist on the outer surface of the PT which will impede heat transfer between the molten Zry and PT wall. In fact, a ~0.2 mm ZrO_2 layer is deposited on the inner surface of the PT during manufacturing process. Thus, it is appropriate to study the impact of this thermal resistance on the heat-up of the PT wall.

The thermal conductivity, k, of ZrO_2 is 2.0 W/m^2K [25]. The contact resistance, R, of the ZrO_2 layer is defined as:

$$R = \frac{d}{k} \tag{B.11}$$

where d is the oxide layer thickness. Reference thicknesses of 20μm, 200μm and 2.0mm where chosen which correspond to resistances of 0.00001, 0.0001 and 0.001 m^2K/W respectively. Thermal simulations in COSMOSM were completed by inputting the above values as thermal resistances for the surface contact pair between the molten Zry and PT inner wall. All runs used the same model for the 100g geometry as discussed in previous sections. Figure 28 through Figure 30 show a comparison of the temperature histories of five cases at various locations in the PT wall. The first case is merely the base 100g case with an adiabatic boundary condition on the outer PT wall. The second through fourth cases are modifications of this base case using the three different oxide thicknesses. The fifth case modifies the 200μm model to include radiation and convection on the outer surface of the PT wall. From this analysis, it is clear that for oxide thicknesses of less than 20μm, the temperature history is unaltered, while for oxide thicknesses of >200μm the temperature history is reduced and greatly delayed. The impact of the oxide layer on time to failure is studied in the structural portion of this report (Section B.11).

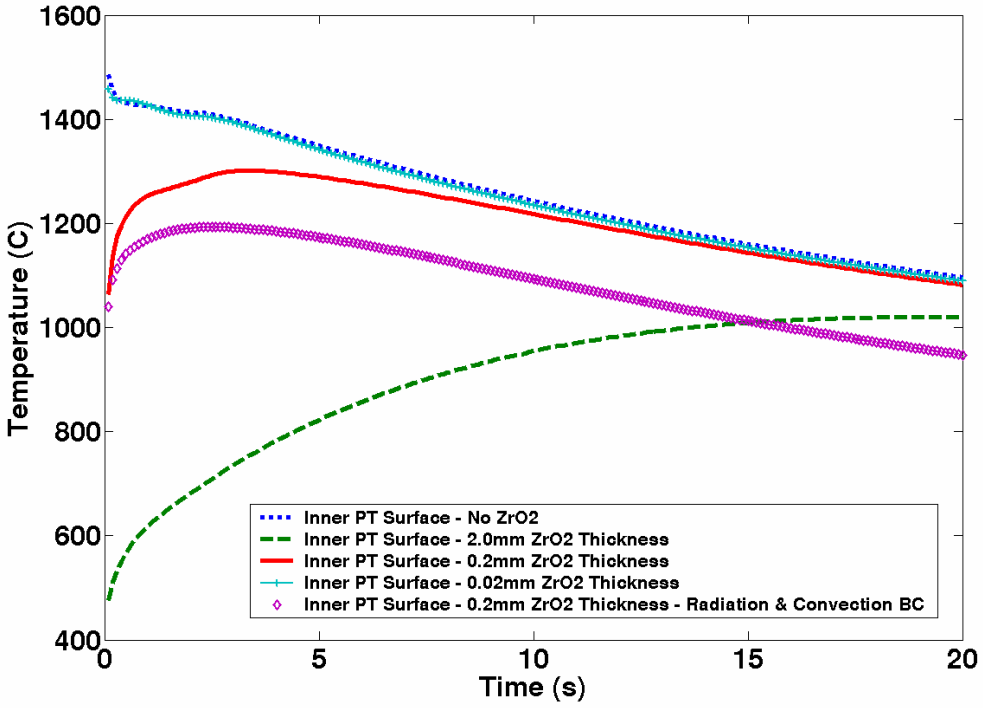

Figure 28: Thermal Contact Resistance Analysis: Inner PT Surface Comparison

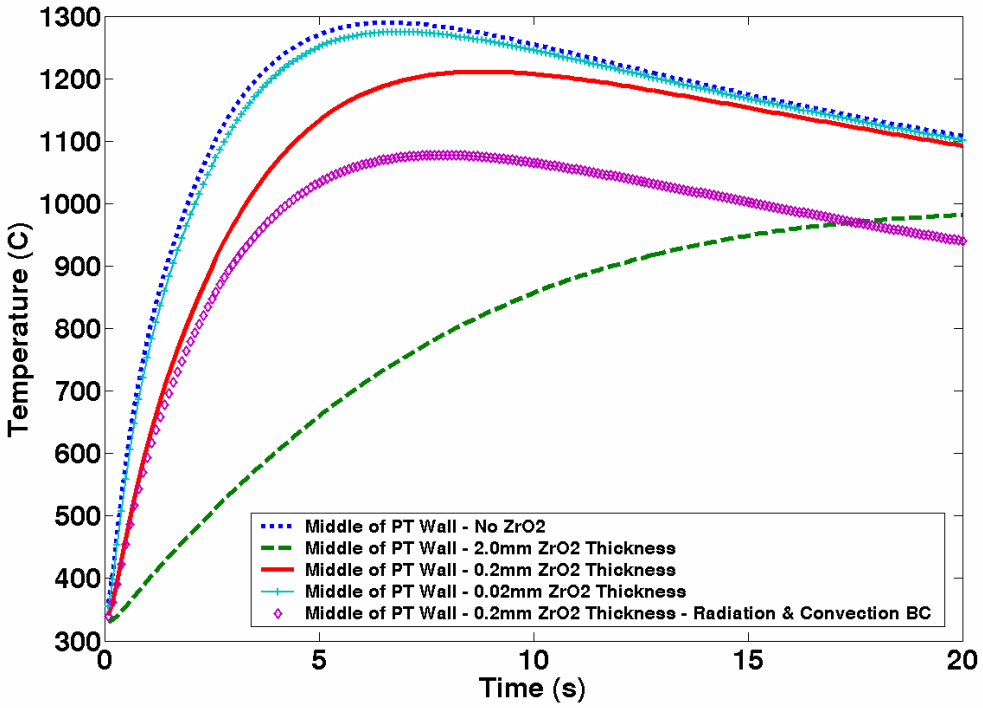

Figure 29: Thermal Contact Resistance Analysis: Middle PT Wall Comparison

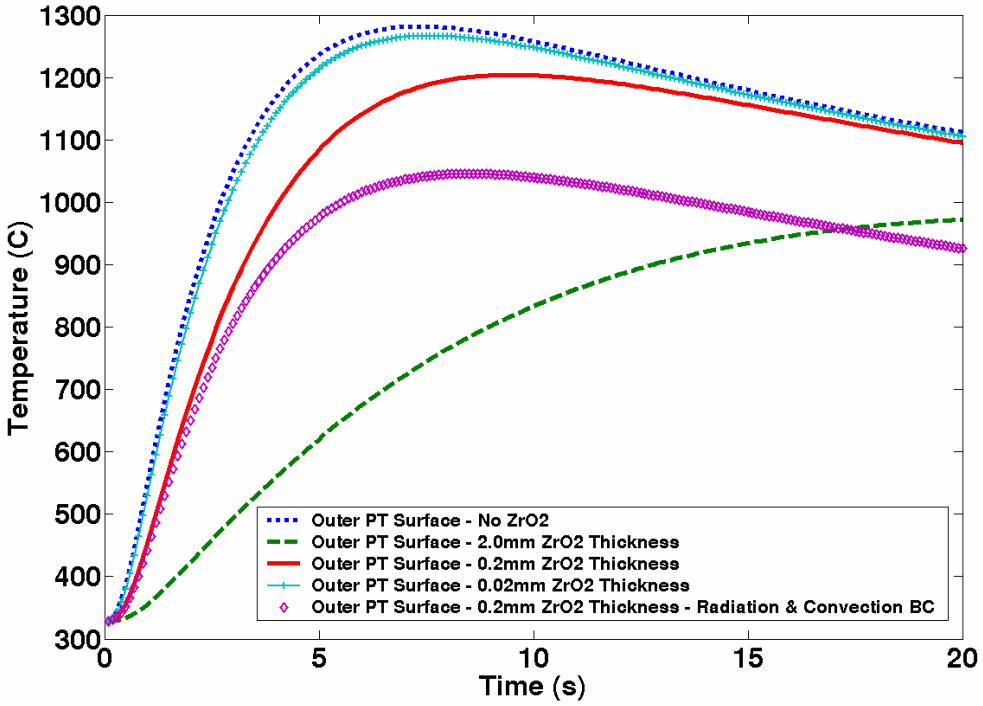

Figure 30: Thermal Contact Resistance Analysis: Outer PT Surface Comparison

B.6. PRESSURE TUBE CREEP STRAIN ANALYSIS

A three dimensional model was developed to study the bulging of the PT wall due to the presence of the localized hotspot from the molten cladding droplet. This model has been developed analytically, and implemented via MATLAB (see Appendix C for source code). The area beneath the molten Zry is expected to bulge in a spherical fashion (Figure 31) as it heats and significant creep strains are produced. The membrane stresses within the shell are given as:

$$\sigma_r = \frac{P}{2} \tag{B.12}$$

$$\sigma_t = \frac{1}{\left(1+\frac{\delta}{r}\right)^2 - 1} P \tag{B.13}$$

where σ_r, σ_t, P, r and δ are the radial stress, tangential (hoop) stress, PT pressure, inner instantaneous radius of curvature for the bulging area, and the thickness of the wall in the

bulging area. The equivalent or Von-Mises stress is calculated in the usual way first defining the stress tensor as:

$$\underline{\underline{\sigma}} = \begin{vmatrix} \sigma_{11} & \sigma_{12} & \sigma_{13} \\ \sigma_{12} & \sigma_{22} & \sigma_{23} \\ \sigma_{13} & \sigma_{23} & \sigma_{33} \end{vmatrix} = \begin{vmatrix} \sigma_r & 0 & 0 \\ 0 & \sigma_t & 0 \\ 0 & 0 & \sigma_t \end{vmatrix} \tag{B.14}$$

where σ_{11}, σ_{22}, σ_{33} are the three principal stresses. Then finding the deviatoric stress tensor, S, as:

$$\begin{aligned} \underline{\underline{S}} &= \begin{vmatrix} \frac{2}{3}\sigma_{11} - \frac{1}{3}\sigma_{22} - \frac{1}{3}\sigma_{33} & \sigma_{12} & \sigma_{13} \\ \sigma_{12} & \frac{2}{3}\sigma_{22} - \frac{1}{3}\sigma_{11} - \frac{1}{3}\sigma_{33} & \sigma_{23} \\ \sigma_{13} & & \frac{2}{3}\sigma_{33} - \frac{1}{3}\sigma_{11} - \frac{1}{3}\sigma_{22} \end{vmatrix} \\ &= \begin{vmatrix} \frac{2}{3}\sigma_r - \frac{2}{3}\sigma_t & 0 & 0 \\ 0 & \frac{1}{3}\sigma_t - \frac{1}{3}\sigma_r & 0 \\ 0 & 0 & \frac{1}{3}\sigma_t - \frac{1}{3}\sigma_r \end{vmatrix} = \frac{1}{3}\left(\sigma_t - \sigma_r\right)\begin{vmatrix} -2 & 0 & 0 \\ 0 & 1 & 0 \\ 0 & 0 & 1 \end{vmatrix} \end{aligned} \tag{B.15}$$

The equivalent stress, σ_e, is given by the Von-Mises relation:

$$\sigma_e = \sqrt{\frac{3}{2} S_{ij} S_{ij}} = \sqrt{2}\left(\sigma_t - \sigma_r\right) \tag{B.16}$$

The associated flow rule is then applied to find the strain rate tensor, $\dot{\varepsilon}_{ij}$, as:

$$\dot{\varepsilon}_{ij} = \frac{3}{2}\frac{S_{ij}}{\sigma_e}\dot{\varepsilon}_e \tag{B.17}$$

where $\dot{\varepsilon}_e$ is the one dimensional logarithmic creep strain rate given in Equations (3.1) and (3.2). From the relation in Equation (B.17), the radial creep strain rate, $\dot{\varepsilon}_r$, and tangential creep strain rate, $\dot{\varepsilon}_t$, are found as:

$$\dot{\varepsilon}_r = -\frac{1}{\sqrt{2}}\dot{\varepsilon}_e \tag{B.18}$$

$$\dot{\varepsilon}_t = \frac{1}{2\sqrt{2}}\dot{\varepsilon}_e \tag{B.19}$$

Using an explicit integration scheme, the tangential strain at any time is given by:

$$\varepsilon_t(t+\Delta t) = \varepsilon_t(t) + \varepsilon_t \Delta t \tag{B.20}$$

The logarithmic tangential strain can also be defined as the logarithm of the fractional change in arc length:

$$\varepsilon_t = \ln\left(\frac{2r\theta}{2r_0\theta_0}\right) = \ln\left(\frac{r\theta}{r_0\theta_0}\right) \tag{B.21}$$

where θ, θ_0, and r_0 are the angle between the line of symmetry and the outer rim of the bulging area (see Figure 31), the initial angle, and the initial radius of curvature respectively. Using Figure 31, the following geometrical relations can be found for the angle and the radius of curvature:

$$\sin\theta = \frac{x}{r} \tag{B.22}$$

$$\sin\theta_0 = \frac{x}{r_0} \tag{B.23}$$

where x is the distance perpendicular to the line of symmetry in the bulge to the outer rim of the bulging area. These expressions naturally lead to the following relation:

$$\frac{r}{r_0} = \frac{\sin\theta_0}{\sin\theta} \tag{B.24}$$

which can be used to solve for the angle using Equation (B.21):

$$\frac{\sin\theta}{\theta} = \frac{\sin\theta_0}{\theta_0}\frac{1}{e^{\varepsilon_t}} \tag{B.25}$$

This equation can be iterated to obtain a numerical value for θ. Then, Equation (B.24) can be used to solve for the new value of radius of curvature. The volume within the bulging area is given by:

$$V = \left[\frac{4}{3}\pi(r+\delta)^3 - \frac{4}{3}\pi r^3\right]\frac{\Omega}{4\pi} \tag{B.26}$$

where Ω is the solid angle subtended by the bulging area which is given by:

$$\Omega = 2\pi(1-\cos\theta) \tag{B.27}$$

It is well known that creep strains occur with negligible volume change, thus volume conservation within the bulging area is used to find the new thickness. These new values for thickness, radius of curvature, and theta are then input into Equations (B.12) and (B.13) repeating the process to calculate the next time step. In this way, the growth history of the bulging area can be predicted until the theoretical failure point has been reached which has been predetermined to be a 37% reduction in wall thickness [18].

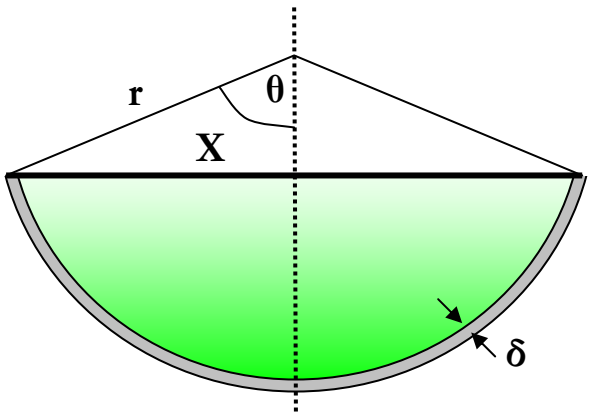

Figure 31: Spherical Bulge beneath Molten Zry

B.7. BULGE GROWTH

Upon coming in contact with the PT, the molten Zry will heat up the PT region directly beneath. However, as time progresses, the heated region of the PT will increase as the heat diffuses both axially and circumferentially. Thus, choosing a constant radius for the bulging area, x, as was done in the model discussed in Section B.6, is not quite accurate. From simplified 1-D heat-up models, we found that when the PT is subjected a temperature of approximately 800°C, creep strains become large and the material is very compliant. Thus, to accurately describe the size of the bulging region increase over time, an additional variable for the time dependent angle of impacted bulging area, φ, was used. The value of this angle was determined by using the COSMOSM thermal simulation to find the time at which the temperature wave of 800 °C completely radially penetrated the PT wall.

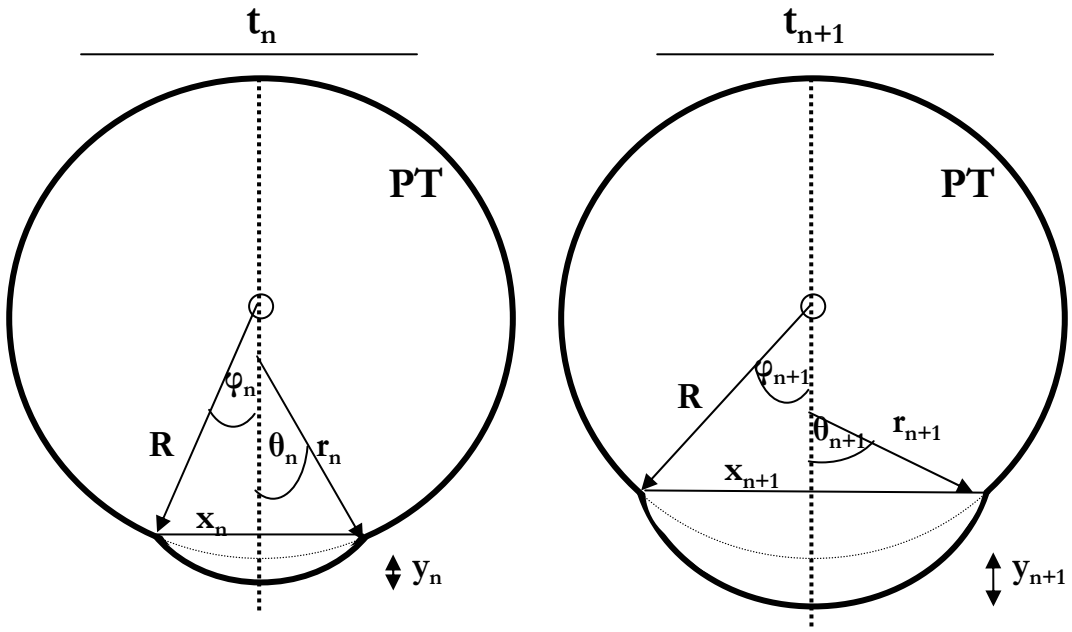

Figure 32: Time Dependent Bulge Size

This model only requires a few adjustments from the fixed bulging area model discussed in the previous section. The objective is still the same: finding values for the change in thickness, radius of curvature and theta at each time step. The only major changes are in the geometrical relations discussed from Equation (B.21) on. The logarithmic strain at any time step, n, is now defined as:

$$\varepsilon_{t_n} = \ln\left(\frac{r_n \theta_n}{R\varphi_n}\right) \tag{B.28}$$

where R, r_n, θ_n, φ_n are the radius of the PT, radius of curvature of the bulge at step n, angle of curvature of the bulge at step n, and angle between the line of symmetry and the outer rim of the bulge at step n. As in the previous section, a set of geometrical relations can be found by using Figure 32:

$$\sin\theta_n = \frac{x_n}{r_n} \tag{B.29}$$

$$\sin\varphi_n = \frac{x_n}{R} \tag{B.30}$$

where x_n is distance perpendicular to the line of symmetry in the bulge to the outer rim of the bulging area at step n. These can be rearranged to obtain:

$$\frac{r_n}{R} = \frac{\sin\varphi_n}{\sin\theta_n} \tag{B.31}$$

which can the be used to find the angle of curvature of the bulge at time step n:

$$\frac{\sin\theta_n}{\theta} = \frac{\sin\varphi_n}{\varphi_n}\frac{1}{e^{\varepsilon_{t_n}}} \tag{B.32}$$

The reference volume, V_{n0}, of the PT wall at any time step if there were no bulging is then:

$$V_{n0} = \left[\frac{4}{3}\pi(R+\delta_0)^3 - \frac{4}{3}\pi R^3\right]\frac{2\pi(1-\cos\varphi_n)}{4\pi} \tag{B.33}$$

and the actual volume of the bulging region at step n is:

$$V_n = \left[\frac{4}{3}\pi(r_n+\delta_n)^3 - \frac{4}{3}\pi r_n^3\right]\frac{2\pi(1-\cos\theta_n)}{4\pi} \tag{B.34}$$

By combining Equations (B.33) and (B.34), one can solve for the thickness of the PT at step n. These new values for thickness, radius of curvature, and θ at step n are then input to the stress and strain equations for step n+1 and the process is repeated until failure of the PT occurs.

To find the distance the center of the bulging area has displaced from its initial position at step n, y_n, the following simple geometric relation is used:

$$y_n = \left(r_n - r_n \cdot \cos\theta_n\right) - \left(R - R \cdot \cos\varphi_n\right) \tag{B.35}$$

Temperature Input

The temperature within the bulging region is not uniform, which means some method of choosing a characteristic temperature for input into the creep strain rate equations is required. Merely picking an average temperature for the volume is not physical, as this average temperature would be very high due to the extremely high temperatures present on the inner surface of the PT in contact with the molten mass. Once the high temperature wave (~>800 °C) has penetrated a radial portion of the PT, this section becomes essentially 'liquefied' – carrying little to no pressure load, and capable of straining at high rates. The cooler shell, toward the outer surface of the PT (see Figure 33), carries the actual load, and prevents the hot inner layer from radially bulging at a rate consistent with its high temperature. Thus, it is actually the coolest radial node, or the outer surface, that controls radial bulging. Unlike radial straining, the circumferential strain rate is dominated by the hottest circumferential segment, which in this case would be a straight line beneath the center point of the molten Zry droplet through the PT thickness. Thus, the single node that approximately dominates bulging is the node directly beneath the center of the molten Zry droplet on the outer surface of the PT. The temperature history of this node, T_b, is obtained from the COSMOSM thermal simulation and placed into the MATLAB bulging model.

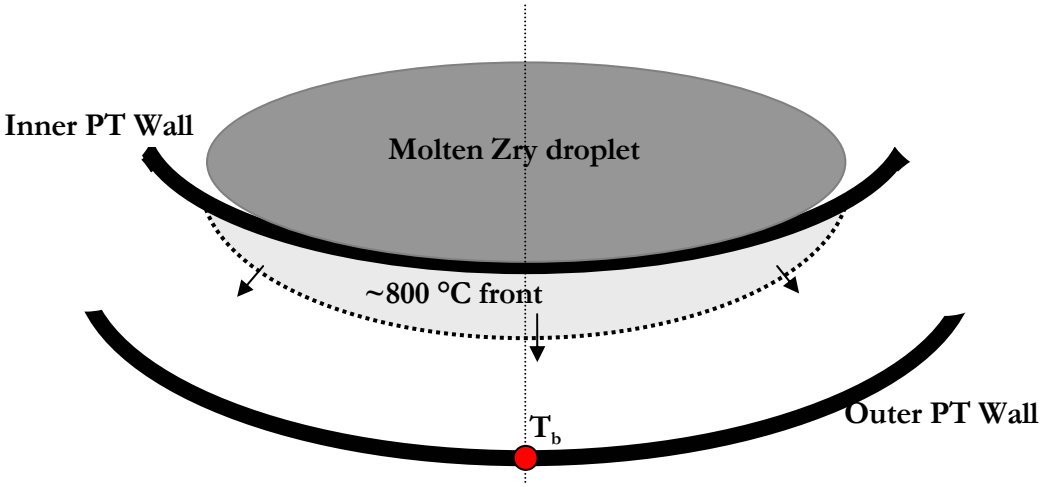

Figure 33: Movement of High Temperature Front through Cross section of PT Wall

B.8. VERIFICATION OF THE PT BULGING MODEL

To ensure that the analytic model created to describe the evolution of the bulging area is reasonable, it was benchmarked with the results from a similar case in the literature. Kojic [26] was chosen as it discusses the creep bulging of a thin circular plate under pressure. This model uses a circular plate that is connected to a rigid wall via a hinge at the outer radius and is subject to a normal pressure p=0.2 MPa. The disk has a 24 mm diameter, and is 0.314 mm thick. The creep law is defined as:

$$\varepsilon_c = 2x10^{-9}\sigma^3 \cdot t^{1.2} \tag{B.36}$$

A comparison of the result for the deflection of the central point during time obtained via the model discussed in Section B.6 with that of Kojic is shown in Figure 34. The results agree very well, and thus the MATLAB model is considered accurate.

As a way of comparing this result to the PT structural models in the following portions of this report, Figure 35 is included showing that bulging is fairly limited in this thin disk case.

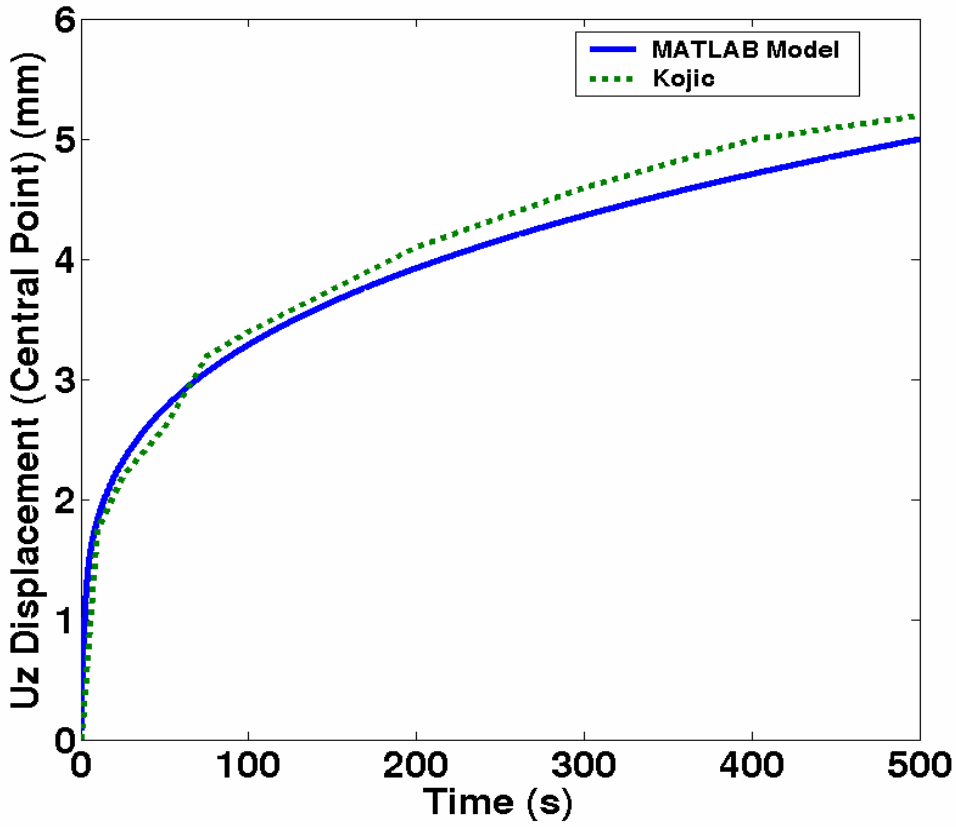

Figure 34: Displacement of Central Point during Time for Creep Bulging in a Circular Plate

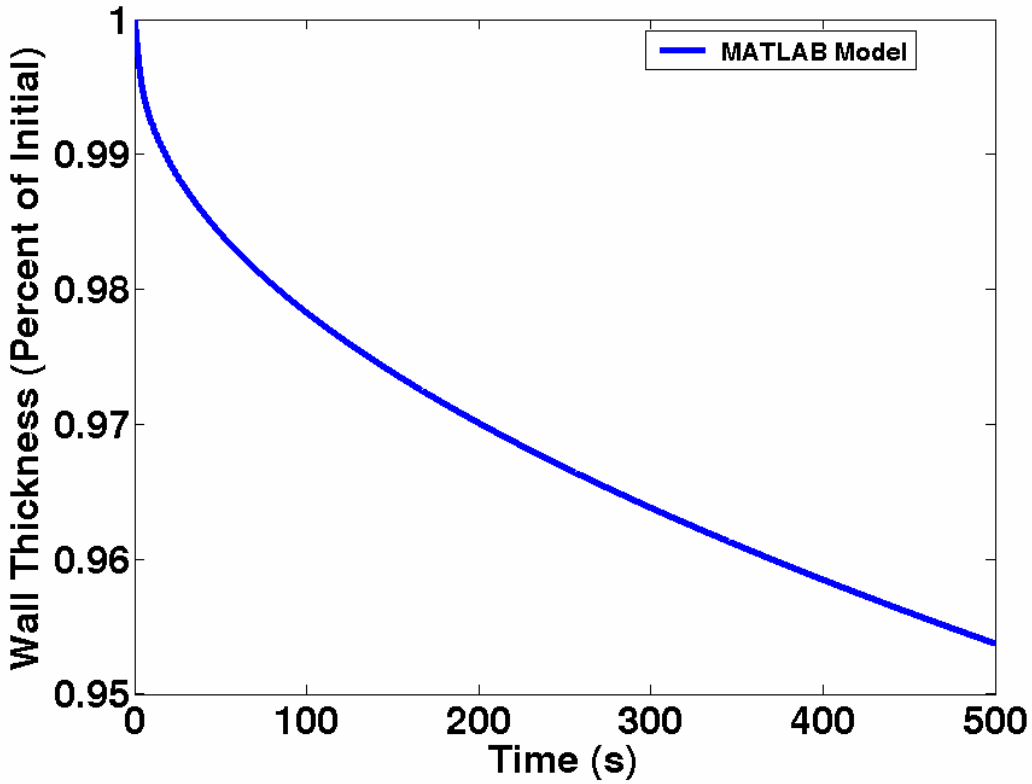

Figure 35: Reduction in Wall Thickness over Time for Creep Bulging in a Circular Plate

B.9. PT CONTACT WITH CT

The nominal radial distance between the PT and CT is 17.331 mm. It is expected that the PT bulge will need to displace further than this distance in order to reach the theoretical rupture point. Thus, inclusion of the thermal and structural impact of bulge-CT contact is important in evaluating the time to CT failure, because failure of this barrier is what ultimately allows a steam bubble to penetrate into the moderator and result in accident detection and reactor scram. Since the thermal analyses for these studies do not include the effects of the shape change as bulging progresses, this CT analysis assumes that the entire CT is in contact with the PT (see Figure 36), but large thermal resistances were introduced between the surfaces other than directly below the bulge area so that, thermally, only the bulged area of the PT will 'see' the CT. The entire surface of the bulging area was assumed to be in contact with the CT once minimal contact was made as shown in Figure 37. This is somewhat non-physical as the dimensions used for the CT in this thermal model are not exact in order to allow for PT/CT contact. However, since cooling via convection on the outer surface of the CT (discussed in Section B.4) is more important than circumferential or axial conduction within the PT, the thickness of the CT was modeled exactly as 2.5 mm, while the inner and outer radii were modified from 75.5 to 58.169 cm and 78.0 to 60.669 cm respectively. The structural analysis for this model utilized the same methods discussed in Section B.9, however, the actual dimensions of the CT were used, and the temperature history was taken from the node directly below the center of the molten mass on the outer surface of the CT. The creep equations from Shewfelt were used for the CT as well, even though the material properties between the PT and CT do differ, simply to have an approximate estimate for time to CT failure. When the PT comes in contact with the CT, it is reasonable to assume the PT is extremely compliant and thus transfers its full load to the CT in the region of contact.

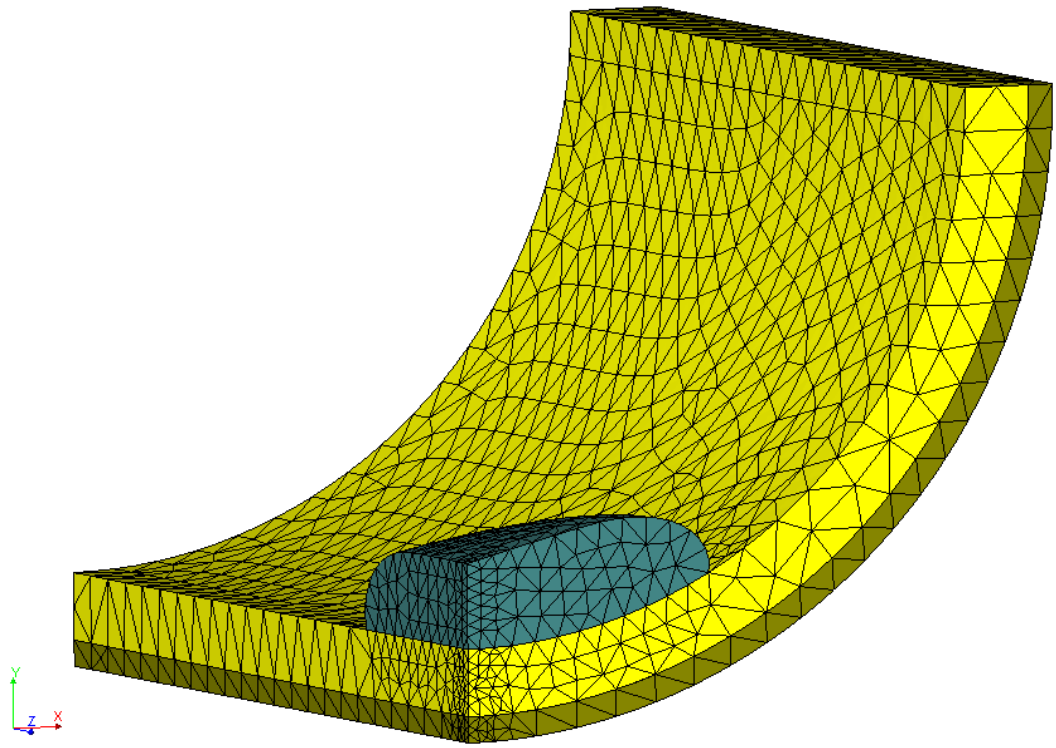

Figure 36: Meshing of 100g melt, PT & CT for Thermal Analysis

The simulation steps taken to include the CT contact are as follows:

1. Run COSMOSM thermal analysis without addition of CT
2. Run MATLAB structural analysis of PT coupled to thermal analysis of step 1. Find time at which the displacement of the central point in bulge equals 17.3mm.
3. Run COSMOSM thermal analysis with large thermal resistances between PT/CT walls until the time found in step 2. At this time, remove the thermal resistance between the PT/CT directly below the melt. Continue thermal analysis using a large (10,000-40,000 W/m^2K) convection coefficient consistent with nucleate boiling along CT outer wall
4. If film boiling is expected to occur in step 3, rerun the thermal analysis of step 3 with a small (~350 W/m^2K) convection coefficient consistent with film boiling
5. Run MATLAB structural analysis of CT coupled to thermal analysis of step 4 to find time at which CT is expected to fail or the thermal transient dissipates

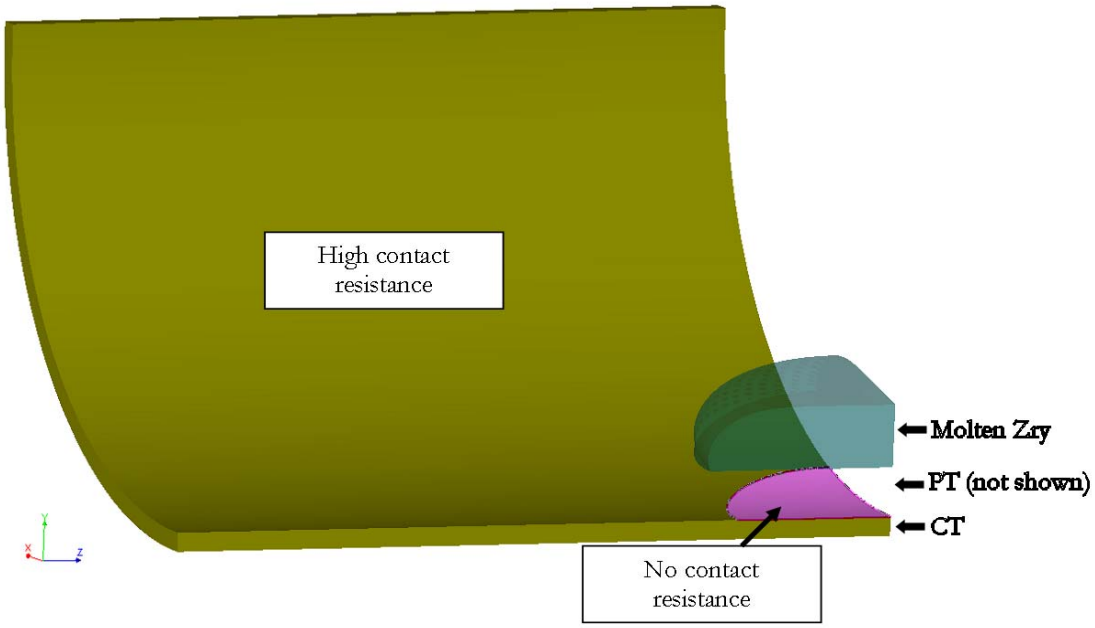

Figure 37: Depiction of high and zero contact resistance regions between CT inner and PT outer surface used in thermal analysis of PT bulge/CT contact (PT not shown)

B.10. HEAT TRANSFER ON OUTSIDE OF CALANDRIA TUBE

It is important to have an order of magnitude value for the heat transfer that will occur on the outer surface of the CT once the bulge comes in contact with the CT inner surface. The magnitude of this heat transfer will control whether the CT will bulge as well, or if it will dissipate the thermal transient, and prevent failure. To properly bound this value, a high convection coefficient consistent with nucleate pool boiling, and a low convection coefficient consistent with film boiling are used as discussed below.

Nucleate Pool Boiling Heat Transfer

From Table 10-2 of Todreas & Kazimi [4], the typical value for the heat transfer coefficient due to natural convection in boiling water is in the range of 60-12,000 W/m^2K. To obtain a more specific value, some correlations from Zuber [4] and Rosenhow [16] were applied to this case.

Zuber's correlation of CHF was used to get an approximate value for the maximum heat flux that could occur during pool nucleate boiling. At the approximate pressure within the

calandria of two atmospheres, Zuber predicts CHF to occur at a heat flux of 0.55 MW/m^2. A value of half that of CHF, or 0.275 MW/m^2 was used to approximate the flux experienced in nucleate boiling. Rosenhow's correlation was then used to find the temperature difference between the CT wall and the bulk fluid when this heat flux is applied:

$$q_s'' = \mu_l h_{fg} \left[\frac{g(\rho_l - \rho_v)}{\sigma} \right]^{0.5} \left[\frac{C_{p,l}(T_w - T_{sat})}{C_{s,f} h_{fg} \, \mathrm{Pr}_l^n} \right]^3 \tag{B.37}$$

with μ_l, h_{fg}, ϱ_l, ϱ_v, σ, $C_{p,l}$, $C_{s,f}$, Pr_l, and T_w being the viscosity of the liquid moderator, change in boiling enthalpy, density of the liquid, density of the vapor, surface tension of the liquid, heat capacity of the vapor, Prandtl number of the vapor, and temperature of the outer CT wall respectively.

The values used for the physical parameters in this correlation are given in Table XV. Properties of water (instead of heavy water) at 100 °C were used.

Table XV: Parameters used for Nucleate Pool Boiling from CT Outer Surface

Parameter	Value
Viscosity - liquid (N s/m^2)	283x10^{-6}
Specific Volume – liquid (m^3/kg)	1.0435x10^{-3}
Specific Volume – gas (m^3/kg)	1.673
Enthalpy of Vaporization (kJ/kg)	2257
Heat Capacity – liquid (kJ/kgK)	4.218
Surface Tension – liquid (N/m)	58.78x10^{-3}
Prandtl Number	0.987
Cs,f (constant from Incropera)	0.013
n (exponent from Incropera)	1.0

This calculation results in an wall superheat ($\Delta T_e \equiv T_w - T_{sat}$) of approximately 7.0 K. Using the familiar expression relating the wall superheat with heat flux, q":

$$q'' = h \cdot (T_w - T_{sat}) \tag{B.38}$$

with h being the convection coefficient of the moderator. One can find that the approximate heat transfer coefficient is 40,000 W/m^{2}K. Since this value is high it was used

along with a more reasonable value of 10,000 W/m^{2}K in all of the calculations involving the heat transfer of the CT. The value of 40,000 is extremely conservative regarding CHF, though. Also, it is important to recognize since this hot spot is on the underside of a horizontal tube, heat transfer will be inhibited, which would further reduce the expected heat transfer coefficient.

Film Boiling Heat Transfer

When the wall superheat predicted using the large nucleate boiling heat transfer coefficient is large (> 30 K), then the system will transition to the film boiling regime. In this regime, the surface of the CT in the region underneath the molten mass will be completely covered by a vapor blanket whereby poor heat transfer will occur via conduction and radiation through the vapor. Thus, the heat transfer coefficient will be considerably smaller than for nucleate boiling. The film pool boiling correlations from Incropera and DeWitt [16] were used to find the film boiling convection coefficient on the outer surface of the CT:

$$\bar{h}_{conv} = \frac{k_v}{D} C \left[\frac{g(\rho_l - \rho_v) h'_{fg} D^3}{v_v k_v (T_w - T_{sat})} \right]^{1/4} \tag{B.39}$$

where h_{conv}, k_v, D, C, ϱ_l, ϱ_v, and v_v are the effective convection coefficient, conductivity of the vapor, CT diameter, correlation constant (0.62 for horizontal cylinders), liquid density, vapor density, and the specific volume of the saturated vapor respectively. All vapor properties are evaluated at the film temperature, $T_f=(T_w+T_{sat})/2$. The corrected latent heat, h'_{fg}, is approximated by $h'_{fg}=h_{fg}+0.80C_{p,v}(T_w-T_{sa}t)$. The effective heat transfer coefficient, h, is then calculated using Bromley's [16] transcendental equation:

$$\bar{h}^{4/3} = \bar{h}_{conv}^{4/3} + \bar{h}_{rad} \bar{h}^{1/3} \tag{B.40}$$

where the effective radiation coefficient, h_{rad} is:

$$\bar{h}_{rad} = \frac{\varepsilon\sigma(T_w^4 - T_{sat}^4)}{T_w - T_{sat}} \tag{B.41}$$

where ε, and σ are the emissivity of the CT and Stefan-Boltzmann constant respectively. Using several iterations of this calculation, a high film boiling heat transfer coefficient of 350 W/m^2K corresponding with the hottest expected CT temperature (900 °C) was used to remain reasonably conservative.

B.11. RESULTS OF BULGING ANALYSIS

This section reports the thermal and structural results from the various types of analysis discussed in the preceding sections. A summary of these results is included in Table XVI. For all times listed, the initial time, or t=0, is the instant when the molten Zry droplet contacts the PT.

Table XVI: Summary of Bulging Results. (Moment when Zry contacts PT is t=0 for all times listed.)

Case #	Size of Molten Mass (g)	Zry/ Steam[6] Reaction?	Thickness of ZrO_2 on PT Surface (mm)	Time PT Bulging Begins (s)	Time bulge/CT contact (s)	Time CT Bulging Begins (s)	Time to CT Failure (s)
1	10	No	--	2.6	--	--	--
2	10	Yes	--	2.6	--	--	--
3	100	No	0.20	2.9	5.3	6.4	11.0
4	100	No	--	2.0	3.58	4.4	7.52
5	100	No	2.00	10.6	--	--	--

Case 1: 10g molten Zry, no Zry/PT contact resistance, no Zry/steam reaction, radiation & convection cooling included

For this case, the 10g molten droplet was placed in contact with the PT. No contact resistance was applied between the Zry and PT surface. No heat flux was applied from the steam/Zry reaction. Radiation and convection heat transfer boundary conditions were applied to the outer surface of the PT to properly model the gas annulus. The values used for the impacted bulging angle (φ) for this case are included in Table XVII. The thermal and structural results are shown in Figure 38 and Figure 39 respectively. Since this droplet

[6] Radiation and convection cooling from outer surface of PT is included in all cases to properly model the gas annulus

is small, its thermal energy dissipates quickly within the PT, which results in minimal bulging and no failure. Do to the irreversible nature of creep strains the bulging area is displaced approximately 1.5 mm in 5.2 seconds where it remains as the transient subsides. Since a similar case including a Zry/PT contact resistance would result in decreased temperatures compared with the current case, and thus would not result in failure, it is not considered.

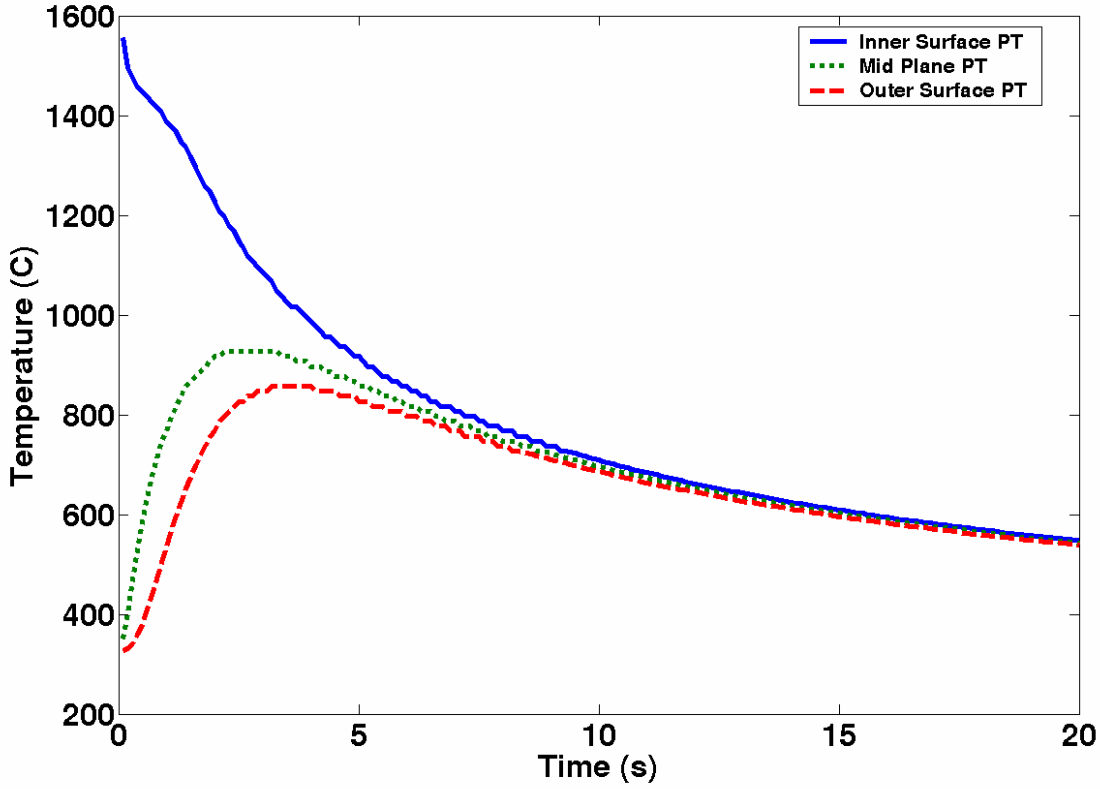

Figure 38: Case 1: Temperature Histories of PT Wall

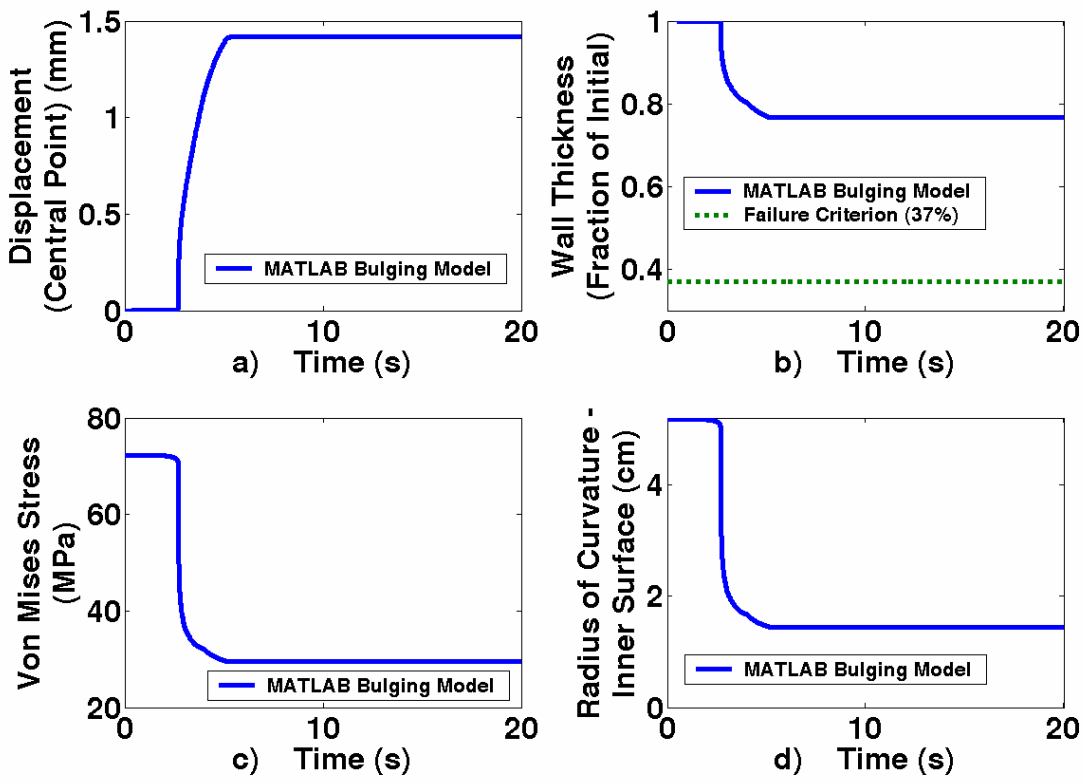

Figure 39: Case 1. a) Displacement of PT central point, b) PT Reduction in wall thickness, c) Von Mises membrane stress in PT bulge, d) Radius of curvature (inner PT)

Table XVII: Case 1. Impacted Bulging Angle (φ) used in MATLAB script

Time (s)	0	4	20
Impacted Bulging Angle (φ) (deg.)	7	8	8

Case 2: 10g molten Zry, no Zry/PT contact resistance, with Zry/steam reaction, radiation & convection cooling included

The Zry/Steam reaction could potentially provide enough excess heat to result in failure of the PT for the 10g droplet. A comparison of the temperatures resulting from the inclusion of this reaction and that of Case 1 is shown in Figure 40. Since there is very little (~10 °C maximum) temperature difference between the two cases, it is assumed that the structural results will be the same for both. Thus, this case is not expected to lead to failure.

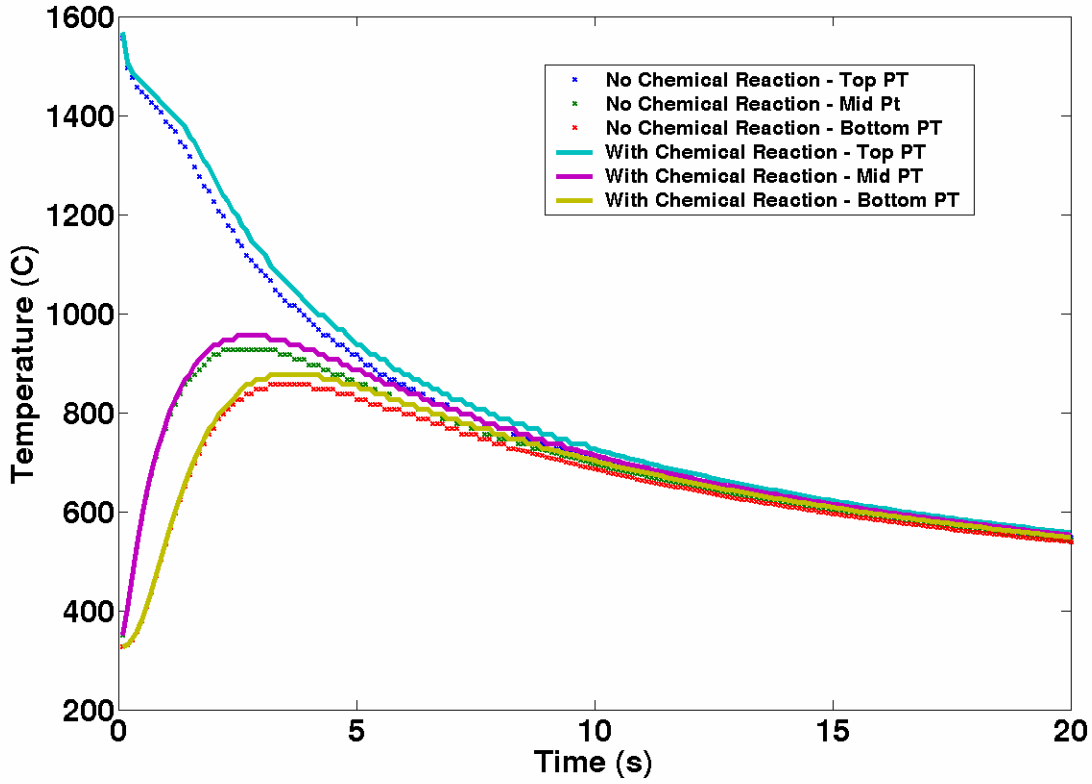

Figure 40: Comparison of Case 1 & Case 2 thermal results (10g Zry with and without Zry/Steam reaction)

Case 3: 100g molten Zry, 0.2mm Zry/PT contact resistance, no Zry/steam reaction, radiation & convection cooling from PT surface included

This case is considered the reference for all other 100g models, as it is the best estimate model. A layer of 0.2 mm ZrO_2 is modeled as a contact resistance on the inner surface of the PT in contact with 100g of molten Zry. Radiation and convective cooling on the outer surface of the PT is considered and no Zry/steam reaction is modeled. As discussed in the preceding sections, the thermal analysis of just the Zry/PT system is modeled first and input into a MATLAB structural model for the PT, shown in Figure 44. This structural model is used to find the time at which the bulge contacts the CT, which occurs at approximately 5.3 s after Zry/PT contact.

Also discussed in the preceding sections, nucleate boiling heat transfer is first assumed to occur on the outer CT surface once bulge/CT contact is made. If this analysis shows a sufficiently high wall superheat that would force a transition to nucleate boiling, then

another thermal analysis is completed with a low heat transfer coefficient consistent with film boiling. The results of this thermal analysis are then placed into the MATLAB structural model to predict the bulging of the CT. The results from two nucleate boiling analyses, one with a convection coefficient of 40,000 W/m^{2}K and the other of 10,000 are shown in Figure 41 and Figure 42. It is clear from the magnified cutaway of the CT outer surface temperature history in Figure 41, that the wall superheat will surpass 60 °C even for this extremely high heat transfer coefficient. Thus, film boiling is expected to occur and the results from this thermal analysis are shown in Figure 43. The structural model then utilizes this film boiling thermal result and is shown in Figure 45. This structural model predicts failure within 11 seconds.

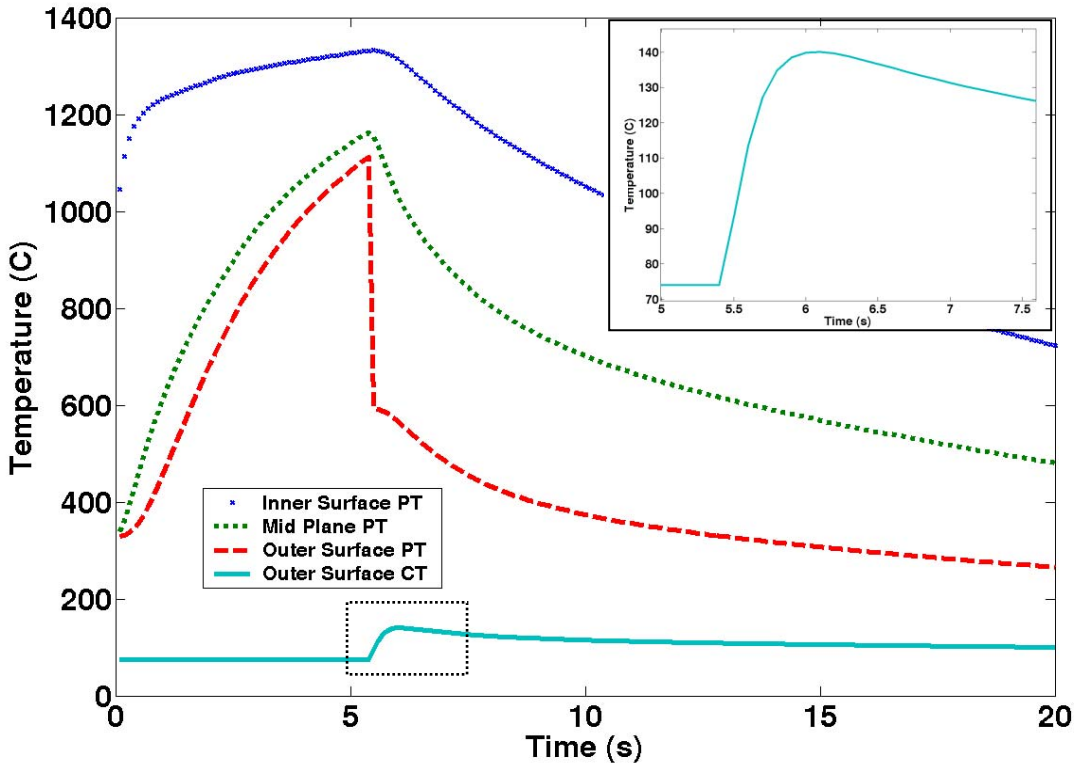

Figure 41: Case 3 – Temperature histories for h=40,000 W/m^{2}K on CT outer surface (with zoom-in CT outer surface initial heat-up)

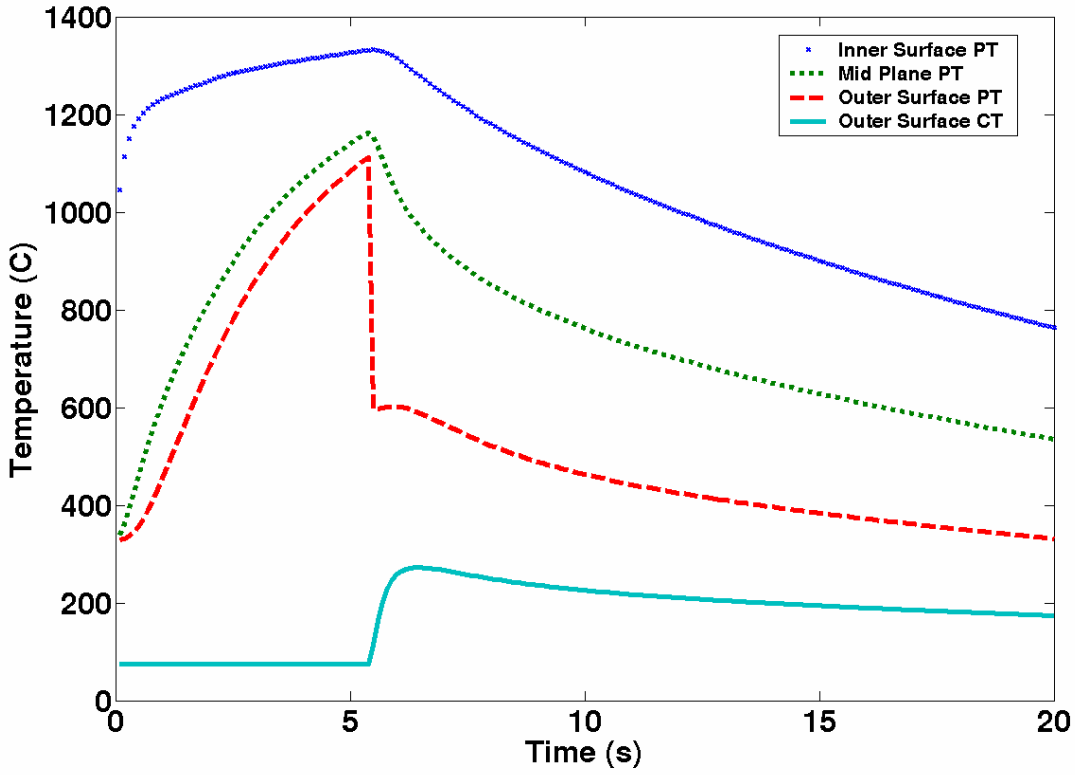

Figure 42: Case 3 – Temperature histories for h=10,000 W/m^{2}K on CT outer surface

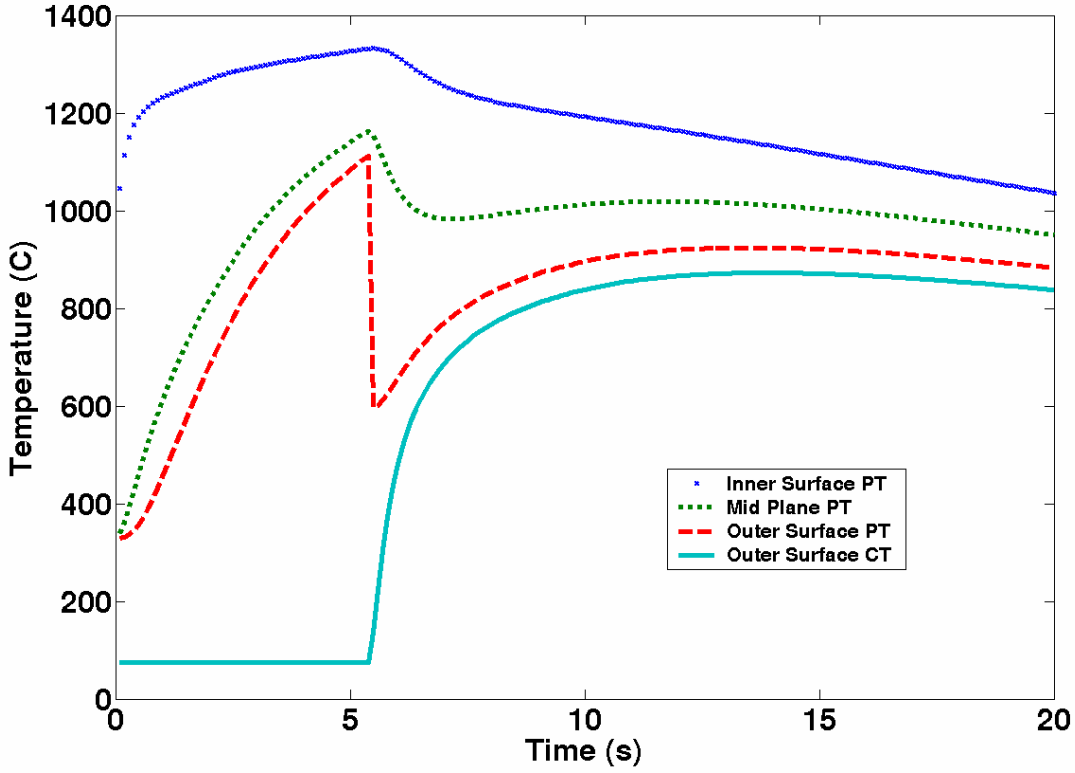

Figure 43: Case 3 – Temperature histories for film boiling heat transfer on CT outer surface

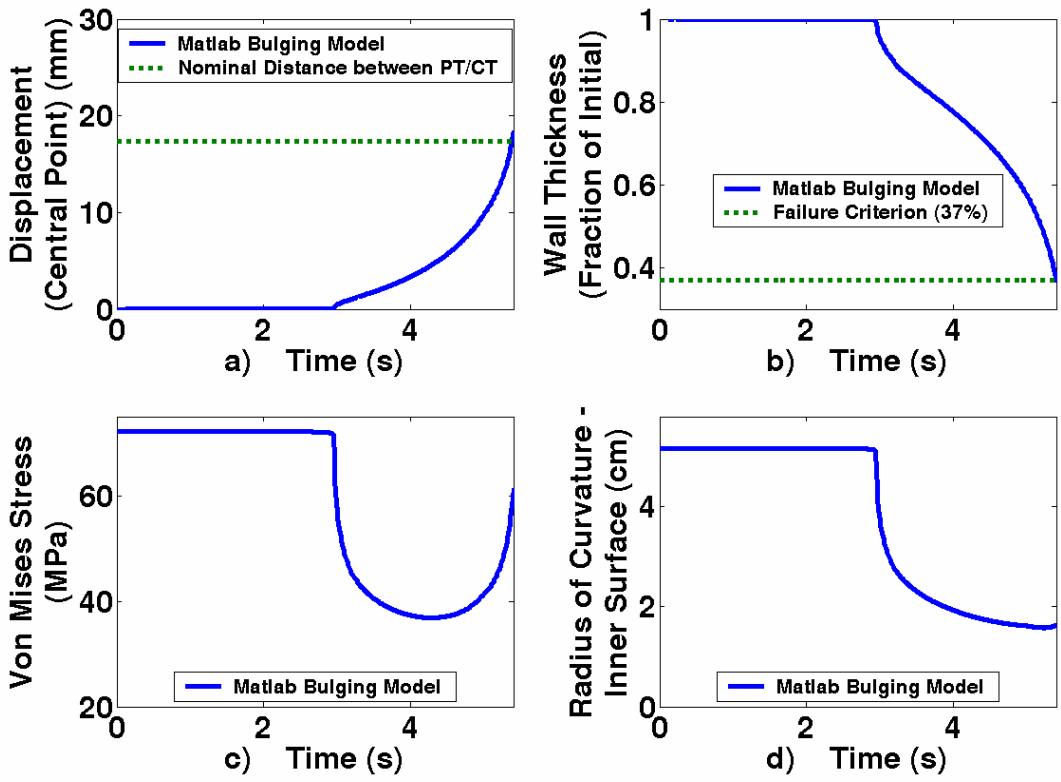

Figure 44: Case 3. a) Displacement of PT central point, b) Reduction in PT wall thickness, c) Von Mises membrane stress in PT bulge, d) Radius of curvature (inner PT)

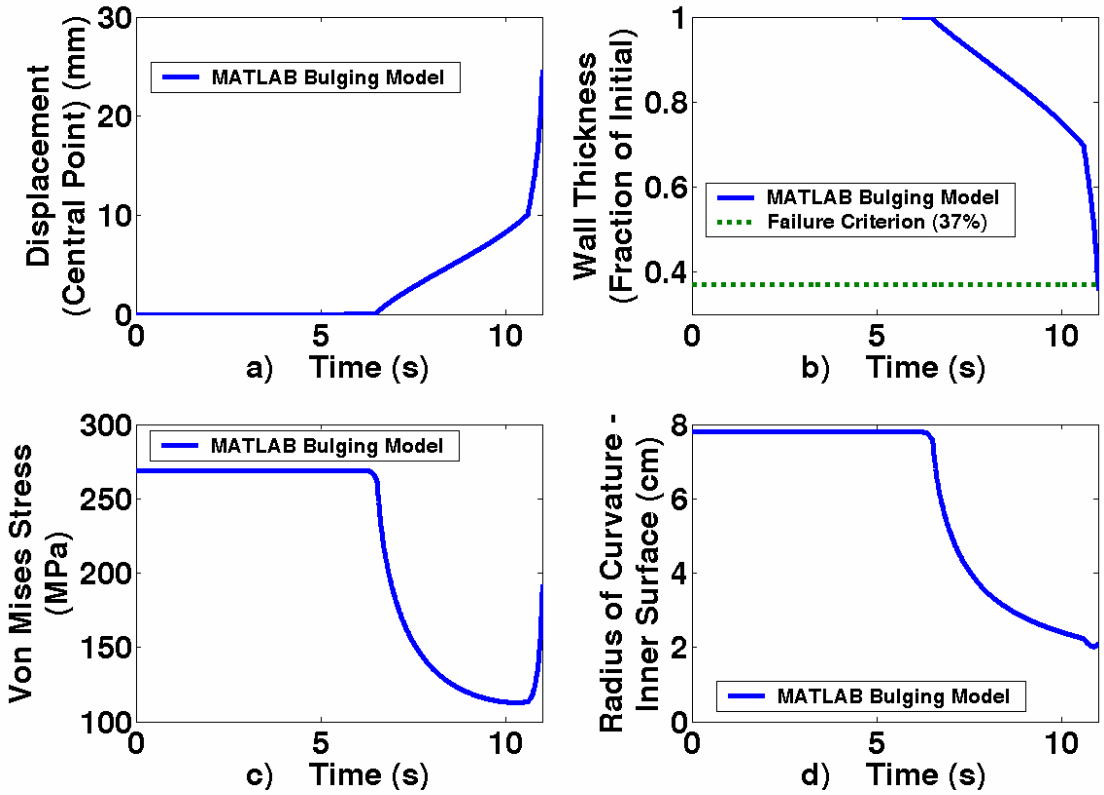

Figure 45: Case 3. a) Displacement of CT central point, b) Reduction in CT wall thickness, c) Von Mises membrane stress in CT bulge, d) Radius of curvature (inner CT)

Table XVIII: Case 3. Impacted Bulging Angle (φ) used in MATLAB script

Time (s)	0	3.5	12
Impacted Bulging Angle (φ) (deg.)	12	17.7	20

Case 4: 100g molten Zry, no Zry/PT contact resistance, no Zry/steam reaction, radiation & convection cooling from PT surface included

This case is considered to study the maximum speed that failure could occur with a 100g Zry droplet, as the major phenomena affecting PT heatup is the Zry/PT contact resistance, which this case neglects. Radiation and convection cooling is considered for the PT outer surface to properly model the gas annulus, while the Zry/steam reaction is not considered. The structural model for the PT in this case is shown in Figure 48, where it is clear that the bulge contacts the CT in approximately 3.58 s. Based on the expected temperature histories using an outer CT surface heat transfer coefficient of 40,000 W/m^{2}K shown in

Figure 46, the CT is expected to transition into film boiling almost immediately upon bulge contact. Using the temperature histories for film boiling from the CT surface shown in Figure 47, into the MATLAB model for CT bulging, it is expected that the CT will fail at approximately 7.52 seconds after Zry/PT contact as shown in Figure 49.

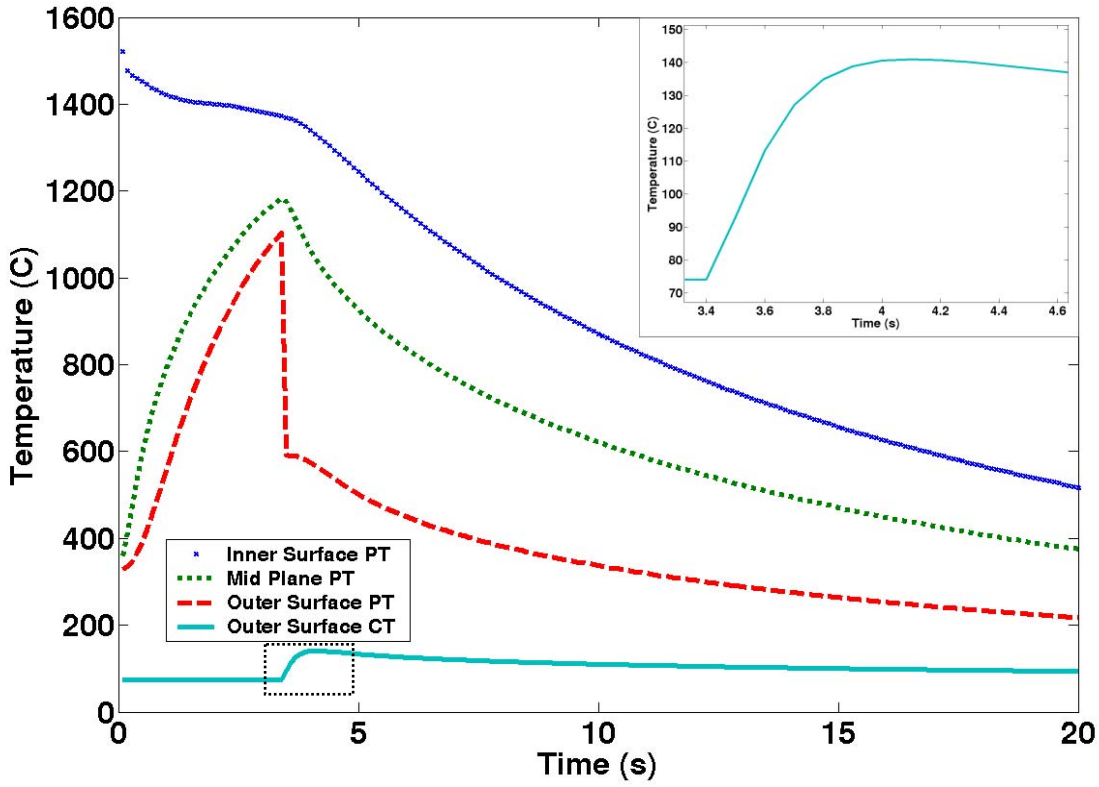

Figure 46: Case 4 – Temperature histories for h=40,000 W/m^{2}K on CT outer surface (with zoom-in CT outer surface initial heat-up)

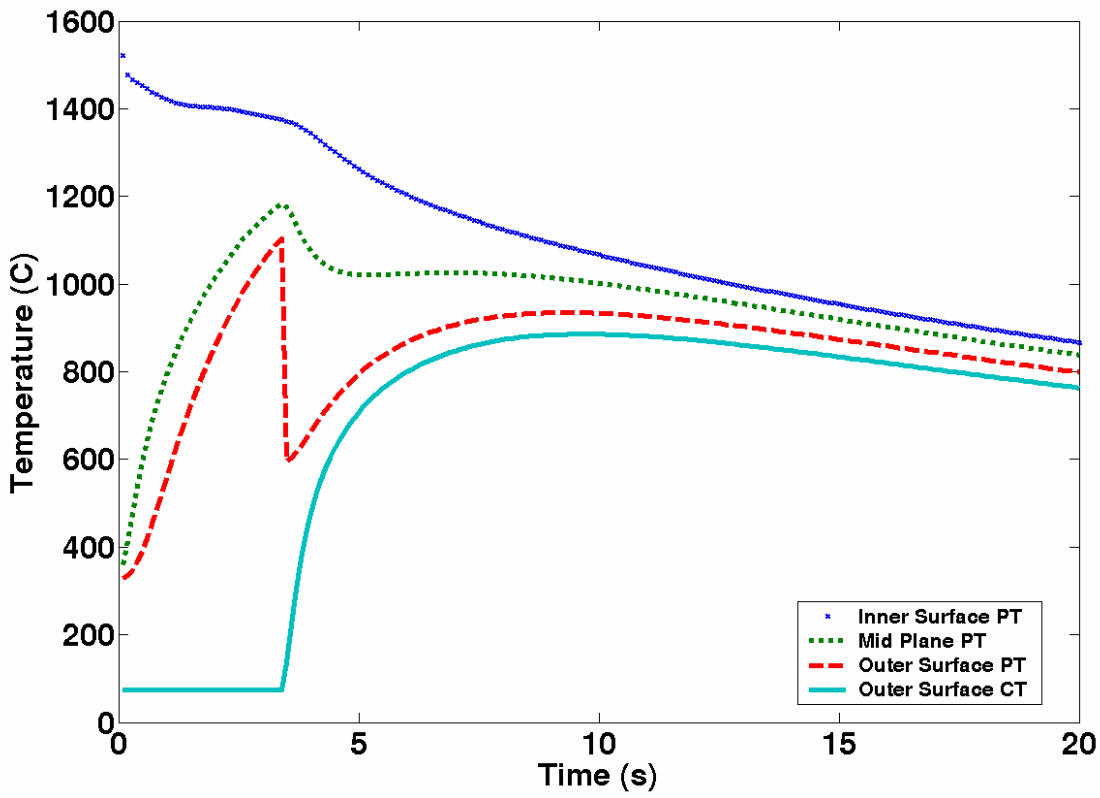

Figure 47: Case 4 – Temperature histories for film boiling heat transfer on CT outer surface

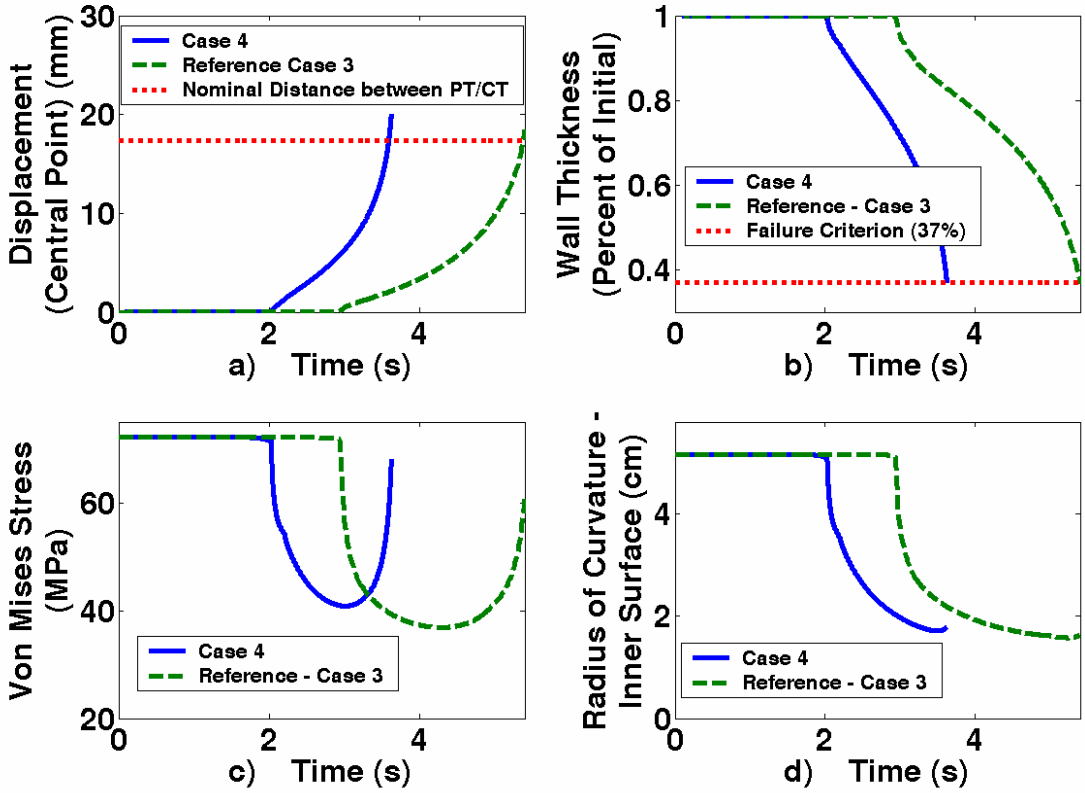

Figure 48: Case 4 (compared with reference Case 3). a) Displacement of PT central point, b) Reduction in PT wall thickness, c) Von Mises membrane stress in PT bulge, d) Radius of curvature (inner PT)

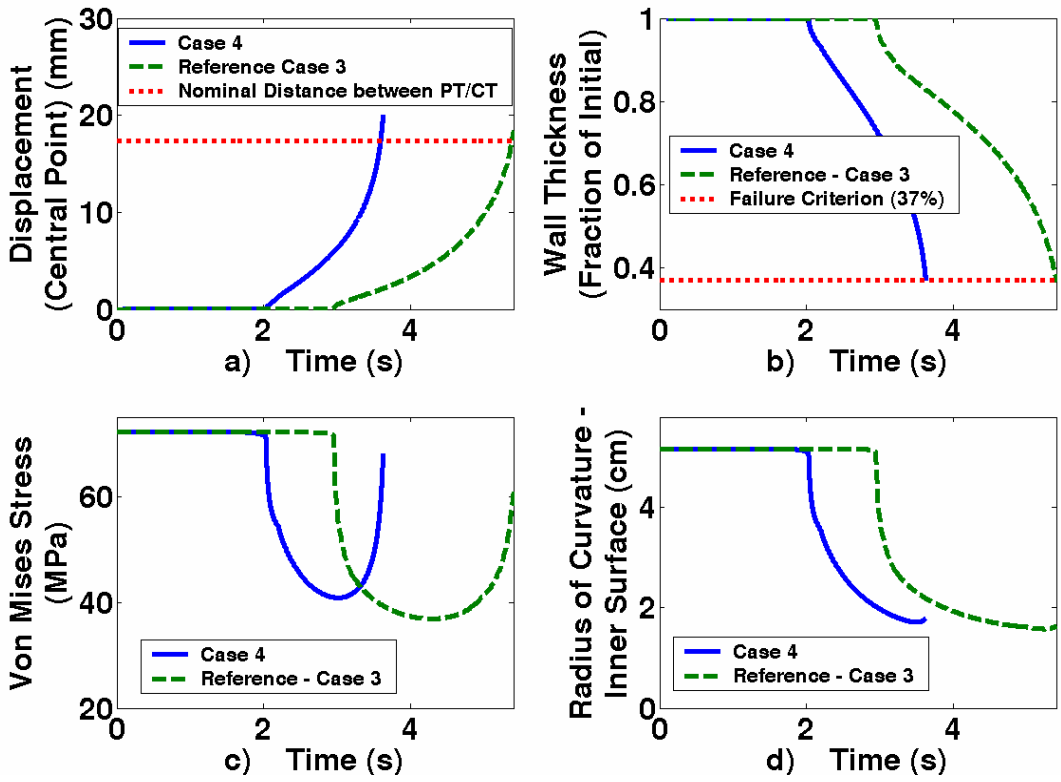

Figure 49: Case 4 (compared with reference Case 3). a) Displacement of CT central point, b) Reduction in CT wall thickness, c) Von Mises membrane stress in CT bulge, d) Radius of curvature (inner CT)

Table XIX: Case 4 Impacted Bulging Angle (φ) used in MATLAB script

Time (s)	0	2.2	4
Impacted Bulging Angle (φ) (deg.)	12	17.7	20

Case 5: 100g molten Zry, 2.0mm Zry/PT contact resistance, no Zry/steam reaction, radiation & convection cooling from PT surface included

The difference between this case and Case 3 and 4 is that a large portion of the PT thickness is assumed to be oxidized (2.0 mm) upon molten Zry contact in this case. This is an extremely thick oxide layer, and is considered unlikely in nearly any scenario, but is included as a bounding case. The temperature history for Case 5 is included in Figure 50 and the structural response of this case is shown in Figure 51.

Failure of the PT is not expected until 20.5 seconds after molten Zry contact, and due to the long duration for bulging over a larger area, contact with the CT is not expected to be made prior to PT failure in this case. In reality the PT will fail before 20.5 sec because of the relocation of significant additional molten Zry from the collapsing fuel assemblies.

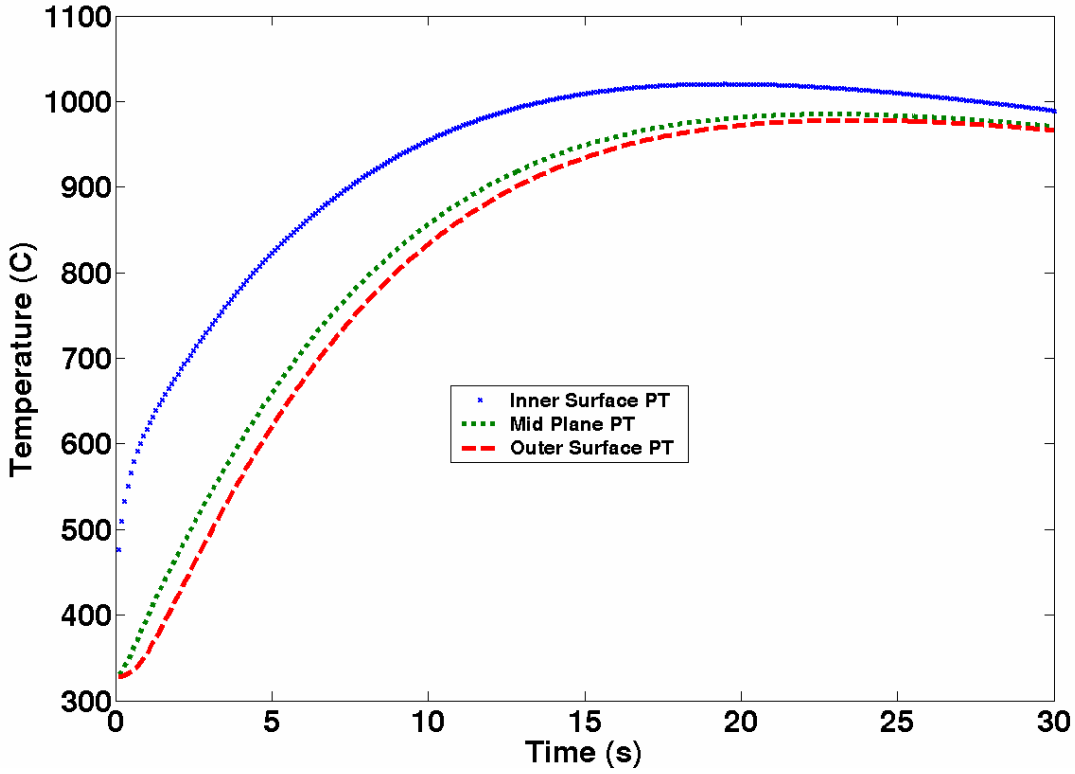

Figure 50: Case 5 – Temperature histories for points along PT thickness

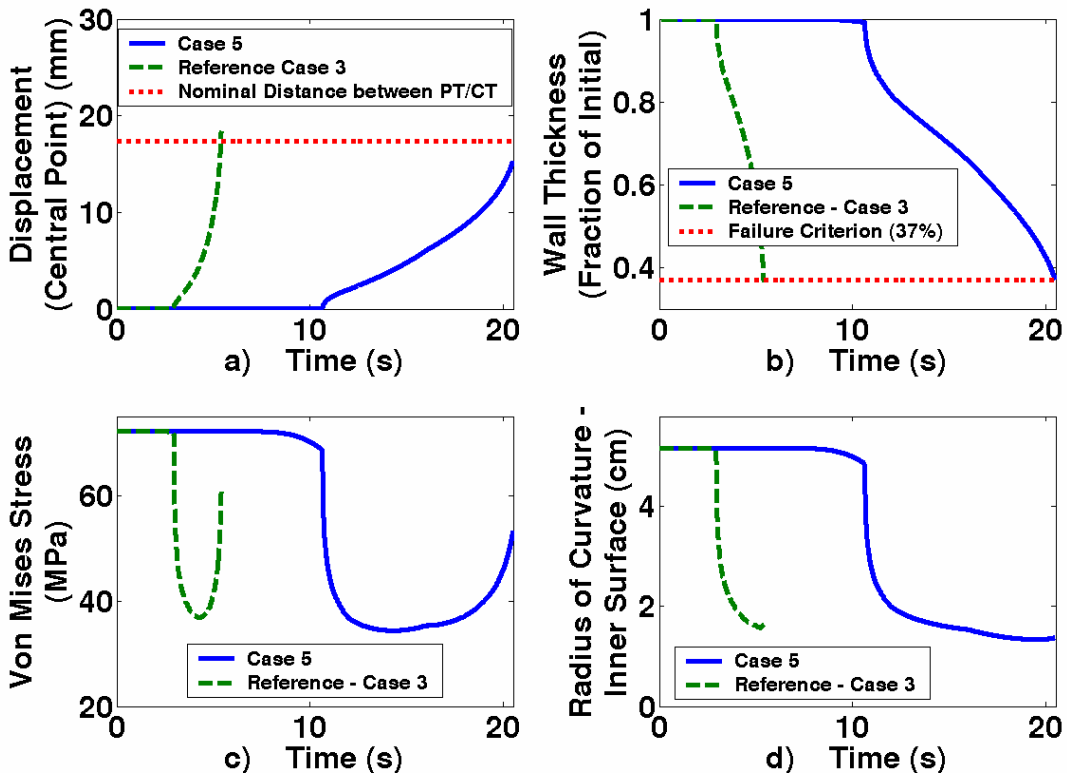

Figure 51: Case 5 (compared with reference Case 3). a) Displacement of PT central point, b) Reduction in PT wall thickness, c) Von Mises membrane stress in PT bulge, d) Radius of curvature (inner PT)

Table XX: Case 5. Impacted Bulging Angle (φ) used in MATLAB script

Time (s)	0	15	20
Impacted Bulging Angle (φ) (deg.)	12	16	16

APPENDIX C: SOURCE CODE

This is a sample of the MATLAB code used to calculate PT bulging. This is for the 100g reference case (Case 3) but is applicable to all cases.

```
clear all
close all

%%%%%%%%%%%%%%%%%%%%%%%%%%%%%%%%%%%%
% Define Variable Values
%%%%%%%%%%%%%%%%%%%%%%%%%%%%%%%%%%%%

TestName=['100g Reference - PT'];   %
Pi=12.0e6;          %internal pressure (Pa)
delta0=6.48e-3;     %initial PT thickness (m)
r0=51.689e-3;       %initial radius of curvature (m)
teta0=12/180*pi;    %initial angle (radians)
phid=[teta0*180/pi 12 17.7 20]/180*pi;      % time dependent angle of impacted  bulging
area
t_phi=[0 2 2.2 4];                      % times to apply phid

% Load Temperatures
load -ascii 'RES_100g_ThermalResistanceNONE.txt'
t=RES_100g_ThermalResistanceNONE(:,2);  % Define times used for temperatures
T=RES_100g_ThermalResistanceNONE(:,5)-273;  %Define temperatures

% Increase precision of temperatures by decreasing the time step - linearly
% interpolate to get new temperature values
precision=100;  % precision
tn(1)=(t(2)-t(1))/precision;
for h=1:(length(t))
   for k=1:precision
    tn(length(tn)+1)=tn(length(tn))+tn(1);
   end
end
t=tn;  %assign new time values

Tn(1)=T(1)
for k=1:precision-1
   Tn((length(Tn)+1))=T(1);
end
for h=2:length(T)
   for k=1:precision
      Tn((length(Tn)+1))=Tn(length(Tn))+(T(h)-T(h-1))/precision;
   end
end
```

```
T=Tn;  % assign new temperatures

N=length(t);  % get number of time increments
dt=t(2)-t(1); % get length of time increment

% Add final time to t_phi
numsteps=t_phi/dt; %get number of steps used for phi
if numsteps(length(numsteps))<length(t)
   numsteps=[numsteps length(t)];
   phid=[phid phid(length(phid))];
end

% Linearly interpolate phi so it has the same number of values as t
phi=[];
phidel=[];
for i=2:length(numsteps)
   phidel(i-1)=(phid(i)-phid(i-1))/(numsteps(i)-numsteps(i-1));
   if phidel(i-1)==0
      for j=(numsteps(i-1)+1):(numsteps(i))
         phi(j)=phid(i-1);
      end
   else
   for j=(numsteps(i-1)+1):(numsteps(i))
      phi(j)=phi(j-1)+phidel(i-1);
   end
   end
end

% Initial membrane stresses, strain, wall thickness and radius of curvature
sigr(1)=-Pi/2; %radial stress (Pa)
sigt(1)=1/((delta0/r0+1)^2-1)*Pi; %tangential stress (Pa)
sige(1)=(sigt(1)-sigr(1))*sqrt(2); %Von Mises equivalent stress (Pa)
epst(1)=0; %tangential strain
delta(1)=delta0; %wall thickness (m)
r(1)=r0; %radius of curvature (m)
teta(1)=teta0; %angle (radians)
i=1;

% Get membrane stresses, strain, wall thickness and radius of curvature,
% etc for every time step
for j=2:N

   %stresses
   sigr(j)=-Pi/2; %radial stress (Pa)
   sigt(j)=1/((delta(j-1)/r(j-1)+1)^2-1)*Pi; %tangential stress (Pa)
   sige(j)=(sigt(j)-sigr(j))*sqrt(2); %Von Mises equivalent stress (Pa)

   %strains
   %Shewfelt correlation
   if T(j)<850
      edot(j)=1.3e-5*(sige(j)/1e6)^9*exp(-36600/(T(j)+273.15));
```

```
    else
        edot(j)=10.4*(sige(j)/1e6)^3.3*exp(-19600/(T(j)+273.15));
    end

    edott(j)=1/(2*sqrt(2))*edot(j); %tangential strain rate (1/s)
    epst(j)=epst(j-1)+edott(j)*dt; %tangential strain

    %displacements

    PlaceholdV(j)=sin(phi(j))/phi(j)/(exp(epst(j)));  %placeholder variable

    teta(j)=teta(j-1); %guess
    err=1;
    while err>0.001
        tetanew=teta(j);
        teta(j)=sin(tetanew)/PlaceholdV (j);  %new theta
        err=abs(tetanew-teta(j));
    end
    V(j)=2*pi/3*(1-cos(phi(j)))*((r0+delta0)^3-r0^3);
    r(j)=r0*sin(phi(j))/sin(teta(j)); %radius of curvature (m)
    delta(j)=(r(j)^3+3*V(j)/(2*pi)/(1-cos(teta(j))))^(1/3)-r(j); %thickness (m)

    if delta(j)/delta(1)<.37  % Evaluate if failure criterion has been achieved
        break
    end

end

xTheor=r-r.*cos(teta)-(r0*ones(1,length(teta))-r0*cos(phi(1:length(teta))));        %        Get
displacement of central point in bulge

tfailure=t(length(delta))  %Print failure time
```

NOMENCLATURE

A	area	(m^2)
C	heat capacity	(J/kg·K)
D	diameter	(mm)
E	energy	(kJ)
K	rate constant	(mg^2/cm^4s)
P	pressure	(MPa)
Pr	Prandtl number	
R	pin radius	(cm)
R	thermal resistance	(m^2K/W)
Re	Reynold's number	
S	stiffness matrix	
T	temperature	(°C)
V	volume	(m^3)

h	heat of fusion	(kJ/kg)
h	heat	
k	thermal conductivity	(W/m·K)
m	mass	(kg)
q'	linear heat generation rate	(kW/m)
q"	heat flux	(kW/m^2)
$\dot{q}$	power generation/energy production rate	(MW)
r	radius	(mm)
t	time	(s)
v	velocity	(m/s)
x	bulging area radius	(cm)
y	thickness of PT	(mm)
y	vertical displacement of center of bulge	(mm)
z	droplet height	(mm)

Subscript

0	initial
∞	environment
c	clad
c	creep
clad	cladding
co	outer cladding diameter
conv	convection
CT	calandria tube
e	equivalent
evap	evaporation
f	fission

f	fuel
fo	fuel outer diameter
h	hydraulic
i	initial
i	step
i	inner
l	liquid
max	maximum
melt	melting of Zry
o	initial
o	outer
PT	pressure tube
r	radial
rad	radiation
s	solid
s	surface
sat	saturation
t	true engineering strain
t	tangential
v	vapor
w	wall
zr	zirconium
ϱ	non dimensional length

Greek

α	thermal diffusivity	(m^2/s)
γ	surface tension	(dynes/cm)
δ	oxide growth constant	($\mu m/s^{1/2}$)
δ	solidification thickness	(mm)
δ	change in length	(mm)
δ	membrane thickness	(m)
ε	emissivity	
ε	strain	(m/m)
$\dot{\varepsilon}$	strain rate	(1/s)
θ	angle	
θ	non-dimensional parameter	
λ	eigen value	
μ	viscosity	(Ns/m^2)
ξ	oxide thickness	(μm)
ϱ	density	(kg/m^3)
σ	applied stress	(MPa)
σ	Stefan-Boltzmann Constant ($5.67x10^{-8}$)	(W/m^2K^4)
σ	surface tension	(N/m)
τ	time constant	(s)
φ	time dependent angle of impacted bulging area	
Ω	solid angle	(ster)

REFERENCES

1. A. White, "Sequences of ACR Limited and Severe Core Damage Accidents" Presentation to the US NRC, May 6-7 2003

2. J.R. Ramsay, "Thermal Simulation of Molten-Material/Pressure-Tube Interaction in a CANDU Nuclear Reactor," AECL, Pinawa, Manitoba, Canada.

3. E. Kohn, et al., "CANDU Fuel Deformation During Degraded Cooling (Experimental Results)," *Proceedings of the 6th Annual Conference of the Canadian Nuclear Society*, Ottawa, ON, 16.39-16.45 (1985)

4. Todreas, Neil E., Kazimi, Mujid S. *Nuclear Systems I: Thermal Hydraulic Fundamentals*. Taylor & Francis. 1993.

5. PIRT for Single-Channel Severe Flow Blockage in ACR-700. AECL. Licensing Submission to U.S. NRC. February 2004. 108US-03500-LS-002. Revision 0.

6. P. Nikolopoulos, G. Ondracek, D. Sotiropoulou, "Wettability and Interfacial Energies Between Zirconia Ceramic and Liquid Metals," *Ceramics International*. **15**, 201-206 (1989).

7. V.F. Urbanic, T.R. Heidrick, "High Temperature Oxidation of Zircaloy-2 and Zircaloy-4 in Steam," *J. Nuclear Materials*, **75**, 251-261 (1978).

8. H. E. Rosinger, R.K. Rondeau, K. Demoline and K.J. Ross, "The Interaction and Dissolution of Solid UO2 by Molten Zircaloy-4 Cladding in an Inert Atmosphere or Steam," *Proceedings of the 6th Annual Conference of the Canadian Nuclear Society*. AECL Ltd., 16.33-16.38 (1985).

9. W. Dienst, P. Hofmann, D.K. Kerwin-Peck, "Chemical Interactions between UO2 and Zircaloy-4 from 1000 to 2000 °C," *J. Nuclear Technology*, **65**, 109-124 (April 1984).

10. O. Akalin, C. Blahnik, B. Phan, F. Rance, "Fuel Temperature Escalation In Severe Accidents", *Proceedings of the 6th Annual Conference of the Canadian Nuclear Society*, Ottawa, ON (1985)

11. C. Gerardi, J. Buongiorno, "Simplified Evaluation of Key Phenomena during a Complete Single-Channel Blockage Event in ACR-700," *Proceedings of the International Conference on Advances in Nuclear Power Plants 2005*, **Paper 5424,** Seoul, Korea, May 15-19, 2005.

12. S. Beer, *Liquid Metals: Chemistry and Physics*. Marcel Dekker, Inc., New York, New York, 161-212 (1972).

13. A. W. Adamson. *Physical Chemistry of Surfaces*. 6-30, Wiley, New York, New York. (1997).

14. SolidWorks 2004/2005 Online User's Guide. SolidWorks Corporation (2004).

15. COSMOSM 2.85 (2003/220) Command Reference. Structural Research and Analysis Corporation (SRAC) (2003).

16. F.P. Incropera, D.P. Dewitt, *Fundamentals of Heat and Mass Transfer*, 268-272, John Wiley & Sons (2002).

17. R.S.W. Shewfelt, L.W. Lyall and D.P. Godin. "A High-Temperature Creep Model for Zr-2.5 wt% Nb Pressure Tubes," *J. Nucl. Materials.*, **125**, 228-235 (1984).

18. W.C. Muir, M.H. Bayoumi, "Prediction of Pressure Tube Ballooning Under Non-Uniform Circumferential Temperature Gradients and High Internal Pressure," *Proc. Fifth International Conf. on Simulation Methods in Nuclear Engr.*, Montreal Canada (Sept 1996)

19. P.J Hayward, I.M. George, "Dissolution of ZrO_2 in molten Zircaloy-4". *J. Nuclear Matl.*, **265**, 69-77 (1999).

20. J. Fitch, "Using Oil Analysis to Monitor the Depletion of Defoamant Additives", Noria Corp. (2005), http://www.oilanalysis.com/learning_center/category_article.asp?articleid=103&relatedbookgroup=Lubrication (Accessed July 31, 2005).

21. MATLAB Release 13 Online User's Guide. MathWorks Corporation (2002)

22. International Nuclear Safety Center (INSC). Material Properties of Zr-2.5%Nb. Argonne National Lab. http://www.insc.anl.gov/matprop/zr-25nb/zr25nbk.pdf (Accessed Jan 31, 2005)

23. R.W.L. Fong, C.K. Chow, "High Temperature Transient Creep Properties of CANDU Pressure Tubes", Presented at the 23rd Annual Conference of the Canadian Nuclear Society, Toronto, ON, AECL-12143, (June 2002).

24. "KANUPP – IAEA Training: Annulus Gas Chemistry Control", Report #97146-224. CANTEACH Project website. http://canteach.candu.org/library/20032103.pdf.

25. MELCOR. Material Properties (MP) Package Reference Manual. Sandia National Laboratory. http://melcor.sandia.gov/reference/MPReferenceManual.pdf (Accessed Jan 31, 2005)

26. M. Kojic, "An Extension of 3-D Procedure to Large Strain Analysis of Shells", Comput. Methods Appl. Mech. Engr., 191, 2447-2462 (2002).

27. P.M. Mathew, D.G. Evans, B. Heindrichs, and I.M. George, "Emissivity and Surface Colour of Steam-Oxidized CANDU Fuel Sheath at High Temperatures," AECL Report COG-93-486 (May 1994)